

MICROCOPY RESOLUTION TEST CHART  
NATIONAL BUREAU OF STANDARDS-1963-A

AD-A145 107

12

**PREDICTION OF AERODYNAMIC CHARACTERISTICS OF  
FIGHTER WINGS AT HIGH ANGLES OF ATTACK**

B. Maskew  
T.S. Vaidyanathan  
J.K. Nathman  
F.A. Dvorak

Analytical Methods, Inc.  
2047 - 152nd Avenue N.E.  
Redmond, Washington 98052

CONTRACT N00014-82-C-0354

Final Technical Report

March 1984

Prepared for:

Office of Naval Research  
800 North Quincy Street  
Arlington, VA 22217

DTIC

AUG 23 1984

A

DTIC FILE COPY

Analytical Methods Report 8405

This document has been approved  
for public release and sale; its  
distribution is unlimited.

84 08 22 008

Unclassified

SECURITY CLASSIFICATION OF THIS PAGE (When Data Entered)

REPORT DOCUMENTATION PAGE		READ INSTRUCTIONS BEFORE COMPLETING FORM
1. REPORT NUMBER AMI Report No. 8405	2. GOVT ACCESSION NO. AD-A145107	3. RECIPIENT'S CATALOG NUMBER
4. TITLE (and Subtitle) PREDICTION OF AERODYNAMIC CHARACTERISTICS OF FIGHTER WINGS AT HIGH ANGLES OF ATTACK		5. TYPE OF REPORT & PERIOD COVERED Final Report 4/15/82 - 3/31/84
7. AUTHOR(s) Brian Maskew, T.S. Vaidyanathan, James K. Nathman and Frank A. Dvorak		6. PERFORMING ORG. REPORT NUMBER
9. PERFORMING ORGANIZATION NAME AND ADDRESS Analytical Methods, Inc. 2047 - 152nd Ave. N.E. Redmond, WA 98052		8. CONTRACT OR GRANT NUMBER(s) N00014-82-C-0354
11. CONTROLLING OFFICE NAME AND ADDRESS Office of Naval Research 800 North Quincy Street Arlington, VA 22217		10. PROGRAM ELEMENT, PROJECT, TASK AREA & WORK UNIT NUMBERS
14. MONITORING AGENCY NAME & ADDRESS (if different from Controlling Office)		12. REPORT DATE March 1984
		13. NUMBER OF PAGES 124
		15. SECURITY CLASS. (of this report) Unclassified
		15a. DECLASSIFICATION/DOWNGRADING SCHEDULE
16. DISTRIBUTION STATEMENT (of this Report)  Approved for public release; distribution unlimited.		
17. DISTRIBUTION STATEMENT (of the abstract entered in Block 20, if different from Report)		
18. SUPPLEMENTARY NOTES		
19. KEY WORDS (Continue on reverse side if necessary and identify by block number) Aerodynamics Separated Flows Vortical Flows Fighter Aircraft High Angle of Attack		
20. ABSTRACT (Continue on reverse side if necessary and identify by block number) Potential modeling techniques for representing separated and vortical flows are investigated with the objective being the prediction of aerodynamic characteristics of fighter wings at high angles of attack. A low-order surface singularity panel method is coupled with iterative routines for locating the force-free wake and for including viscous effects and edge vortices. The viscous effects are computed using integral boundary layer		

Unclassified

SECURITY CLASSIFICATION OF THIS PAGE(When Data Entered)

procedures and the displacement effect is represented in the panel method using the transpiration model. Regions of massive separation are enclosed in free vortex sheets which are included in the general wake configuration scheme of the panel method. Calculations show encouraging results in those cases where there is little cross flow inside the separated zone. The calculations were less successful when the separated zone became highly three-dimensional, as in the case of a vortex/surface interaction. The modeling technique promises to be a practical, cost effective approach to predicting the aerodynamic characteristics of fighter wings at high angle of attack; however, further development of the model is required for the highly three-dimensional separated zones involving strong vortical action. ↗

Unclassified

SECURITY CLASSIFICATION OF THIS PAGE(When Data Entered)

TABLE OF CONTENTS

<u>Section</u>	<u>Page No.</u>
List of Figures . . . . .	ii
1.0 INTRODUCTION . . . . .	1
2.0 BACKGROUND . . . . .	3
3.0 THEORY	
3.1 Potential Flow Method . . . . .	18
3.2 Streamline Analysis . . . . .	27
3.2.1 Construction of the Interpolation Zone . . . . .	29
3.3 Boundary Layer Methods . . . . .	41
3.4 Estimation of Leading-Edge Vortex Geometry	
3.4.1 Introduction . . . . .	42
3.4.2 Theory . . . . .	43
3.4.3 Wake Model . . . . .	45
3.4.4 Streamline Tracker . . . . .	48
4.0 NUMERICAL PROCEDURE . . . . .	52
5.0 CALCULATIONS	
5.1 Basic Test Cases . . . . .	56
5.2 Separated Flow Cases . . . . .	58
5.3 Vortex/Surface Interaction . . . . .	89
5.4 Leading-Edge Vortex Flows	
5.4.1 Delta Wing . . . . .	102
5.4.2 Swept Wing with Strake . . . . .	102
6.0 CONCLUSIONS AND RECOMMENDATIONS . . . . .	118
7.0 REFERENCES . . . . .	119



A1

LIST OF FIGURES

Fig. No.	Title	Page No.
2.1	Three Forms of Separated Flow on Wings . .	4
2.2	Basic Flow Chart for Separated Flow Modeling	6
2.3	Vortex Sheet Model for Separated Flows . .	8
2.4	Calculations on a NACA 0012 over a Large Alpha Range	
(a)	Comparison of Calculated and Experimental Lift Characteristics for a NACA 0012 . . .	9
(b)	Calculated Wake Shape for a NACA 0012 at 90° Incidence after 6 Viscous/Potential Flow Iterations . . . . .	10
(c)	Calculated Pressure Distribution on a NACA 0012 at 90° Incidence . . . . .	11
2.5	Separated Flow on a NACA 0012	
(a)	Comparison of Experimental Flow Field and Calculated Free Vortex Sheets . . . . .	13
(b)	Calculated Velocity Vectors using the Method of Ref. 4 . . . . .	14
2.6	Basic Stripwise Separation Model from Ref. 1	15
3.1.1	Idealized Flow Model--Section through the Wing and its Wake . . . . .	19
3.1.2	Local Coordinate System on a Wake Line . .	25
3.2.1	Coordinate System in Tangent Plane-to-Body Surface and Region Covered by Basic Four-Point Interpolation Scheme . . . . .	30
3.2.2	Sphere Streamlines; Equatorial View . . .	35
3.2.3	Sphere Streamlines; Polar View . . . . .	36
3.2.4	Calculated Pressure on Streamlines Compared against Exact Solution . . . . .	37
3.2.5	Streamlines on Upper Surface of Wing; Angle of Attack 16° . . . . .	38
3.2.6	Streamlines on Lower Surface of Wing; Angle of Attack 16° . . . . .	39

TABLE OF CONTENTS (CONTINUED)

<u>Fig. No.</u>	<u>Title</u>	<u>Page No.</u>
3.2.7	Tip Streamlines on Wing; Angle of Attack $16^\circ$	40
3.4.1	Unsteady Cross-Flow Analogy . . . . .	44
3.4.2	VORSEP Wake Model . . . . .	47
3.4.3	Streamline and Wake Geometry . . . . .	49
3.4.4	Prediction of Streamline Trajectory from Wake Doublet Distribution . . . . .	50
4.1	VSAERO Method Outline . . . . .	53
4.2	General Arrangement of the Configuration	54
5.1.1	Comparison of Calculated Chordwise Pres- sure Distributions on a Thin Swept Wing. .	57
5.1.2	Comparison of Calculated $y$ -Component of Velocity at Two Stations on Wing with Strake. NACA 0012 Section, $\alpha = 5^\circ$ . .	59
5.1.3	Comparison of Calculated and Experimental Spanwise Lift Distribution . . . . .	60
5.1.4	Comparison of Measured and Predicted Pres- sure Distributions . . . . .	61
5.2.1	Calculated Streamlines on a Rectangular Wing . . . . .	62
5.2.2	Effect of Angle of Attack on Extent of Tip-Edge Separation . . . . .	63
5.2.3	Calculated Separation Boundaries for a Range of Angles of Attack at Two Reynolds Numbers . . . . .	65
5.2.4	Tentative Flow Field Model for Low Aspect Ratio Wing just Beyond Stall (Winklemann (7))	66
5.2.5	Calculated Pressure Distributions along Three (External) Streamlines Starting Near The Tip . . . . .	67

LIST OF FIGURES (CONTINUED)

Fig. No.	Title	Page No.
5.2.6	Spanwise Pressure Distribution Calculated Near the Tip of a Swept Wing with Prescribed Edge Separation . . . . .	69
5.2.7	Chordwise Pressure Compared against Experiment at $y/c = 1.0$ . . . . .	70
5.2.8	Chordwise Pressure at Various Spanwise Stations Compared against Experiment . . . . .	71
5.2.9	Calculated Flow Separation Boundary . . . . .	73
5.2.10	Oil Patterns on the Upper Surface of the Wing Reproduced from Ref. 55 . . . . .	74
5.2.11	Vector Plot of Off-Body Velocity in $y-z$ Plane Normal to Free Stream Direction	
(a)	x-Station Close to Wing Tip . . . . .	75
(b)	x-Station One Chord Length Downstream of Tip . . . . .	76
(c)	x-Station Two Chord Lengths Downstream of Tip . . . . .	77
5.2.12	Off-Body Velocity Compared against Experiment (55) . . . . .	78
5.2.13	Calculated Streamlines and Separated Flow Wake on a Sphere for $Re = 4.28 \times 10^5$ . . . . .	79
5.2.14	Comparison of Calculated and Experimental Pressure Distributions on a Sphere at $Re = 4.25 \times 10^5$ . . . . .	79
5.2.15	Sphere with Paneling Rotated $15^\circ$ . . . . .	81
5.2.16	Separation Line Identified by New Procedure . . . . .	82
5.2.17	Comparison of Calculated and Experimental Pressure Distributions at Two Stations on a Wing with Extensive Separation	
(a)	$\eta = 0.6$ . . . . .	83
(b)	$\eta = .9$ . . . . .	84
5.2.18	Calculated Streamlines on a Swept Wing . . . . .	86

LIST OF FIGURES (CONTINUED)

<u>Fig. No.</u>	<u>Title</u>	<u>Page No.</u>
5.2.19	Low-Speed Aerodynamic Characteristics of Kolbe-Boltz Wing . . . . .	87
5.3.1	Calculations of a Vortex/Wing Encounter	
	(a) General View . . . . .	88
	(b) Side View . . . . .	88
	(c) Top View . . . . .	88
	(d) Spanwise Cut through Doublet Distribution at $x/c = .25$ . . . . .	88
	(e) Spanwise Cuts through $V_y$ Distribution at $x/c = .25$ and $.004$ . . . . .	88
	(f) Spanwise Cut through Pressure Distribution at $x/c = .004$ . . . . .	91
	(g) Streamlines (External) Calculated on Wing Upper Surface . . . . .	91
	(h) Velocity Survey in Cross-Flow Plane at $x/c = 1.3$ . . . . .	91
5.3.2	Layout of the Model for the Vortex/Wing Encounter . . . . .	94
5.3.3	Starting Condition for Wake Calculations Showing Wake-Grid Plane Locations . . . . .	94
5.3.4	Final Calculated Wake Configuration for the 80 Case	
	(a) General View . . . . .	96
	(b) Side View and Comparison with Experimental Vortex Track . . . . .	96
5.3.5	Plan View of Calculated (External) Streamlines for Aft Wing at 80 in Presence of Vortex . . . . .	96
5.3.6	Comparison of Calculated and Experimental Force and Moment Coefficients in Presence of Vortex . . . . .	98
5.3.7	Side View of Calculated Wake Configuration and Experimental Vortex Track with Aft Wing at 160 . . . . .	98
5.3.8	Comparison of Second and Third Calculated Wake Shapes for Aft Wing at 120 . . . . .	100

LIST OF FIGURES (CONCLUDED)

<u>Fig. No.</u>	<u>Title</u>	<u>Page No.</u>
5.3.9	Comparison of Computed Wake and Experimental Vortex Track for Aft Wing at 12°. .	100
5.3.10	Top View of Calculated Surface Streamlines on Aft Wing at 12° in Presence of Vortex and Showing Calculated Separation Zone (First Iteration) . . . . .	100
5.4.1	Delta Wing Leading-Edge Vortex Shape . . .	103
5.4.2	Predicted and Observed Elevation of Vortex Core over Delta Wing . . . . .	104
5.4.3	Predicted and Observed Span Position of Vortex Core over Delta Wing . . . . .	105
5.4.4	Delta Wing with VORSEP-Generated Leading-Edge . . . . .	106
5.4.5	Comparison of VSAERO Pressure Distribution on Delta Wing with Experiment . . . . .	107
5.4.6	Experimentally Observed Vortex Core Behavior over Straked Wing . . . . .	108
5.4.7	Single-Wake Model of Leading-Edge Separation over Straked Wing . . . . .	110
5.4.8	VORSEP-Generated Wake over Straked Wing .	111
5.4.9	Straked Wing with VORSEP-Generated Wake	
(a)	Yawed Station Cut; $x = 33.85$ , $y = 0.0$ , Beta = 49.07 . . . . .	112
(b)	Yawed Station Cut; $x = 49.95$ , $y = 0.0$ , Beta = 43.50 . . . . .	113
(c)	Yawed Station Cut; $x = 62.05$ , $y = 0.0$ , Beta = 36.70 . . . . .	114
(d)	Yawed Station Cut; $x = 90.25$ , $y = 0.0$ , Beta = 18.70 . . . . .	115
5.4.10	Comparison of VORSEP and VSAERO Vortex Circulation . . . . .	117

## 1.0 INTRODUCTION

The ever present demand for superior maneuverability of combat aircraft is pushing the operating range of these aircraft deeper and deeper into the high angle-of-attack regime. For effective design of these vehicles, techniques are required that are capable of predicting their performance and behavior at large angles of attack. Such predictions have not been successful in the past because the flow field is dominated by zones of separated and vortical flows which lead to highly non-linear aerodynamic characteristics. Vortices generated by the fuselage or engine nacelles may have significant contributions to these non-linear effects but the primary influences are normally associated with separations and vortical flows from wing surfaces. Therefore, as a start towards predicting the performance and behavior of combat aircraft at high angles of attack, a research program was undertaken whose objective is to predict aerodynamic characteristics of fighter wings using modeling techniques for extensive separation regions and edge vortices. The present report describes the approach used in the study and the development of analytical and modeling techniques, with emphasis placed on practical solutions. Results are presented from applications of the techniques to a number of basic test cases.

An interim report (1) described the development of a preliminary procedure for calculating separated flow characteristics on wings. The initial work started with an existing viscous/inviscid interaction program (2), (3). This was based on a potential flow panel method coupled with integral boundary layer routines. The basic program (3) had been developed specifically for treating high-lift wings up to the condition of separation onset and included an iterative routine for calculating the wake location. The new work extended the program to model separated flows using a strip-wise technique in which free vortex sheets were used to enclose the separated flow. This model had already proven successful in the two-dimensional case (5). The prime objectives of that first phase were to establish the overall program structure for the complex iteration cycles--involving wake-shape calculations, viscous/potential flow interaction and moving separation lines--and to validate this initial approach to separated flow modeling in three dimensions as expediently as possible.

The aim of later phases of the work, the subject of the present report, was to remove the simplifying parts of the Phase I approach and to form within the program structure a more general model for the overall objective to treat separated flows on fighter wings. This includes the presence of strake, leading-edge and tip-edge vortices. In order to

achieve these objectives, a more general panel method--which was under development under a separate project--was substituted for the preliminary code. The new program became VSAERO, for Vortex Separation AEROdynamics. The basic method is described in Reference 6.

The background work and the present approach to the separated flow modeling are discussed in Section 2. The theories for the various parts of the method are described in Section 3, while the related numerical procedure is outlined in Section 4. Example calculations and correlations with experimental data are discussed in Section 5.

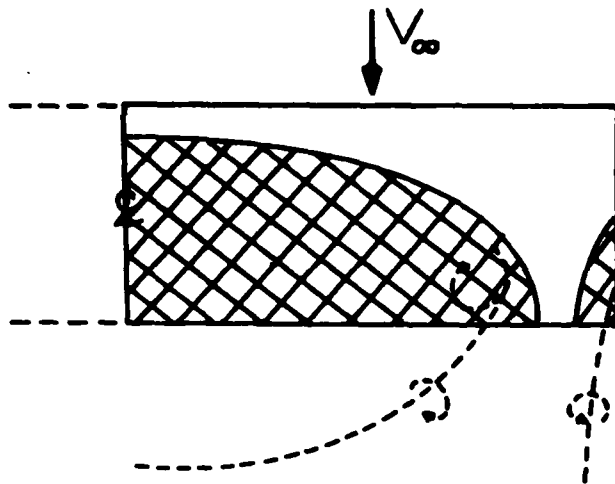
## 2.0 BACKGROUND

The flow field about a wing at high angle of attack is dominated by regions of separated flow with strong vortical flow structures. Experimental studies have established the general nature of such flow fields for a wide range of wing shapes. Figure 2.1 illustrates three basic forms. The simple rectangular wing just beyond the stall has an inboard and an outboard zone of separation, Figure 2.1(a), (e.g., (7)), and, depending on leading-edge contour and Reynolds number, a possible laminar bubble separation zone near the leading edge. The middle part of the inboard zone has an essentially two-dimensional character which could be treated with a stripwise model; however, the outer part of that zone leads to a strong three-dimensional vortical flow structure possibly connected downstream and across the wing centerline in a loop vortex (e.g., (7)). A corresponding lower-surface loop vortex of opposite sign would coexist with this. The loop vortex system is a time-averaged model as the real flow is basically unsteady (7). The outboard separated flow zone results from flow passing around the tip edge and separating (Section 5.2) in a strong adverse pressure gradient. This separation forms into the tip vortex structure above the surface and upstream of the trailing edge.

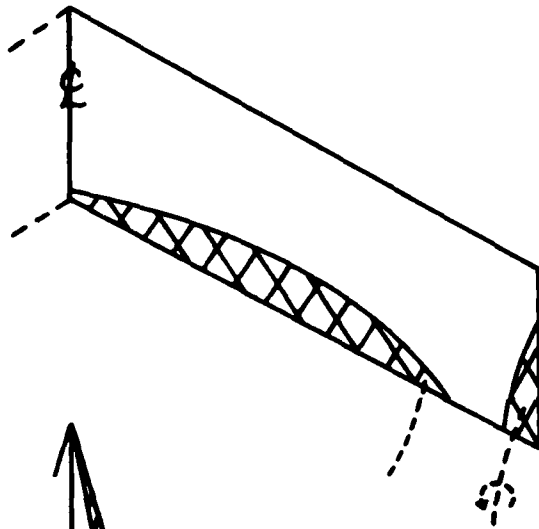
With increasing sweep, the extent of inboard trailing-edge separation tends to decrease, Figure 2.1(b) (e.g., see Section 5.2); however, this tendency would be influenced by wing-body junction effects on a complete aircraft configuration.

At high sweep and at higher angles of attack, separation occurs at the leading-edge (depending also on leading-edge radius of curvature and Reynolds number) giving rise to leading-edge vortices. These not only result in additional lift due to local suction under the vortex cores, but they can interact favorably with the wing boundary layer to reduce the tendency for trailing-edge type separation. These characteristics have led to the concept of kinked leading edges or sharp-edged strakes to purposely generate vortices at high angles of attack. The flow about a complete fighter wing, therefore, may have a mixture of strake vortices, leading-edge vortices and tip-edge vortices with possible intermediate zones of separation at the higher angles, Figure 2.1(c). Such multiple vortex configurations have been studied experimentally by, among others, White (8) and Hummel (9).

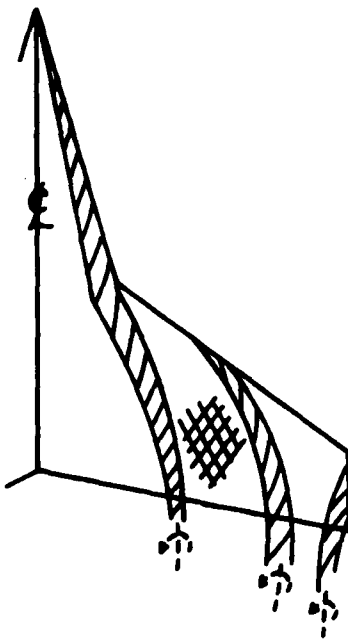
On a complete aircraft configuration other vortices may be present also, e.g., from a canard surface. The nature of the interaction between the wing surface and these "free" vortices is related to the strake-vortex interaction with the wing downstream from the leading-edge kink, and is an important



(a) UNSWEPT WING



(b) SWEPT WING



(c) CRANKED WING

Figure 2.1. Three Forms of Separated Flow on Wings.

ingredient in the calculation procedure, see Section 5.3. Beyond this, the nature of the real flow field can be further complicated by secondary vortices, shock-induced separations and also vortex breakdown, but these are beyond the scope of the present study.

The three examples of separated flow shown in Figure 2.1 form a natural progression in order of complexity for a study of theoretical modeling. Strictly, the theoretical treatment of these flow problems requires the full Navier-Stokes equations; however, practical solutions of these equations specifically for the complex geometry of actual configurations is still some time away (although some progress has been made with solutions of the Reynolds-averaged equations with turbulence modeling). In the meantime, simplifications of the flow-field model can be used in forming a practical approach to the problem for engineering purposes. For most flows of interest, the regions where viscosity has a significant effect are largely confined to thin shear layers, e.g., surface boundary layers and free shear layers. These shear layers have a displacement effect which can be modeled using source singularities and a tangential velocity discontinuity which is modeled by vortex or doublet singularities. The free shear layers cannot support a force and so the vorticity component normal to the local mean flow direction in the layer must be convected with the fluid. In the time-averaged sense, we assume that these "passing" normal vorticity components are constant at a particular location in the body-fixed coordinates. For a zero-force condition, the local static pressure is continuous through the free shear layer and so the jump in tangential velocity across the layer implies a jump in total pressure (Section 3.1) across the vortex sheet. The free edge of a vortex sheet rolls up into a vortex core which can be modeled using a potential vortex with a core model, e.g., a Rankine core or a viscous core superimposed to remove the infinite potential core velocity.

The flow model, therefore, reduces to a solid boundary (in this case, the wing surface) and a number of free vortex sheets embedded in a potential flow. A practical approach to solving this flow problem is to employ a surface singularity panel method with free vortex sheet wakes. The basic unknowns are the singularity strengths on the solid boundary and on the free vortex sheets and also the location of the latter; i.e., the spatial location of the vortex sheets and the location of the separation lines on the solid boundary. This is a highly non-linear problem requiring a multiple iterative approach, Figure 2.2. The inner iteration in the potential flow code computes the force-free vortex sheet locations with fixed separation lines. The outer iteration loop couples the potential flow and boundary layer modules. The latter computes the



location of separation lines and also provides the boundary layer displacement effect in the attached flow zones. This displacement effect is modeled in the potential flow calculation using the source transpiration model (Section 3.1).

The above procedure was assembled earlier in a two-dimensional program, CLMAX (5). Now in wide usage, this simple model--based primarily on vortex singularities, Figure 2.3, has proven to be a very practical yet effective tool for predicting aerodynamic characteristics over a wide range of angle of attack (5), (10), and after seven years, it remains superior to other separated flow models (10). Earlier disadvantages relating to compressibility effects have been removed in a transonic flow version (11). Also, the model has been applied in a multi-element program (12). More recently, it has been extended to the case of dynamic separated flows (13) using a time-stepping approach.

The vortex sheet model of the separated flow boundary (Figure 2.3) allows a direct calculation of velocities and pressures inside the separated wake region as well as in the external flow field. The singularity strengths, and, hence, surface velocities and pressures, on wing panels inside the separated zone are obtained as part of the basic solution and so the model does not require the assumption that the pressure is constant inside the separated zone. This is a definite advantage over other approaches which must make this assumption, e.g., the source outflow model (14) and displacement boundary models (15), (16) in order to obtain a complete surface pressure distribution for integrated force and moment information. In particular, the constant pressure assumption is not valid for the fully three-dimensional separations involving vortical flows. In this situation, the pressure at the wing surface can be quite different from the pressure at the effective displacement boundary. The vortex sheet model also offers a strong coupling (through the singularity influence coefficients) between the separation region boundary and the boundary conditions on the wing surface (and on any other surfaces present). This leads to good convergence characteristics in the iterative solution routines and is a key factor to successful applications on configurations with extensive separation zones. For example, Figure 2.4(a) shows good agreement between "CLMAX" calculated and experimental  $C_L \sim \alpha$  characteristics for a NACA 0012 in the  $\alpha$  range 0 to 90°. The converged computed wake shape and pressure distribution at  $\alpha = 90^\circ$  are shown in Figures 2.4(b) and (c). Certainly, the demonstrated wide angle-of-attack range of the vortex sheet model is a prerequisite for the fighter wing objective; methods without wake modeling or with weak viscous/inviscid interaction capability (e.g., (17), (18) and (19)) would be

REGION 1 - POTENTIAL FLOW REGION  
 REGION 2 - BOUNDARY LAYER  
 REGION 3 - FREE SHEAR LAYER  
 REGION 4 - WAKE

VORTEX SHEETS  
 REPRESENTING  
 FREE - SHEAR LAYERS

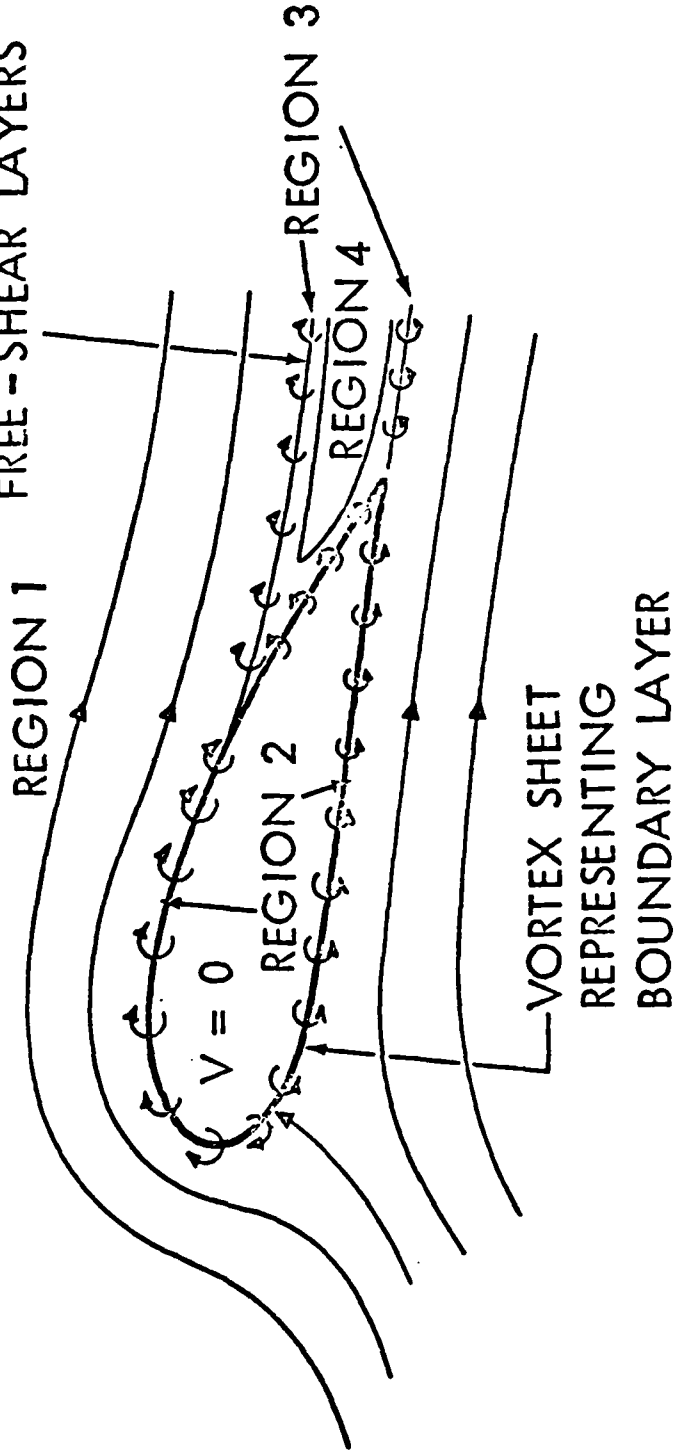


Figure 2.3. Vortex Sheet Model for Separated Flows.

(a) COMPARISON OF CALCULATED AND EXPERIMENTAL LIFT CHARACTERISTICS FOR A NACA 0012 AIRFOIL, REYNOLDS NUMBER  $6.0 \times 10^6$ , MACH NUMBER 0.2

● CLMAX CALCULATION



EXPERIMENT (FROM HOERNER, NACA TN 3361 etc.)

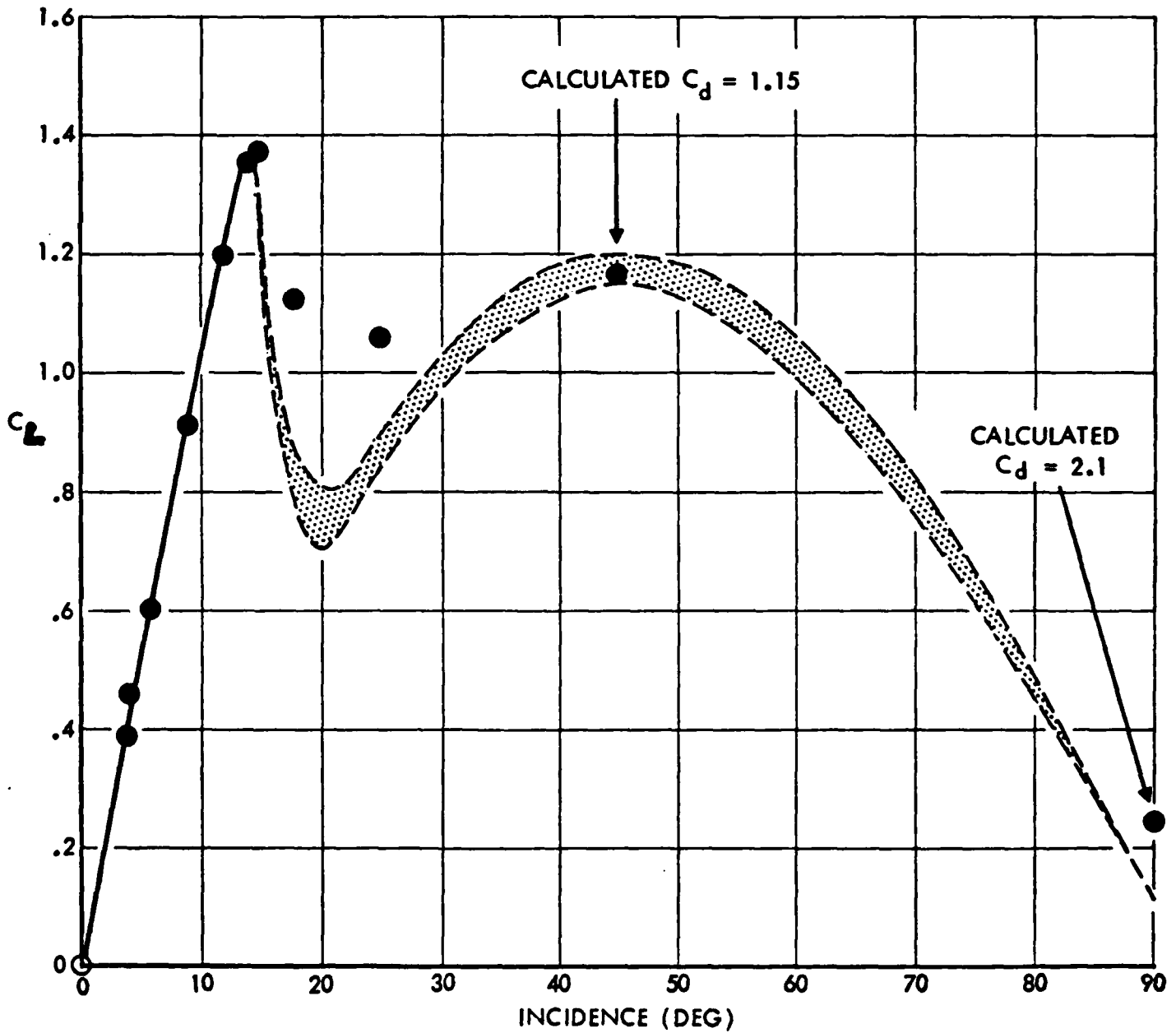


Figure 2.4. Calculations on a NACA 0012 over a Large  $\alpha$  Range.

(b) CALCULATED WAKE SHAPE FOR A NACA 0012 AT 90° INCIDENCE  
AFTER 6 VISCOUS/POTENTIAL FLOW ITERATIONS  
EACH WITH 3 WAKE SHAPE ITERATIONS

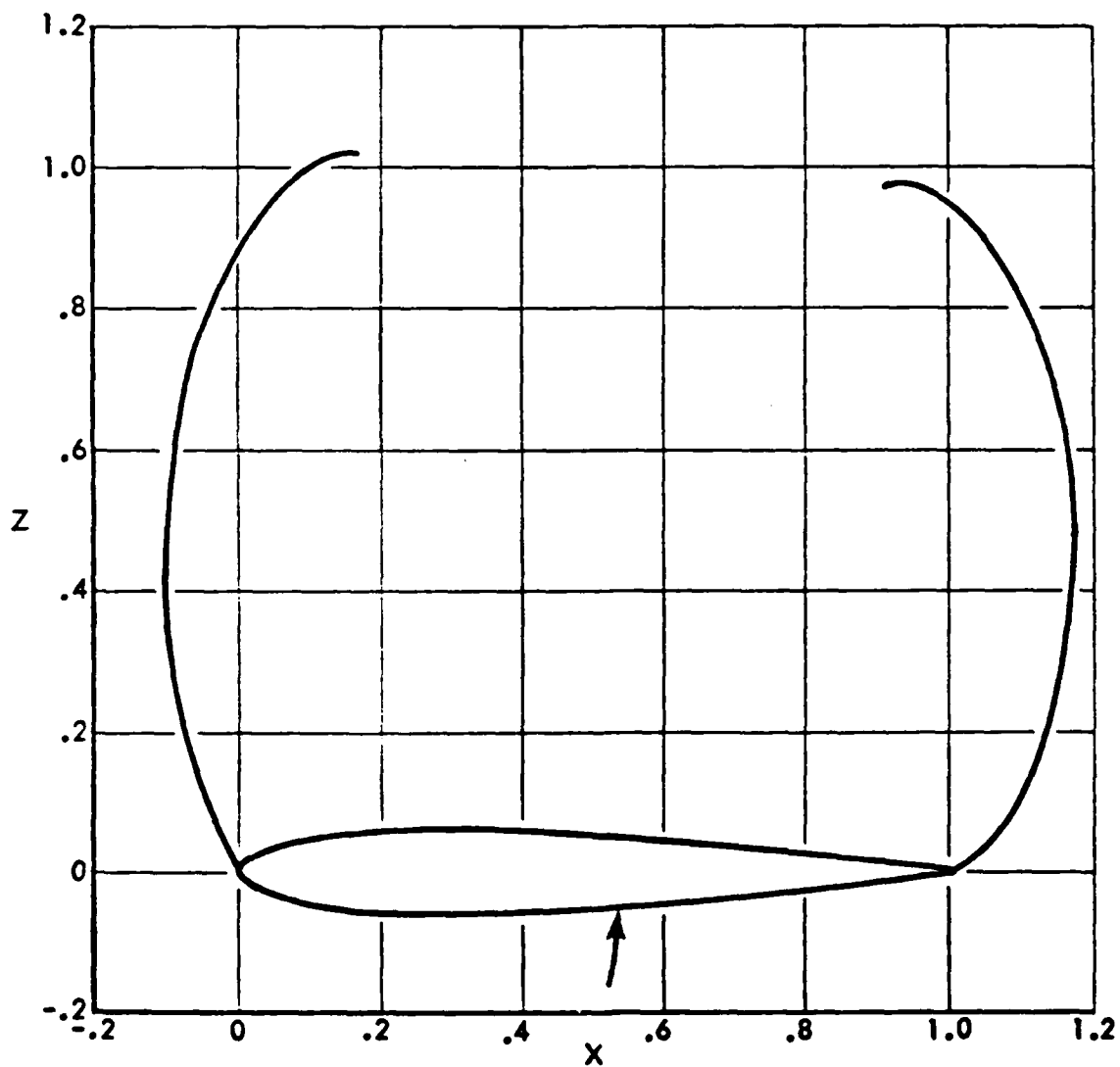
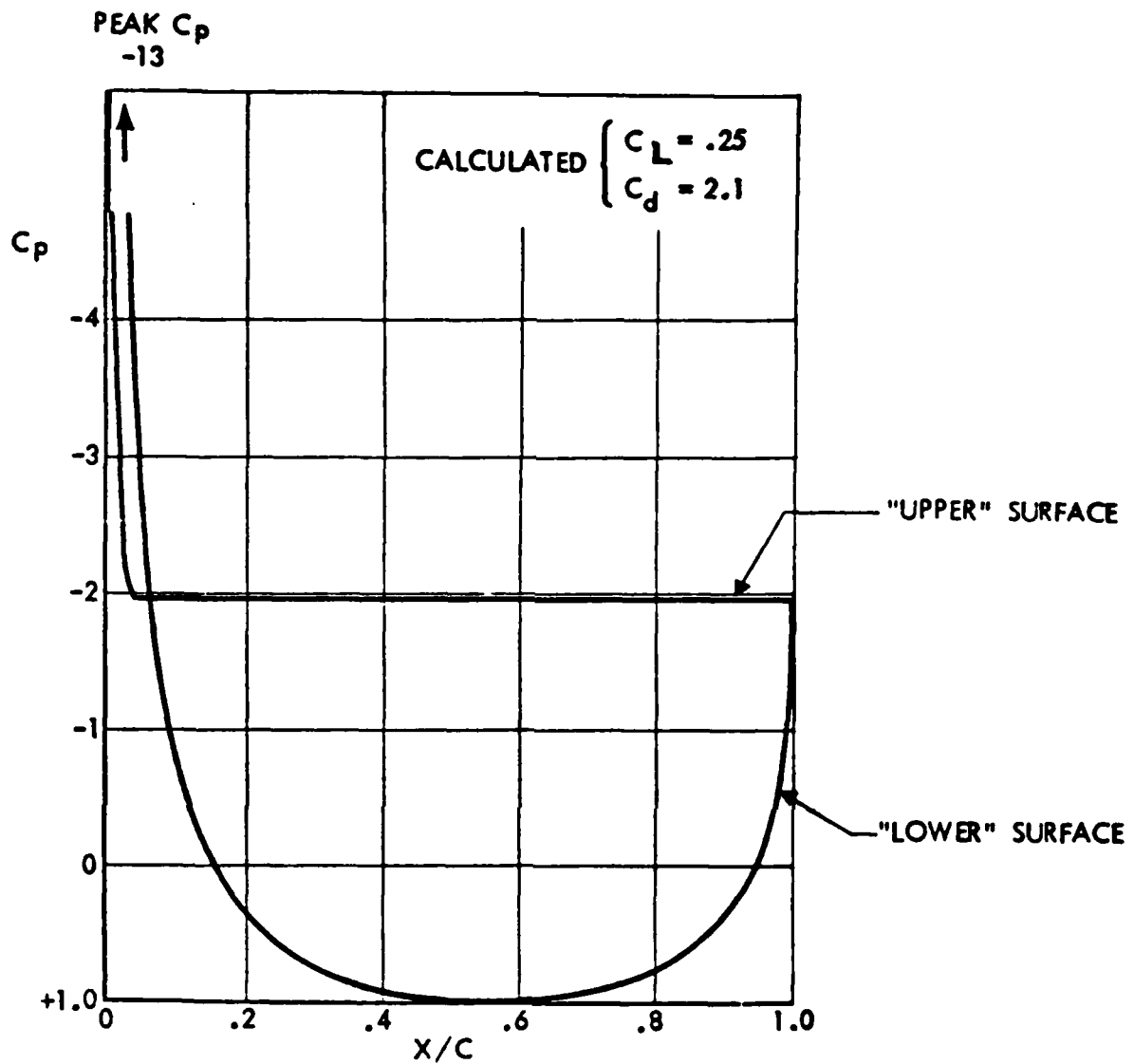


Figure 2.4. Continued.



(c) CALCULATED PRESSURE DISTRIBUTION ON A NACA 0012 AT 90° INCIDENCE,  
REYNOLDS NUMBER  $6.0 \times 10^6$ , MACH NUMBER 0.2

Figure 2.4. Concluded.

expected to break down when the separated flow region became extensive.

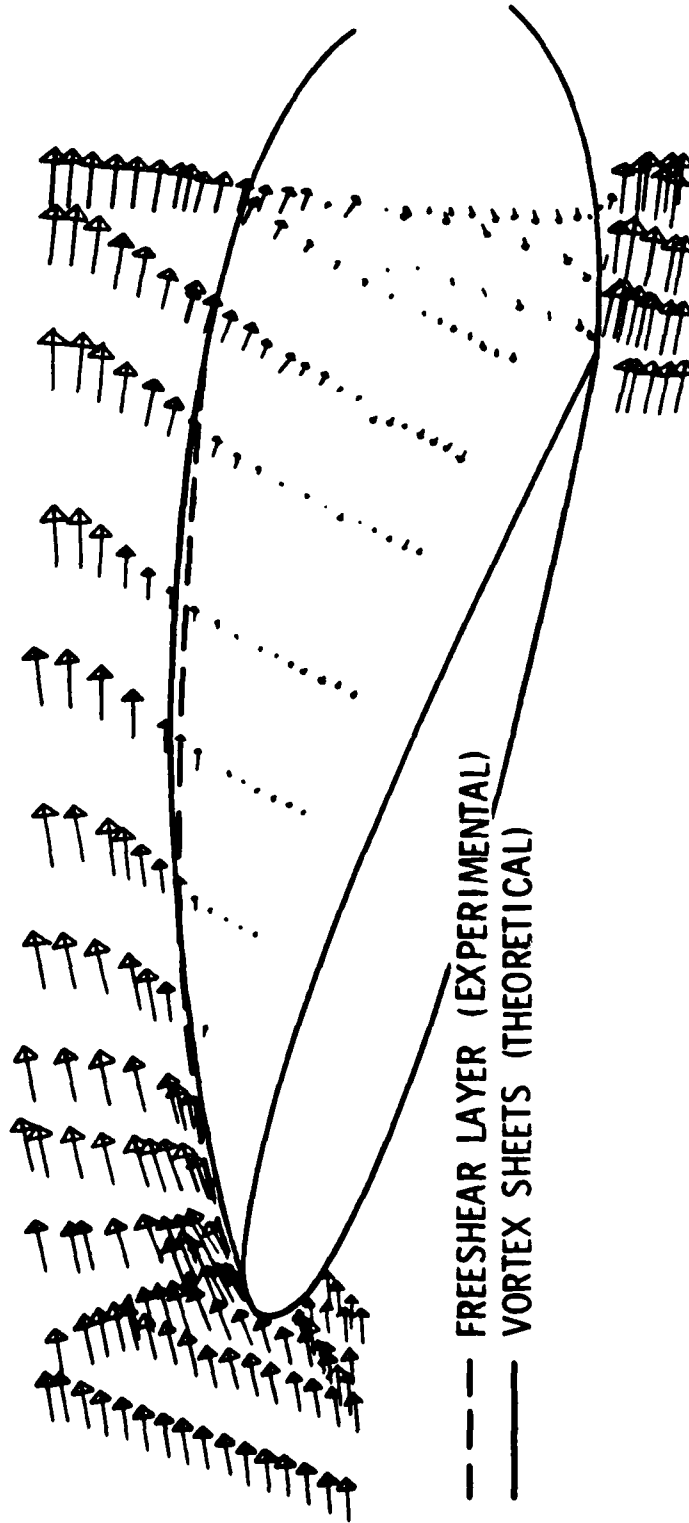
Thus, the vortex sheet model is the only logical choice for development of a practical procedure for treating extensive separated flows in three dimensions. The case for this model is strengthened further when considering separated flow modeling on multi-element wings and multi-component aircraft configurations. Within the current practical approaches to separated flow calculations, the vortex sheet model is the only one in which the low wake velocities are represented, e.g., see Figure 2.5 from the work of Young and Hoad (20), albeit with a simple velocity profile (Section 3.1). Thus, parts of the configuration immersed in the separated wake from an upstream component would automatically experience a reduced onset flow (Section 3.1). While this is not an immediate concern for the fighter wing objective, it is an important consideration in the choice of a suitable modeling technique with future development potential for treating complete combat aircraft configurations.

The vortex sheet separation model was extended to three dimensions in an exploratory program using a stripwise model approach (1). This method used surface singularity panels of linear vorticity chordwise and constant vorticity spanwise. The solution for each panel's vorticity value was obtained from a set of simultaneous linear equations satisfying the external Neumann boundary condition at a central control point on each panel. The wake sheets of constant vorticity representing the free-shear layers enclosing the separated region were forced to leave the surface at the panel edge nearest to the calculated separation point on each strip. Because of this, the separation line representation was not continuous, Figure 2.6, and so vertical gaps occurred between the strips. In the wake relaxation calculations, therefore, the wake lines along strip edges were constrained to move vertically only, otherwise roll-up would certainly occur at each strip edge. In spite of these simplifications, the feasibility of the approach was demonstrated and the complex structure for the iterative cycles (now involving multiple strips) was established. In any event, this simple stripwise model is applicable to essentially unswept wings (see also (21)), except in the vortical flow zone (Figure 2.1). In order to model the vortical flow regions a smoother representation of the separation line is desirable and the restrictions on the wake relaxation calculation must be removed.

Earlier calculations of the non-linear lift contribution from edge vortices on small aspect ratio wings were successfully obtained using a discrete vortex model of the separated zone (22), (23). The discrete vortex model has since been

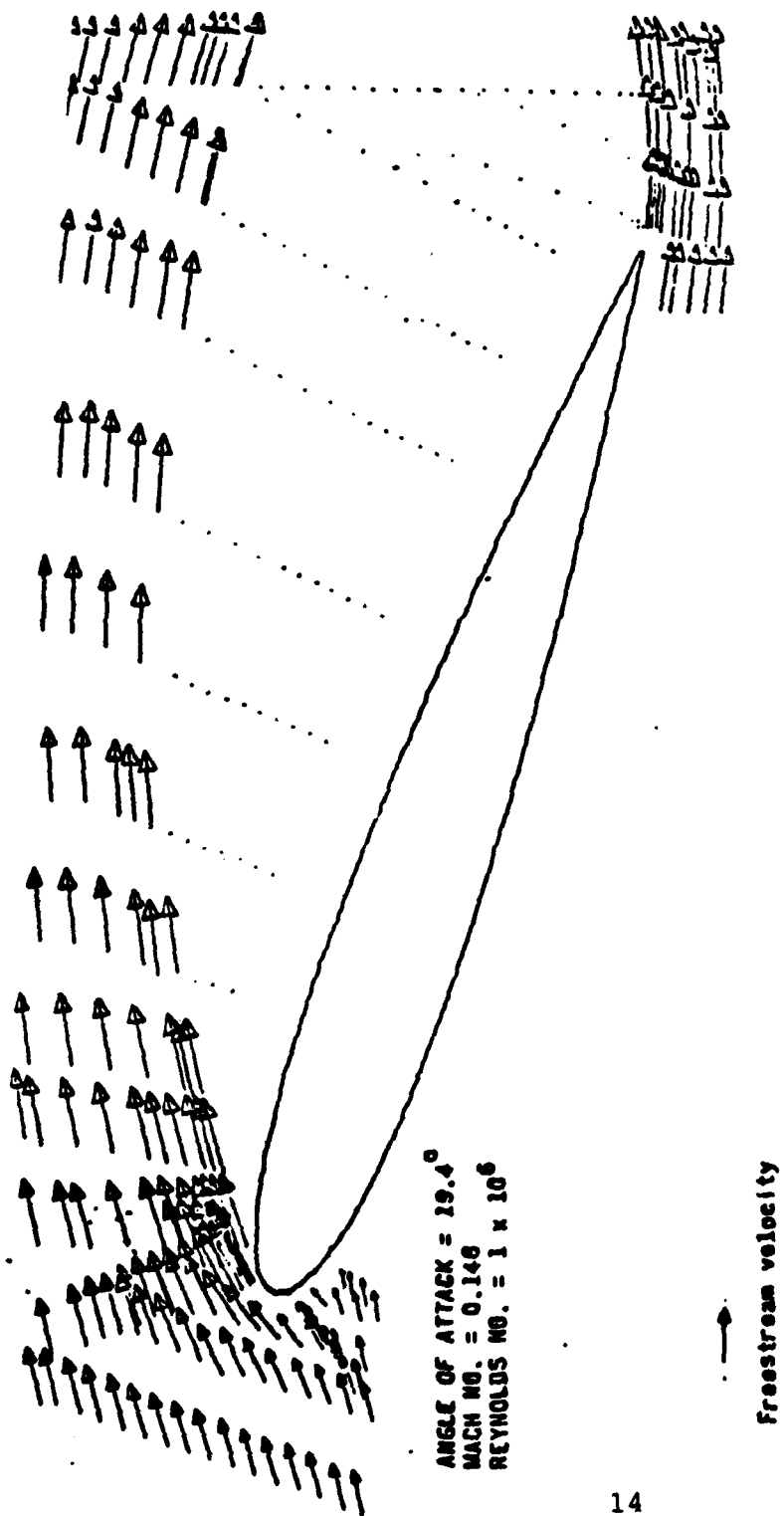
# SHEAR LAYER AND VORTEX SHEET CENTER LINES

MACH 0.148



(a) Comparison of Experimental Flow Field and Calculated Free Vortex Sheets.

Figure 2.5. Separated Flow on a NACA 0012.



(b) Calculated Velocity Vectors using The Method of Reference 4.

Figure 2.5. Concluded.

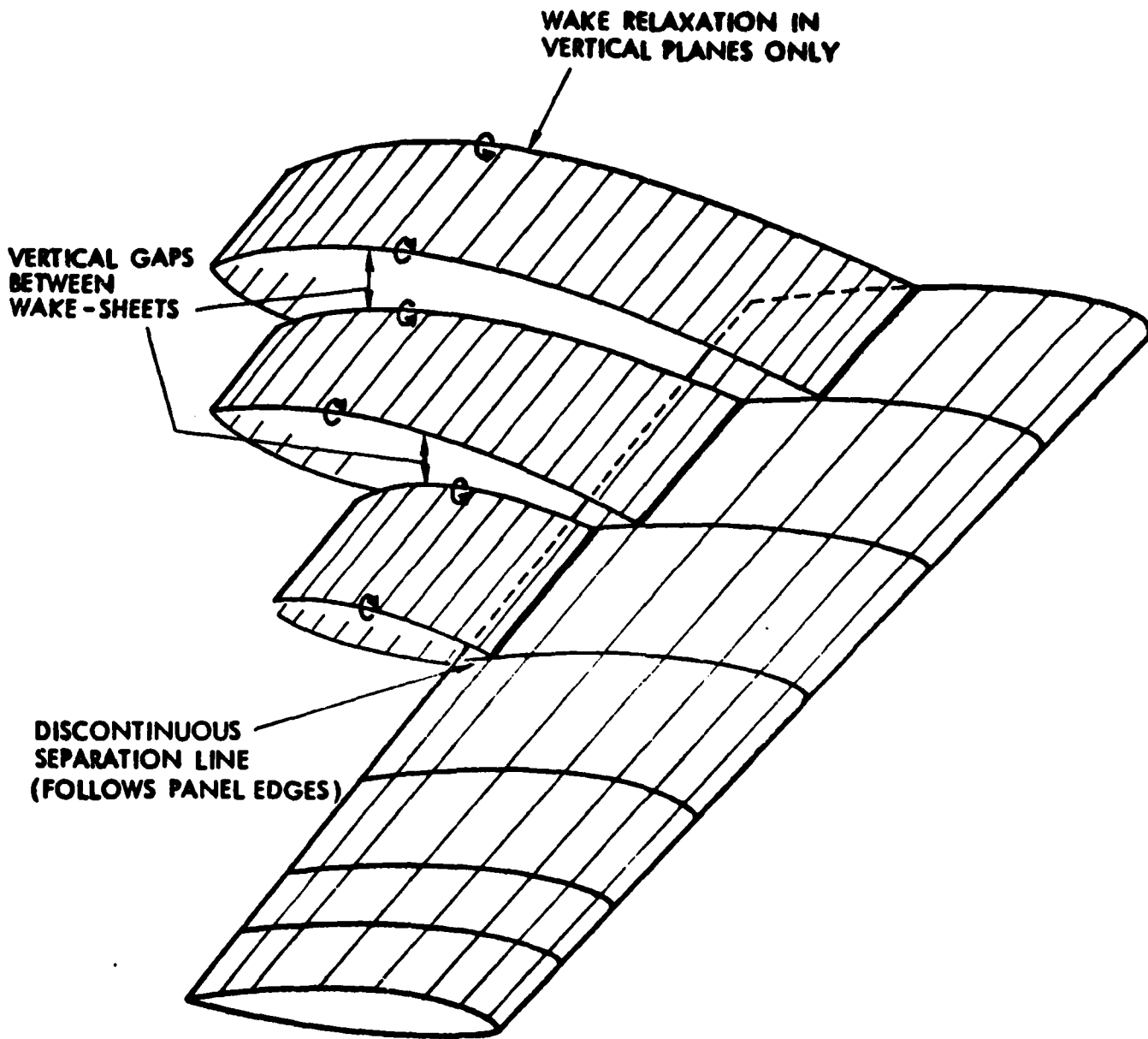


Figure 2.6. Basic Stripwise Separation Model from Reference 1.

successfully employed over a wide range of lifting problems in the so-called vortex-lattice method (see (24)). Although some care is required in the treatment of leading-edge vortices, there has been some success in both steady and unsteady solutions (25), (26). While the discrete vortex model is essentially a piecewise constant doublet sheet representation of the vortex sheets, a higher-order doublet distribution (e.g., (27)) would be expected to provide a more suitable modeling of the problem where the vortices pass close to surfaces. However, such models are significantly more expensive to run and numerical problems over convergence are still apparent, especially for more general planform shapes. Also, calculations of vortex/surface interaction using various models indicated that low-order techniques are adequate (28).

The above discussion of edge-vortex modeling concerns thin sharp-edged wings modeled by a single singularity sheet. Calculations of leading-edge vortices, from wings with thickness-modeled with a surface singularity panel method--have been less successful. One factor is certain; the calculation should be started with a reasonable approximation to the final vortex structure. For this purpose a preliminary investigation into calculating vortex/surface interaction resulted in an unsteady time-stepping program based on a surface singularity panel method with a growing free-vortex sheet routine (28). This was later applied to multiple cross-flow plane calculations using the unsteady cross-flow plane analogy to steady three-dimensional flow about slender configurations (28), (29). The technique is similar to that of Marshall and Deffenbaugh (30) for bodies of revolution except the present basis of a panel method in the cross-flow plane allows treatment of arbitrary shapes. In each of a series of cross-flow planes, therefore, the surface of the cross-section shape of the actual configuration is panelled. The "growth" term of this shape from plane to plane is included in the boundary conditions and the development of the vortex system is computed (28), (29). In the present work, this concept is examined further (Section 5.4) with a view to incorporating the unsteady cross-flow calculations as a preprocessor to the fully three-dimensional calculations. The objective is to generate a representative vortex structure for the initial solution, thereby reducing the number of iterations required in the large program and, hopefully, improving the convergence characteristics.

The free-vortex sheet separation model and the leading-edge vortex model are entirely compatible and promise a firm practical basis for treating fully three-dimensional separated flows with embedded vortical flow structures. In the present work, progressing from the preliminary stripwise model, it was decided to pursue the further development of this technique using the equivalent doublet sheet formulation and to adopt a new singularity panel method developed under a separate study (6). The new formulation is described in the next section.

### 3.0 THEORY

#### 3.1 Potential Flow Method

In Figure 3.1.1 we have taken a streamwise cut through the wing and its wake and, based on the earlier work (1), (4) have formed an idealized model using three closed regions: the wing interior (A), the bubble, or wake region (W) and the external region (E). The latter region is closed by an outer boundary,  $S_\infty$ . We assume the existence of velocity potential fields,  $\phi_A$ ,  $\phi_W$ ,  $\phi_E$  satisfying Laplace's equation throughout the regions A, W and E, respectively. By applying Green's third identity to each of these regions and combining the resulting contributions the velocity potential,  $\phi_P$ , at a point P situated within any of these regions can be written

$$\begin{aligned}
 \phi_P = & \frac{1}{4\pi} \iint_{S_{EA}} \left\{ (\phi_E - \phi_A) \underline{n}_E \cdot \nabla \left( \frac{1}{r} \right) - \frac{1}{r} \underline{n}_E \cdot (\nabla \phi_E - \nabla \phi_A) \right\} dS_{EA} \\
 & + \frac{1}{4\pi} \iint_{S_{EW}} \left\{ (\phi_E - \phi_W) \underline{n}_E \cdot \nabla \left( \frac{1}{r} \right) - \frac{1}{r} \underline{n}_E \cdot (\nabla \phi_E - \nabla \phi_W) \right\} dS_{EW} \\
 & + \frac{1}{4\pi} \iint_{S_{WA}} \left\{ (\phi_W - \phi_A) \underline{n}_W \cdot \nabla \left( \frac{1}{r} \right) - \frac{1}{r} \underline{n}_W \cdot (\nabla \phi_W - \nabla \phi_A) \right\} dS_{WA} \\
 & + \frac{1}{4\pi} \iint_{S_\infty} \left\{ \phi_E \underline{n}_\infty \cdot \nabla \left( \frac{1}{r} \right) - \frac{1}{r} \underline{n}_\infty \cdot \nabla \phi_E \right\} dS_\infty
 \end{aligned} \tag{3.1.1}$$

where  $S_{EA}$  represents the surface of the common boundary between regions E and A with unit surface normal  $\underline{n}_E$  directed into region E (i.e.,  $\underline{n}_A = -\underline{n}_E$ , etc.), and so on. The quantity,  $r$ , is the distance between the element of surface,  $dS_{EA}$ , and the point P (Figure 3.1.1).

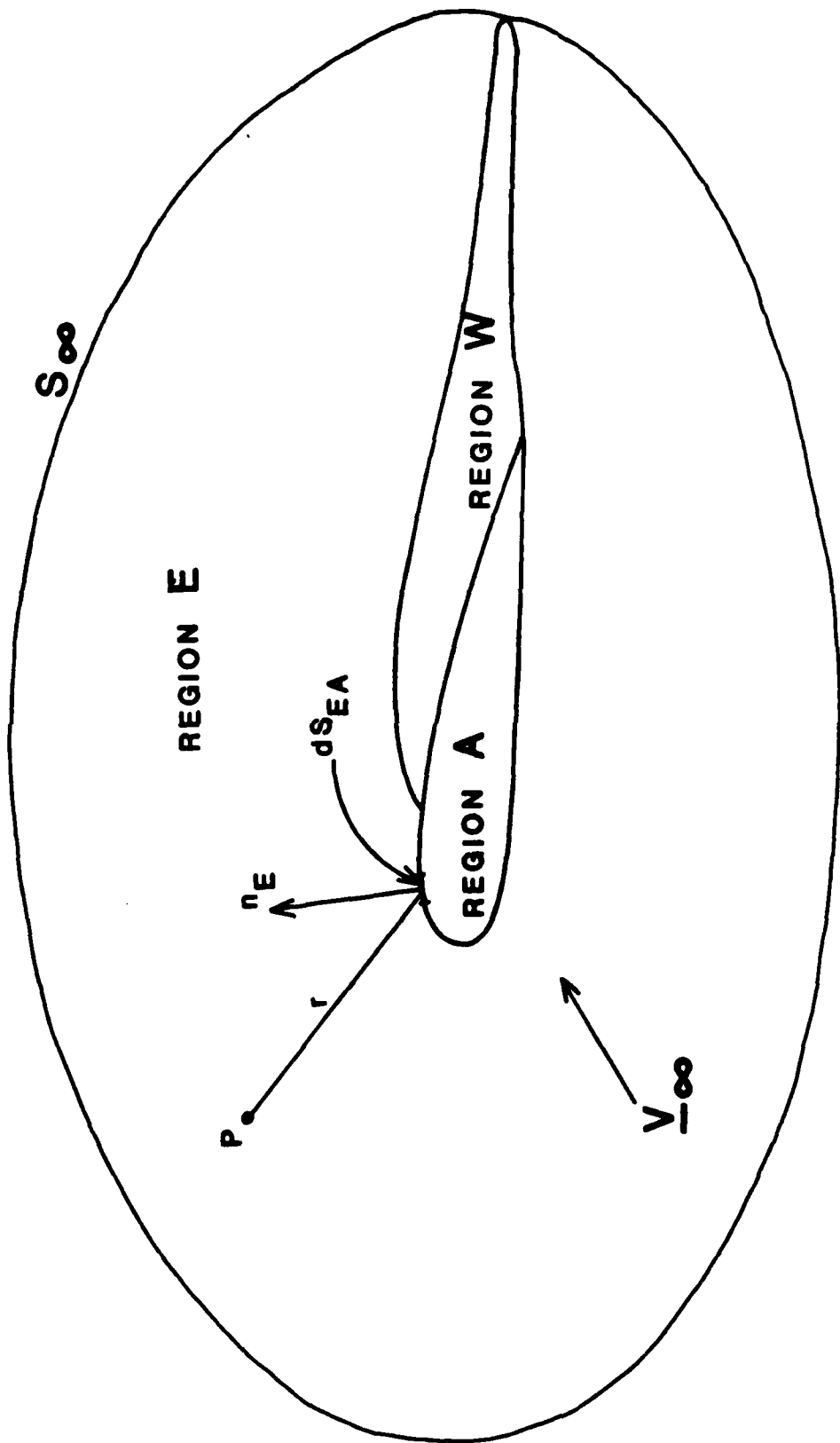


Figure 3.1.1.1. Idealized Flow Model--Section through the Wing and its Wake.

Equation 3.1.1 is an extension of the two-region case given by Lamb (31). In the present case we assume a uniform onset flow with velocity potential  $\phi_\infty$ . The contribution from the last term in Eqn. 3.1.1 can then be evaluated assuming a very large spherical surface centered on P.

Thus,

$$\frac{1}{4\pi} \iint_{S_\infty} \left\{ \phi_E \underline{n}_\infty \cdot \nabla \left( \frac{1}{r} \right) - \frac{1}{r} \underline{n}_\infty \cdot \nabla \phi_E \right\} dS_\infty = \phi_{\infty P} \quad (3.1.2)$$

where  $\phi_{\infty P}$  is the onset flow velocity potential evaluated at P.

If the point P lies on one of the surfaces, say on surface  $S_{EA}$  facing region E, then the local surface contribution becomes singular. However, a limiting process using a small hemispherical distortion of the surface centered on P yields a local contribution from the first term under the integral of

$$\nabla \phi_P = \frac{(\phi_E - \phi_A)_P}{2} \quad (3.1.3)$$

for a smooth surface. This is half the jump in potential across the surface at point P. The surface integral over  $S_{EA}$  in Eqn. 3.1.1 would exclude point P in this case. A similar treatment is performed if P lies on any of the surfaces, noting that the first potential appearing in the expression for  $\Delta \phi_P$  in Eqn. 3.1.3 is the one in the region to which point P is "facing".

Each of the integral expressions in Eqn. 3.1.1 represents the perturbation potential due to distributions of doublets and sources over the respective boundaries. For example, the first integral is the perturbation potential for a doublet distribution of strength  $(\phi_E - \phi_A)$  on the boundary  $S_{EA}$  and with axes  $\underline{n}_E$ , plus the perturbation potential for a source distribution of strength  $-\underline{n}_E \cdot (\nabla \phi_E - \nabla \phi_A)$ .

Within each of the closed regions there exists an infinite number of doublet and source distributions on the boundary surface which give the same flow solution within that region but they produce different solutions in the other regions. Thus a unique distribution of the doublets and sources is obtained only when the boundary conditions are imposed on both

sides of each boundary surface--or, alternatively, when one singularity distribution is prescribed and the boundary condition is applied on one side of the boundary. In the latter case, care must be exercised in the choice of the prescribed singularity distributions, otherwise numerical problems can appear which seriously affect the accuracy of the solution.

In the present case, the following boundary conditions are applied.

(i) On the outside surface of the wing we control the normal velocity component, i.e., the external Neumann boundary condition. The wing surface is basically in two parts: the boundary between regions E and A (i.e., the attached flow zone) and the boundary between W and A (i.e., the separated zone). In a practical case, each of these parts could be further subdivided if there were multiple separated zones.

- (a) In the attached flow zone,  $S_{EA}$ , facing region E, we set the normal velocity equal to the rate of growth of boundary layer displacement

$$\underline{n} \cdot \nabla \phi_E = - \partial/\partial s (U_e \delta^*) \quad (3.1.4)$$

i.e., the transpiration model for boundary layer displacement effect. The right-hand side of this equation is usually set to zero for the initial solution and is subsequently updated by boundary layer calculations along computed external streamlines in an iterative procedure.

- (b) In the separated zone,  $S_{WA}$ , facing region W, we set the normal velocity to zero.

$$\underline{n} \cdot \nabla \phi_W = 0 \quad (3.1.5)$$

(ii) The details of the flow field inside the wing (region A) are of no practical interest and so we can prescribe any reasonable potential flow there. In earlier work the internal flow was set to zero, i.e.,  $\phi_A = \text{constant}$ . This is an internal Dirichlet boundary condition. For the basic case of attached flow on a simple configuration this removes the source term in Eqn. 3.1.1. This is by far the simplest and most economical formulation (32), and with panels of constant doublet distributions results in a lattice of surface quadrilateral vortices (e.g., paper No. 10 in Ref. 24). However, some care must be exercised in panel matching where surfaces come close together. A more benign singularity model results when the internal flow is set equal to the uniform onset flow,

$$\phi_A = \phi_w; \quad (3.1.6)$$

i.e., zero perturbation exists inside the wing. This condition was implied by Morino (33) when he applied Green's theorem directly to the exterior flow field. It was used by Johnson and Rubbert (34) and also by Bristow (35).

(iii) On the boundary,  $S_{EW}$ , we are interested in the flow field on both sides of the surface, i.e., the external and the wake regions. The primary boundary condition here is that the surface is essentially a force-free stream surface of the flow. Some flow normal to the surface may be allowed in the modeling of entrainment, i.e.,

$$\underline{n}_E \cdot \nabla \phi_E = v_e \quad (3.1.7)$$

If we let  $v_e$  be continuous across the boundary, then  $\underline{n}_E \cdot \nabla \phi_W = v_e$  and the source term,  $\underline{n}_E \cdot (\nabla \phi_E - \nabla \phi_W)$  in the second integral in Eqn. 3.1.1 disappears, leaving only doublet singularities on the wake boundary,  $S_{EW}$ . Alternatively, we can make  $v_e$  discontinuous across  $S_{EW}$ ; this would require source singularities as well as doublet singularities on surface  $S_{EW}$ , and would allow modeling of the displacement effect of the free shear layer. For the present investigation, entrainment will not be considered and so  $v_e$  will be set to zero in Eqn. 3.1.7.

Whatever the modeling on the wake, the normal velocity condition cannot be specified explicitly at the outset because the location of the boundary is unknown. Rather, the Neumann boundary condition must first be implied using an initially prescribed wake and then satisfied indirectly in an iterative procedure in which the boundary,  $S_{EW}$ , is moved to coincide with a computed mean streamline surface.

With the appropriate boundary condition applied in the idealized model, the internal Dirichlet boundary condition, Eqn. 3.1.6, is applied at points P on the inside surface of the wing. Equation 3.1.1 becomes

$$0 = \frac{1}{4\pi} \iint_{S_{EA}} \left\{ \phi_E \underline{n}_E \cdot \nabla \left( \frac{1}{r} \right) - \frac{1}{r} \left( - \frac{\partial}{\partial s} (U_e \delta^*) + \underline{n}_E \cdot \underline{v}_w \right) \right\} dS_{EA}$$

$$\begin{aligned}
& + \frac{1}{4\pi} \iint_{S_{WA}} \left\{ \phi_W \underline{n}_W \cdot \nabla \left( \frac{1}{r} \right) - \frac{1}{r} \underline{n}_W \cdot \underline{V}_\infty \right\} dS_{WA} - \frac{\phi_P}{2} \\
& + \frac{1}{4\pi} \iint_{S_{EW}} \mu_W \underline{n}_E \cdot \nabla \left( \frac{1}{r} \right) dS_{EW}
\end{aligned}
\tag{3.1.8}$$

where  $\phi_E = \phi_E - \phi_\infty$  is the perturbation potential. The integral over  $S_{EA}$  and  $S_{WA}$  excludes the point, P, when it lies on that part of the boundary. The wake doublet distribution,  $\mu_W (= \phi_E - \phi_W)$  is the jump in potential across the surface,  $S_{EW}$ . This distribution is related to the conditions of the doublet and its gradient (i.e.,  $\underline{\gamma}$ ) on the wing surface at the separation line as described below.

At the location of separation, i.e., where boundary  $S_{EW}$  meets boundary  $S_{EA}$ , we assume that the total surface vorticity vector normal to the local mean velocity is shed into the free-shear layer. This is essentially a zero-load condition at the beginning of the free shear layer. At the outset, of course, neither the mean flow direction nor the vorticity vector are known. The calculation is therefore started with the assumption of stationary flow under the free shear layer at separation--this is essentially the model used in the two-dimensional model (4), i.e.,

$$\gamma_{SEP} = - \left. \frac{\partial \phi_E}{\partial s} \right|_{SEP}$$

The derivative in the external flow is with respect to distance,  $s$ , measured in the direction of the mean flow which is initially assumed and thereafter should be updated in the iteration cycle.

In previous work (1), (4) the initial value for  $\gamma_{SEP}$  was held constant along the free shear layers (i.e., constant doublet gradient). This simple assumption proved reasonable at least for the influence of the free shear layers acting on the wing, itself (e.g., Figure 2.5 from Young and Hoad (20)) and is a reasonable assumption for the initial solution. However, it would be expected to break down in more general multiple component cases because the computed velocity inside

the wake region remains very small (typically  $V_W/V_\infty < .1$ ) for the total extent of that wake model and that is not very representative of the real flow. For the general case, therefore, a more complete description of the wake vorticity distribution is required. However, in the three-dimensional case, both the magnitude and direction of the wake vorticity vector is unknown at the outset.

Consider a local orthogonal coordinate system at a point on the boundary,  $S_{EW}$ , Figure 3.1.2. Unit vectors  $\underline{l}$  and  $\underline{m}$  are tangent to the boundary, with  $\underline{l}$  being in the direction of the local mean flow;  $\underline{n}$  is normal to the boundary and is directed into the external flow region (i.e.,  $\underline{n} \equiv \underline{n}_E$  here). The velocity vectors on either side of the sheet at this point are  $\underline{V}_E$ ,  $\underline{V}_W$  the mean velocity,  $\underline{\bar{V}}$ , which by definition is parallel to  $\underline{l}$  is, therefore,

$$\underline{\bar{V}} = \left( \frac{\underline{V}_E + \underline{V}_W}{2} \right) = \underline{\bar{V}} \underline{l} \quad (3.1.9)$$

The velocity shear across the boundary is

$$\underline{\delta V} = \underline{V}_E - \underline{V}_W = \underline{\gamma} \wedge \underline{n} \quad (3.1.10)$$

where  $\underline{\gamma}$  is the local vorticity vector.

From Eqn. 3.1.9 and 3.1.10 we can write

$$\begin{aligned} \underline{V}_E &= \underline{\bar{V}} + \underline{\delta V}/2 \\ \underline{V}_W &= \underline{\bar{V}} - \underline{\delta V}/2 \end{aligned} \quad (3.1.11)$$

Next, apply the Bernoulli equation on the two sides of the boundary. The wake surface cannot support a force and so the static pressure must be continuous across this boundary, but, because there is a discontinuity in tangential velocity across the surface, then we anticipate a jump,  $\Delta H$ , in total pressure. Thus

$$\frac{1}{2} \rho V_E^2 = \frac{1}{2} \rho V_W^2 - \Delta H$$

or 
$$\Delta H = \frac{1}{2} \rho (V_W^2 - V_E^2)$$

and using Eqn. 3.1.11 for  $\underline{V}_E$  and  $\underline{V}_W$

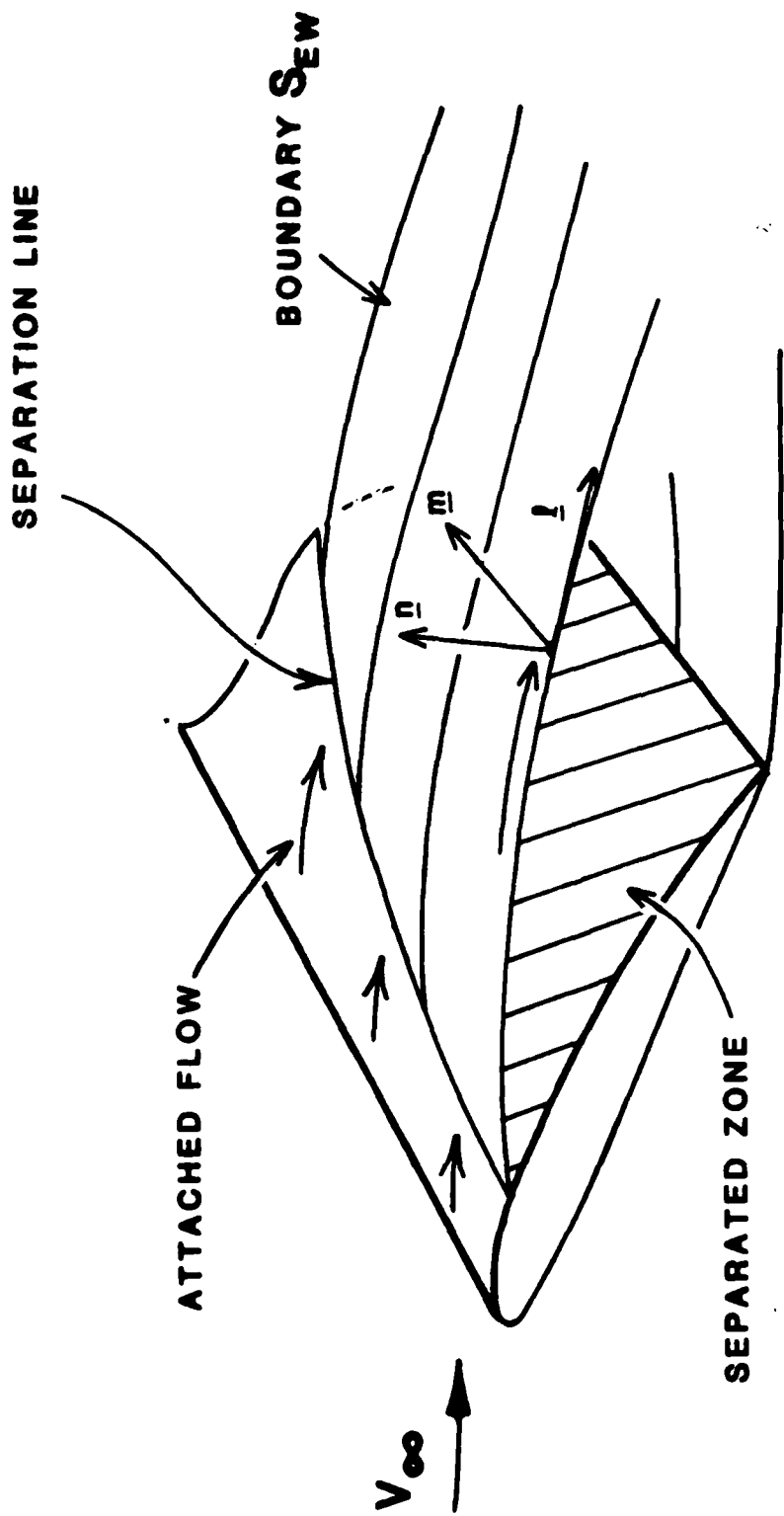


Figure 3.1.2. Local Coordinate System on a Wake Line.

$$\Delta H = -\rho \bar{V} \cdot \delta V$$

and using Eqns. 3.1.9 and 3.1.10, we can write

$$\frac{\Delta H}{\rho} = -\bar{V} \gamma_m \quad (3.1.12)$$

where  $\gamma_m$  ( $= \underline{\gamma} \cdot \underline{m}$ ) is the vorticity component normal to the local mean flow direction.

Equation 3.1.12 can be used to evaluate  $\Delta H/\rho$  at points along the separation line. After a doublet solution (based on an initial prescribed wake) we can compute mean local velocity vectors,  $\bar{V}$ , on the boundary,  $S_{EW}$ , and align wake lines in that boundary to follow essentially mean streamlines on a segment by segment basis. If we assume the value of the total pressure jump remains constant along each of these lines (i.e., keeping the value determined at the separation line for each wake line) then we can compute the local transverse vorticity component by rearranging Eqn. 3.1.12. Thus, at a point distance,  $s$ , along one of these wake lines (Figure 3.1.2)

$$\gamma_m(s) = - \frac{\Delta H}{\rho \bar{V}(s)}$$

or

$$\gamma_m(s) = - \bar{V}_{SEP} \gamma_{mSEP} / \bar{V}(s) \quad (3.1.13)$$

Finally, we can integrate along that line to evaluate the doublet distribution,  $\mu_W$ , starting with the separation value

$$\mu_W(s) = \mu_{WSEP} - \int_0^s \gamma_m(s) ds$$

or, using Eqn. 3.1.13,

$$\mu_W(s) = \mu_{WSEP} + \bar{V}_{SEP} \gamma_{mSEP} \int_0^s \frac{ds}{\bar{V}(s)} \quad (3.1.14)$$

The integral in Eqn. 3.1.14 essentially defines a weighting function for the doublet distribution along that wake line on surface,  $S_{EW}$ , relative to the conditions at separation. This provides a way to use the shape of the previous distribution in the next solution. In the earlier work (1), (4), the details of this distribution were not included and so the doublet gradient (i.e.,  $\gamma$ ) was held constant along the sheet.

### 3.2 Streamline Analysis

The calculation of streamlines and related flow variables requires the construction of a potential distribution which is continuous and differentiable throughout the body surface. The direct evaluation of potential at every point on the body surface is not always feasible because of the singular nature of the kernel function near the panel boundaries. A numerical procedure is, therefore, required to derive the flow variables from the calculated value of the potential at the control point of each panel.

In the literature, investigators generally regard the method of splines as an adequate answer to many interpolation problems. Cubic splines in one dimension are known to be an effective means of numerical interpolation, differentiation and integration. In the context of the present analysis, however, they are not appropriate because the implied cubic form of interpolation for the velocity potential forces a spatial dependence of velocity components that can violate the condition of zero curl. The velocity potential is known at discrete points whose three positional coordinates in a Cartesian frame of reference can vary quite arbitrarily. On a smooth surface which can be analytically expressed, the three positional coordinates can be reduced to two coordinates by means of the equation expressing the relationship of the points on the surface. The same is not true for a general aircraft configuration with surface discontinuity, slope discontinuity, kinks, corners and arbitrarily shaped fixtures. The velocity potential must, therefore, be considered as a function of three Cartesian coordinates and the assumed nature of the interpolating must not introduce rotationality in the flow. To elucidate the ideas regarding the development of an appropriate interpolating function, the following discussion is presented.

Let us assume that the surface streamlines of a three-dimensional body entirely pass through the nearly planar region of each panel. The path of each streamline on a panel follows from the condition that the tangent to the streamline is in the direction of the local velocity vector. Within a

panel the equation describing the streamline originating from a point can be obtained by integrating Eqn. (3.2.1) below where  $ds$  is an infinitesimal incremental vector

$$V_x ds = 0 \quad (3.2.1)$$

along the streamline. When the spatial dependence of  $V$  is substituted in Eqn. (3.2.1), the geometrical relationship between the positional coordinates of the points on a streamline become known within a panel. For a local Cartesian coordinate system in the plane of the panel, Eqn. (3.2.1) reduces to Eqn. (3.2.2) where  $V_x$  and  $V_y$  are components of velocity in the plane of the panel.

$$\psi = \int (V_x dy - V_y dx) \quad (3.2.2)$$

The third component of velocity normal to the plane of the panel does not appear in the above equation because it is assumed that the streamlines are attached. The conditions for the integrability of Eqn. (3.2.2) become satisfied if the divergence of the in-plane velocity vector equals zero. This would imply that the velocity potential within the region of a panel must satisfy the Laplace equation in the two dimensions of the planar panel. Since the velocity potential already satisfies the Laplace equation in three dimensions as required by the assumption of potential flow, the present requirement causes the second derivative of the velocity potential with respect to the normal coordinate to go to zero. The latter result is non-physical because the rate of change of the velocity component normal to the body surface in the direction of the normal depends on the local body curvature and is certainly not zero in general. However, having assumed the curvature of the panel to be equal to zero, i.e., a flat panel, it is no wonder that any potential distribution on it cannot predict the second normal derivative of the potential. The inability to calculate the second normal derivative of potential is, therefore, not an unacceptable limitation.

To further clarify the point, take the familiar example of a space curve discretized by  $N$  straight-line segments. Each straight-line segment has zero curvature (i.e., an infinite radius of curvature); but that does not invalidate the straight-line approximation although it results in zero curvature locally everywhere. Moreover, the true curvature can be computed to any desired degree of accuracy by including a sufficiently large number of straight segments. In the limit of  $N$  tending to infinity the flat regions tend to zero enabling

the recovery of correct behavior on the physical body. Even with finite  $N$ , the global properties can be well approximated by an ensemble of piecewise flat regions which individually do not reflect all the global properties.

The basic problem is the construction of an interpolation polynomial which assumes prescribed values at four arbitrarily placed by non-colinear points. In general, the distribution will depend on the assumed form of the interpolating function. An idea of the appropriate form of the interpolating function can be inferred by assuming the velocity potential in the plane of the panel to be harmonic. It is known from the potential theory that the problem of determining the potential within a planar region is well posed when the potential is specified all along the perimeter of the region. In the present problem, since the value of the potential is known only at the four corner points, an assumption is necessary as to the variation of potential between the corner points. Assuming linear variation in potential between corner points, we have a well-posed problem in potential theory with continuity of potential in the linear region common to two subdomains. Even with such simplifying assumptions, the problem of determining the potential distribution for a general quadrilateral region is a very difficult one because of the presence of corners (i.e., kinks) in the boundary. There is, however, an explicit polynomial construction scheme which directly provides the correct distribution.

### 3.2.1 Construction of the Interpolation Function

Let  $\phi_1, \phi_2, \phi_3$  and  $\phi_4$  be the velocity potentials at four points with the positional coordinates in the tangent plane to the body surface denoted by  $(x_1, y_1), (x_2, y_2), (x_3, y_3)$  and  $(x_4, y_4)$  as shown in Figure 3.2.1. It can now be verified by direction substitution that the following interpolating function for  $\phi$  assumes prescribed values at the specified locations and is harmonic with second-order terms.

$$\begin{aligned} \phi = & \phi_2 + (x - x_2)B_1 + (y - y_2 - m_1(x - x_2))B_2 \\ & + \left[ ((y - y_2) - m_2(x - x_2)) \right. \\ & \left. ((y - y_4)m_2 + (x - x_4)) \right] B_3 \end{aligned} \quad (3.2.3)$$

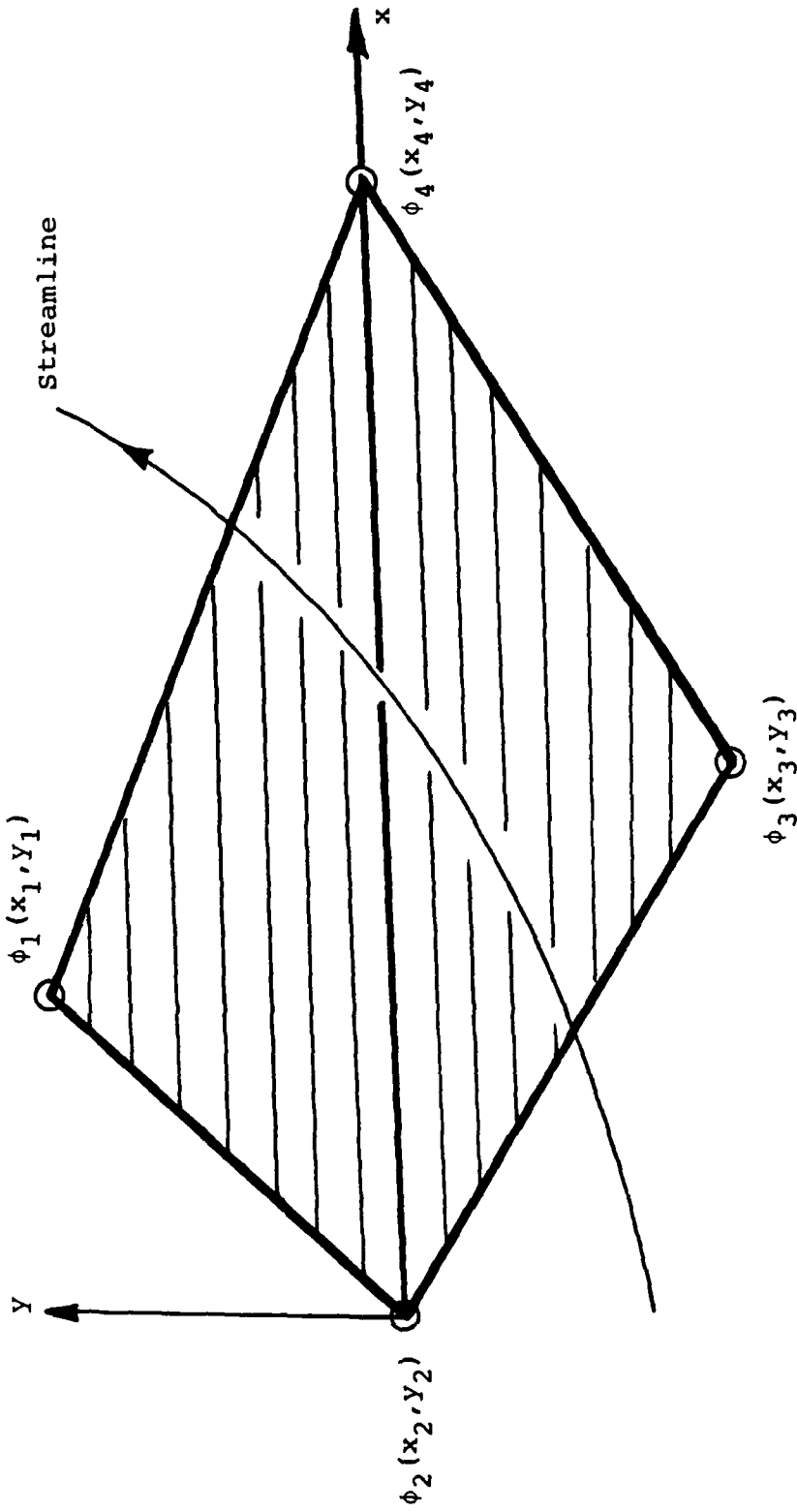


Figure 3.2.1. Coordinate System in Tangent Plane-to-Body Surface and Region Covered by Basic Four-Point Interpolation Scheme.

where

$$B_1 = \frac{\phi_4 - \phi_2}{x_4 - x_2} \quad (3.2.4)$$

$$B_2 = \frac{(\phi_3 - \phi_2 - B_1(x_3 - x_2))}{(y_3 - y_2 - m_1(x_3 - x_2))} \quad (3.2.5)$$

$$B_3 = \frac{(\phi_1 - \phi_2 - B_1(x_1 - x_2) - B_2(y_1 - y_2))}{(y_1 - y_2 - m_2(x_1 - x_2))((y_1 - y_4)m_2 + x_1 - y_4)} \quad (3.2.6)$$

$$m_1 = \frac{y_4 - y_2}{x_4 - x_2} \quad (3.2.7)$$

$$m_2 = \frac{y_3 - y_2}{x_3 - x_2} \quad (3.2.8)$$

$$t_1 = y - y_2 - m_2(x - x_2) \quad (3.2.9)$$

$$t_2 = (y - y_4)m_2 + x - x_4 \quad (3.2.10)$$

The first three terms of the function in Eq. (3.2.3) are straightforward, being simply obtained from the requirement that  $\phi$  assume the specified values at points 2, 3 and 4 with a linear dependence on  $x$  and  $y$ . The structure of the fourth term is very important because it serves to satisfy the following three objectives. It

1. yields the specified values of  $\phi$  for  $x = x$  and  $y = y$  ;
2. determines the second-order terms in the interpolation function; and
3. ensures the zero divergence of the velocity components in the tangent plane to body surface ( $x$ - $y$  plane) which facilitates the integration of the streamline equation. necessary condition for locally tangential attached streamlines.

Further, the fourth term implies that on two mutually orthogonal directions represented by  $t_1$  and  $t_2$ , the variation of  $\phi$  becomes linear.

When the four corner points are the corners of a rectangle, the equations (3.2.8) through (3.2.10) become

$$M_2 = -\tan 45^\circ = -1$$

$$t_1 = y + x = y_2 + x_2$$

$$t_2 = x - y = x_4 + y_4$$

The directions implied by  $t_1$  and  $t_2$  are the two sides of the rectangle, respectively, and the potential distribution (3.2.3) reduces to

$$\phi = a_0 + a_1 t_1 + a_2 t_2 + a_3 t_1 t_2$$

where  $a$ 's are known functions.

For fixed  $t_1$  or  $t_2$ , the variation of the potential is linear in  $t$  and  $t$ , respectively. Thus the solution given in Eqn. (3.2.3) is an exact solution for the problem of finding the potential distribution inside a rectangle when the variation of potential along the perimeter is assumed to be linear. By invoking the property of harmonic potentials, it may be

categorically asserted that there is a one and only solution to a well-posed problem (well-posedness arises from the assumption of linear variation along the boundary) and the solution found being "a solution" must be "the solution".

For a general quadrilateral figure, the solution given in Eqn. (3.2.3) amounts to an exact solution of the two-dimensional Laplace equation for a rectangular region whose sides are parallel and perpendicular to side 2-3 (of Figure 3.2.1) with the connector of points 2 and 4 as diagonal. The choice of side 2-3 as one of the orthogonal directions along which linear variation of potential is assumed raises the question of whether or not uniqueness is marred by this particular selection. The answer is that the assumed interpolation function will ordinarily depend on the choice of side for defining  $m_2$  except in the special case when specified values of the velocity potential satisfy a certain compatibility relation. When the prescribed values of the velocity potential represent a velocity field which yields the same value for the velocity vector at the inner center of the region of interpolation regardless of the direction from which the inner center is approached, the apparent arbitrariness in the choice of  $m_2$  does not produce a non-unique solution.

The interpolating function is guaranteed to lead to interpolated values inside the perimeter of four points which lie between the maximum and minimum values of the specified values because harmonic functions attain their extremum only on the peripheral region. Some care is needed to handle special cases when some of the divisors may become zero, but the effort required is no more than a reordering of the equations. The second-order terms will vanish if two of the four points become coincident because the information available will be insufficient to allow such representation. Colinearity of all the points will again degenerate the scheme by lowering the dimensionality of the original problem. In practice, however, the integrity of the scheme has been found to remain intact for a set of four points at the corners of a rectangle with an aspect ratio of 10,000.

The availability of an analytical potential distribution throughout the network of four points on a body surface greatly facilitates the flow analysis procedure. Tangential velocity components are simply the derivatives of  $\phi$  in terms of  $x$  and  $y$ . While the function is differentiable everywhere, the accuracy of the calculated derivatives deteriorates as the sides of prescribed points are approached. This is to be expected because along the sides the prescribed values do not contain sufficient information to form the derivative normal to the sides. It is, therefore, best to form the derivatives near the centroid of the four points and perform a second

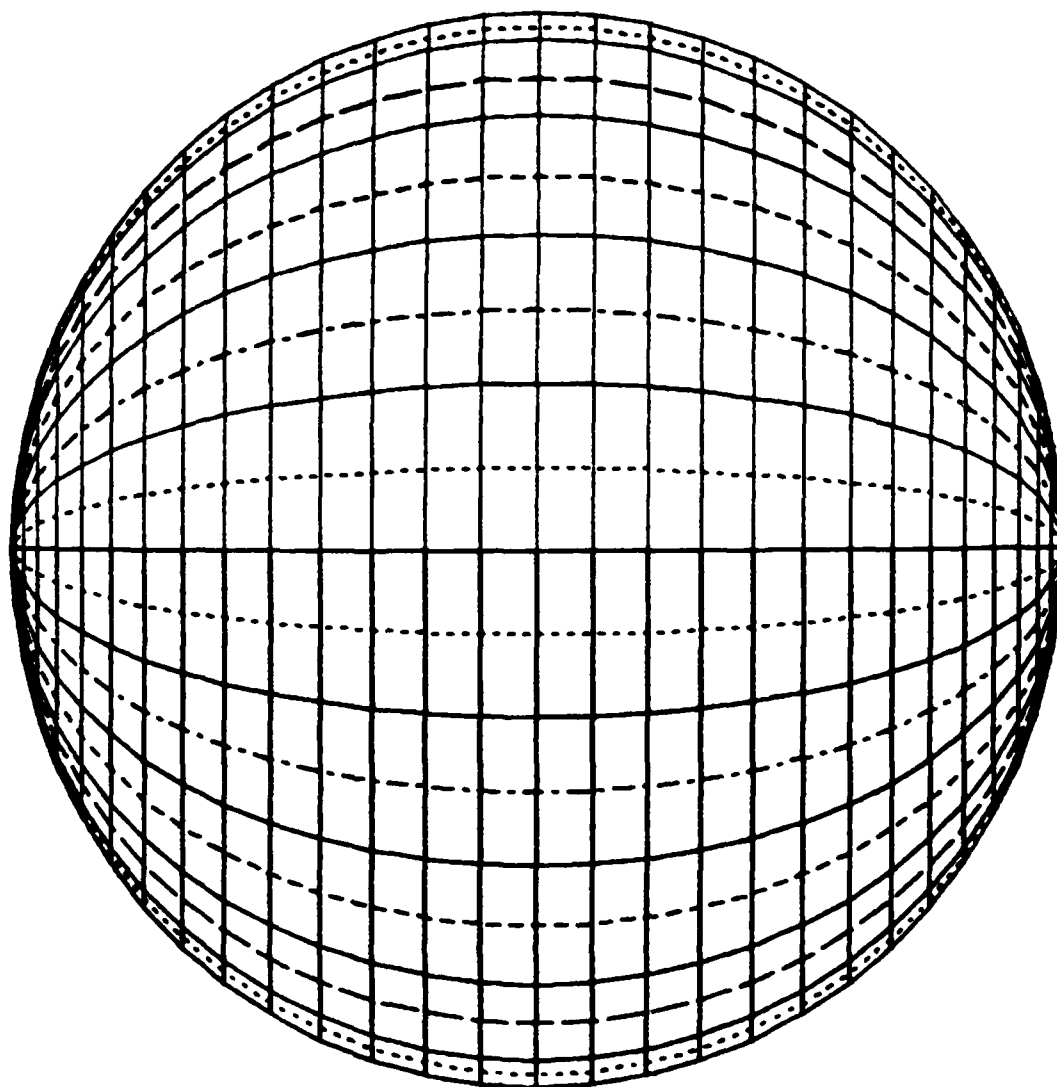
interpolation on the calculated velocity components to evaluate the velocity components everywhere.

To calculate the streamline trajectory through the neighborhood of the four given points it is helpful to form the stream function,  $\psi$ , which follows from the potential distribution of Eqn. (3.2.3). The detailed path of the streamline through the four specified points is given by the following second-order equation, where the coefficients,  $(a)$ , are known from the interpolating function for velocity potential.

$$\psi = a_2x - a_1y - 2a_4xy + a_3(x^2 - y^2)/2 \quad (3.2.11)$$

$$\phi = a_0 + a_1x + a_2y + a_3xy + a_4(x^2 - y^2) \quad (3.2.12)$$

Two examples of calculated streamlines are presented here. Figures 3.2.2 and 3.2.3 show the equatorial and polar views of streamlines on a sphere, respectively, while the pressure distribution along the streamlines is plotted against the exact solution in Figure 3.2.4. Streamlines calculated on a swept wing configuration (sweep  $30^\circ$ ) are presented in Figures 3.2.5 through 3.2.7 for an angle of attack of  $16^\circ$ . Streamlines were calculated close to the plane of symmetry and the tip region to demonstrate their behavior near the plane of symmetry and curved surfaces.



SPHERE WITHOUT WAKE

XVUE = 0.00

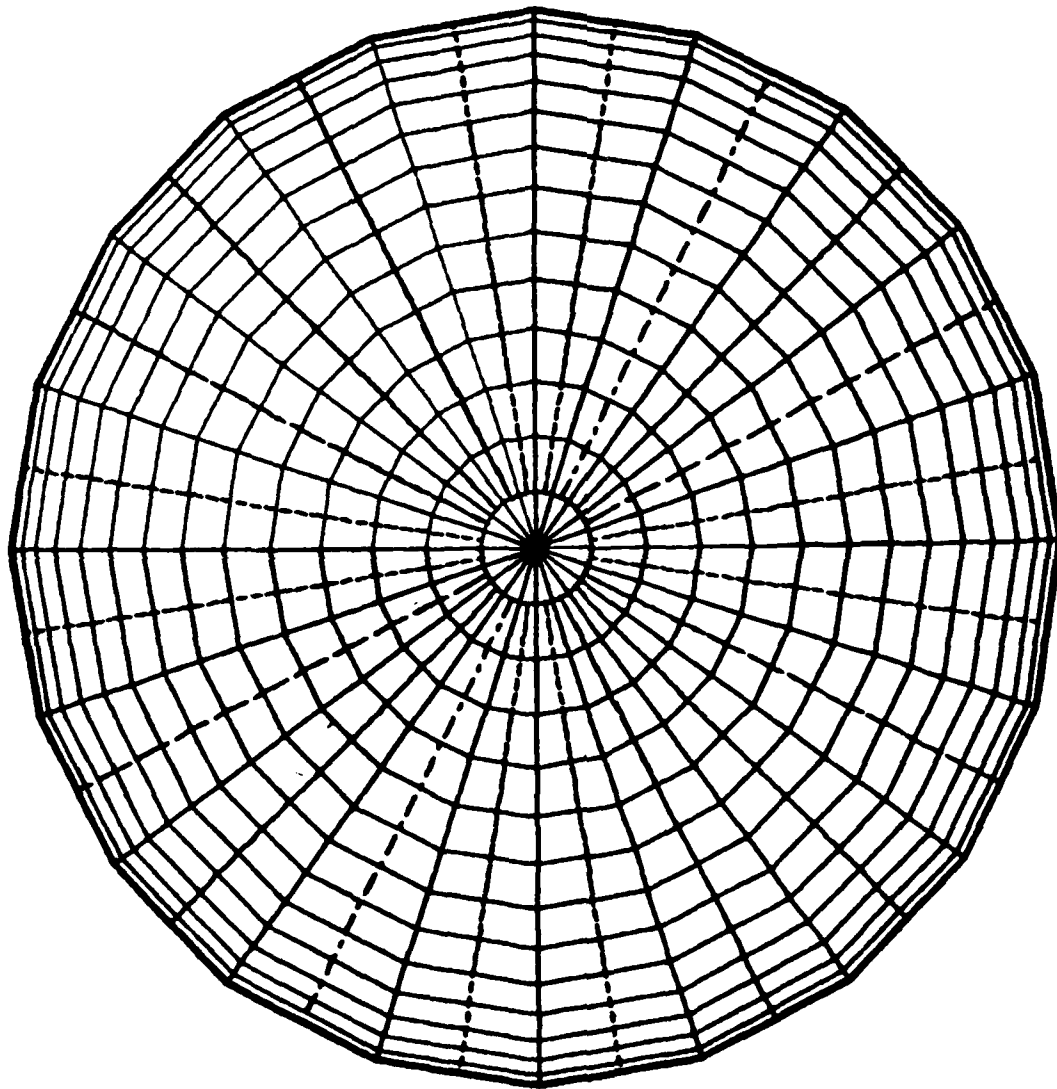
YVUE = 0.00

ZVUE = 14.00E+06

ITER = 1

03-20-64

Figure 3.2.2. Sphere Streamlines, Equatorial View.



SPHERE WITHOUT WAKE

XVUE = 14.00E+06

YVUE = 0.00

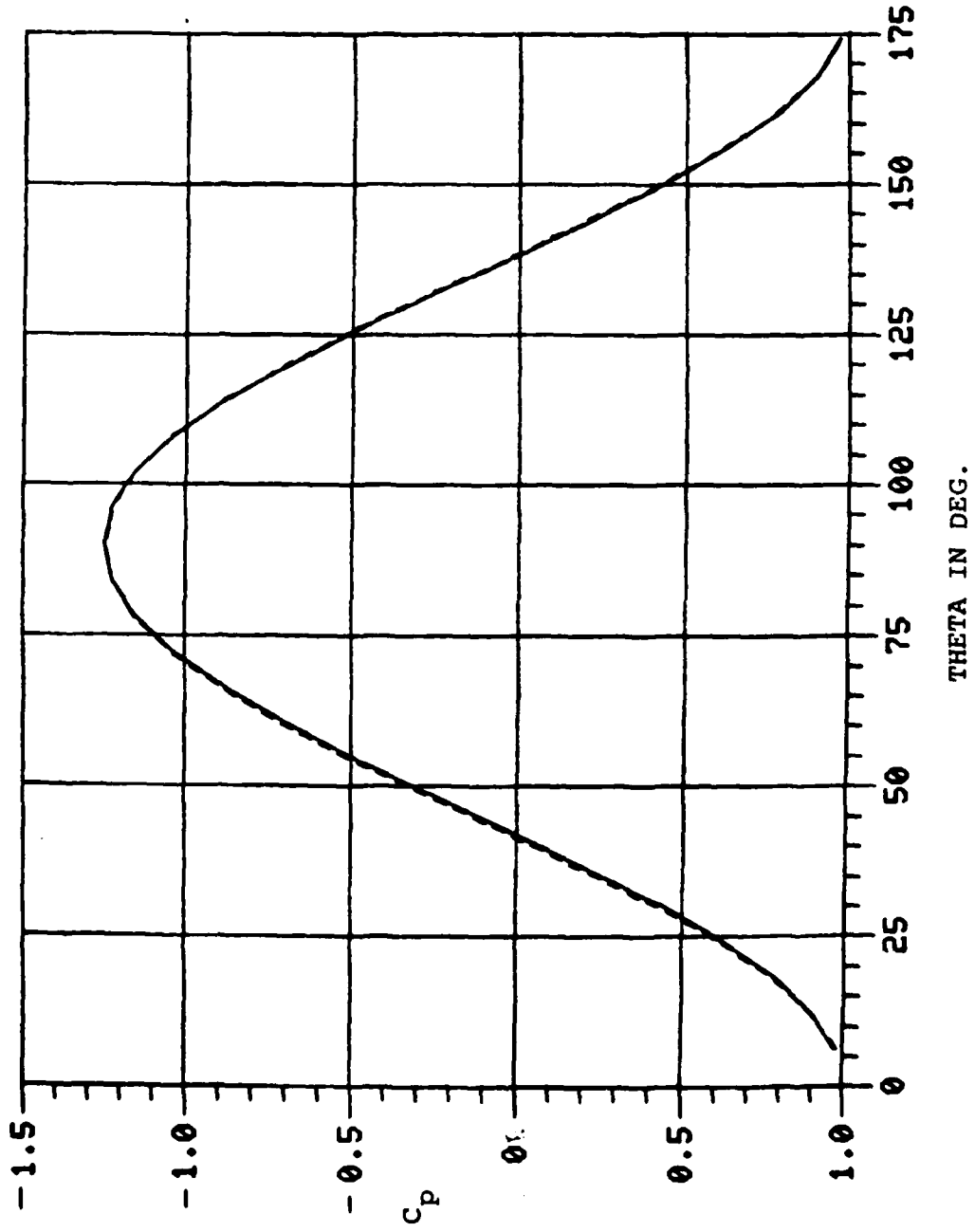
ZVUE = 0.00

ITER = 1

03-21-84

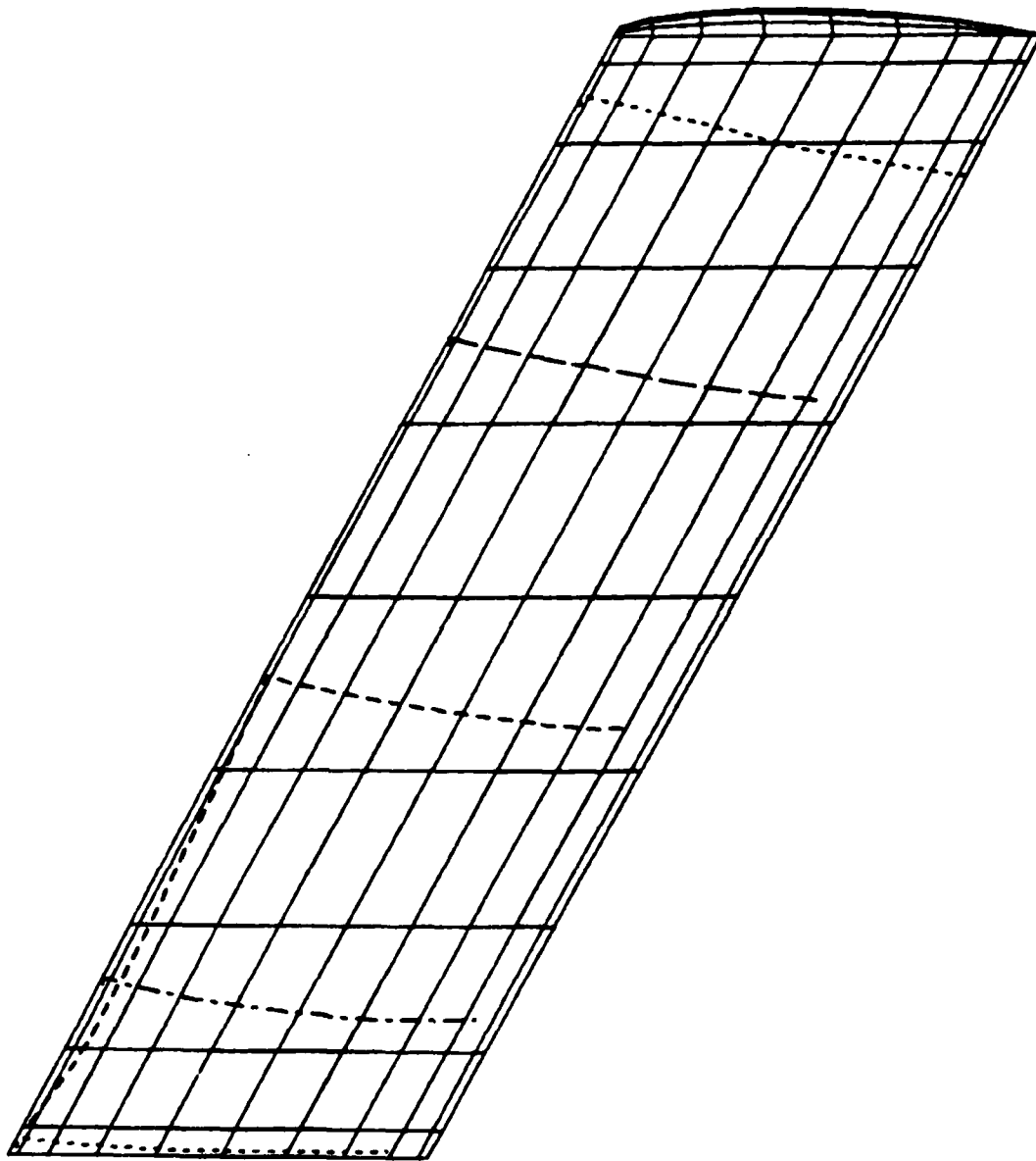
Figure 3.2.3. Sphere Streamlines; Polar View.

— EXACT SOLUTION  
- - - - - CALCULATION



THETA IN DEG.

Figure 3.2.4. Calculated Pressure on Streamlines Compared against Exact Solution.



NLRUING WITH RELAXED WAKE

XVUE = 0.00

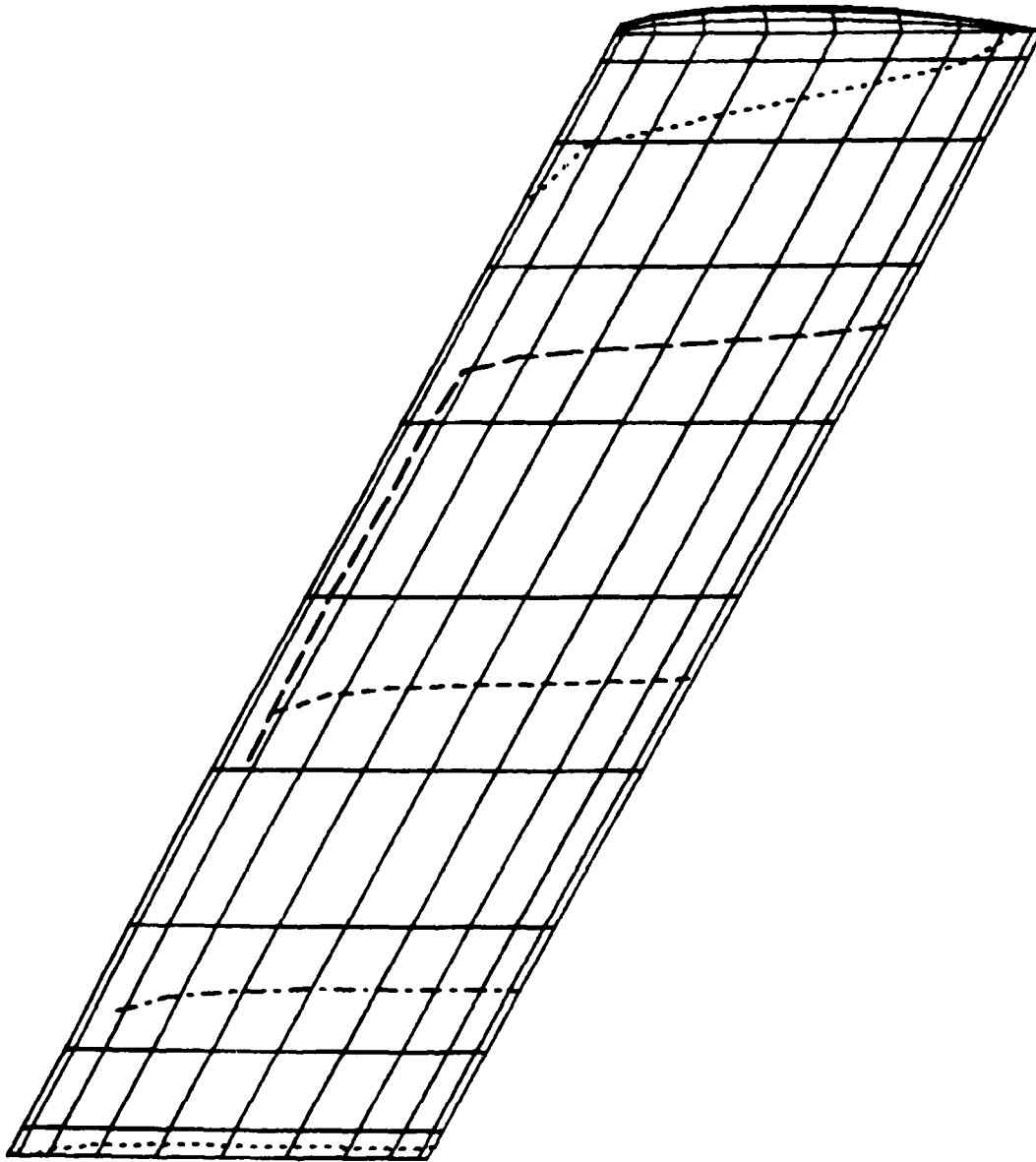
YVUE =

0.00

ZVUE = 14.00E+06

ITER: 4  
63-28-84

Figure 3.2.5. Streamlines on Upper Surface of Wing; Angle of Attack 16°.



NLRUING WITH RELAXED WAKE

XVUE = 0.00

YVUE = 0.00

ZVUE = 0.00

ZVUE = 14.00E+06

ITER: 4  
03-28-84

Figure 3.2.6. Streamlines on Lower Surface of Wing; Angle of Attack 16°.

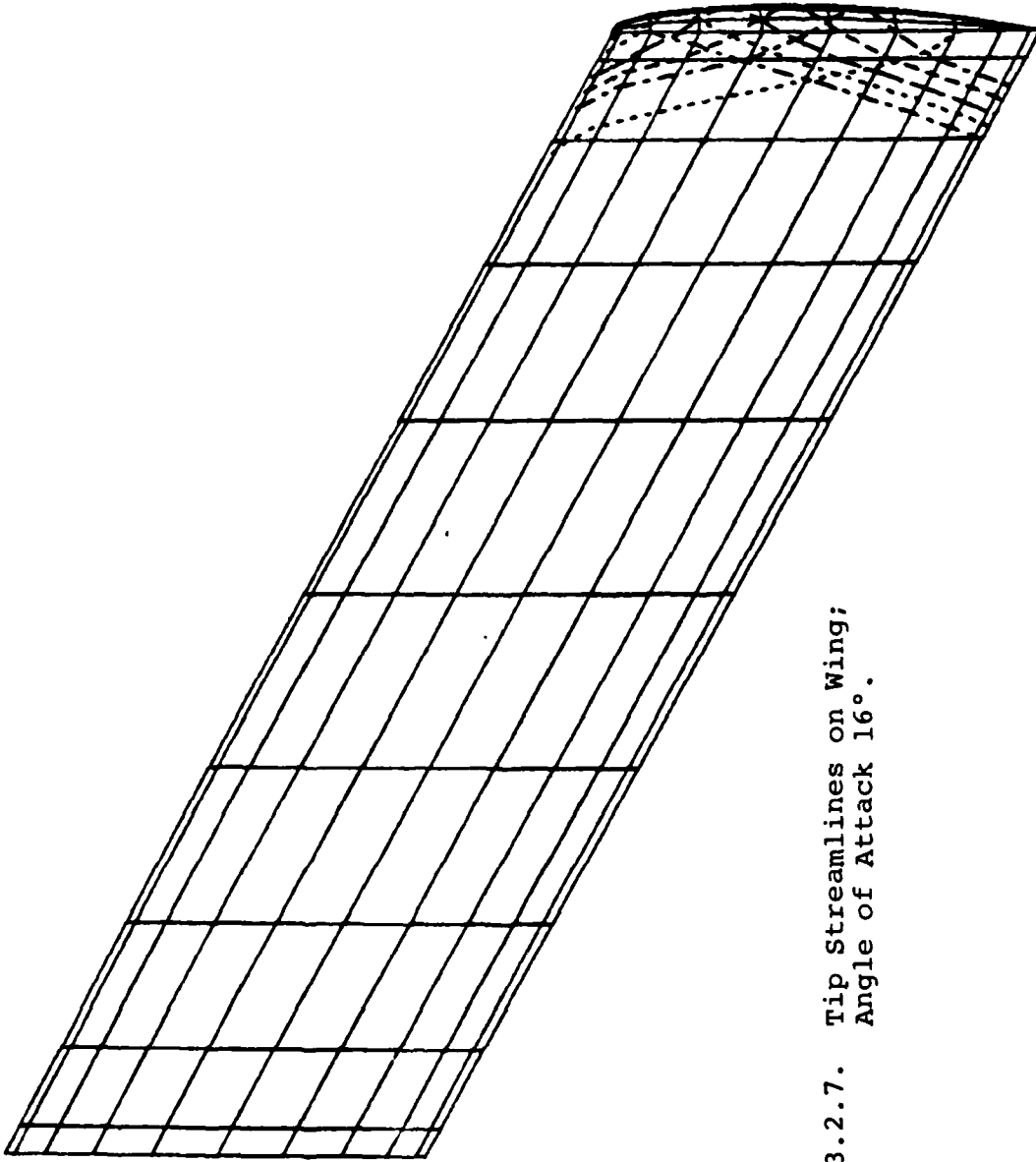


Figure 3.2.7. Tip Streamlines on Wing;  
Angle of Attack 16°.

NLRWING WITH RELAXED WAKE

XVUE= 0.00

YVUE=

0.00

ZVUE= 14.00E+06

ITER: 4  
03-28-84

### 3.3 Boundary Layer Methods

Currently two independent boundary layer methods are available in VSAERO. The first is a streamline approach based on the small cross-flow assumption with streamline convergence/divergence effects included. The second is an infinite swept wing approach which can be made fully three-dimensional via iteration.

In the streamline method the laminar calculation is based on Curle's method (36). Once transition or laminar separation is detected (by a modified Granville approach), or boundary layer tripping is prescribed, the turbulent boundary layer development is determined by a modified Nash and Hicks method (37). Separation on a given streamline is predicted when the local skin friction coefficient reaches zero. The locus of separation points on a series of streamlines forms the three-dimensional separation line.

The three-dimensional wing is developed into a number of streamwise strips. Three-dimensional velocities are used to calculate individual streamlines over each of the strips, each streamline beginning at the stagnation line. Streamline curvature and divergence (convergence) distributions along the streamlines are computed directly from the three-dimensional velocity component and streamline information. Integral methods are used to calculate the boundary layer development along the streamlines. Calculations are begun at the stagnation line using initial conditions based on a combined theoretical and experimental study. Theoretical predictions of the stagnation line flow of an infinite yawed wing by Cumpsty and Head (38) and Bradshaw (39) as well as others indicate that the boundary layer approaches an asymptotic state where frictional forces are balanced by divergence of the flow from the spanwise to the streamline direction. Cumpsty and Head found that the stagnation line boundary layer integral parameters ( $H$ ,  $\theta$ , and  $C_f$ ) and the state (laminar or turbulent) correlate with the parameter,  $C^* = V^2/(\nu(dU/ds))$ . Cumpsty and Head (40) later experimentally verified their theoretical correlations, and it is these correlations that are used to determine the initial boundary layer characteristics on each strip of the swept finite wing. If the wing is unswept, then conventional two-dimensional correlations are used to start the boundary layer calculations. Recently, McLean (41) has shown that at least for a high aspect ratio wing, in this case specifically the BAC 727-200 wing, a fully three-dimensional calculation and an infinite span calculation procedure gave identical results for the attachment (stagnation) line flow. This result, of course, cannot be generalized to the full wing case, and it is expected that in the wing root or tip regions or wherever one has close vortex/surface interactions, a full

three-dimensional calculation should probably be utilized. Unfortunately, the full three-dimensional approach such as McLean's is very expensive of computer time. For example, as quoted by McLean, using this coarsest grid network, each surface of the 727-200 wing required 10 minutes of CDC 6600 CPU time. In comparison, an integral approach would require approximately 30 seconds of CPU time. Assuming that 4 to 5 iterations are required to achieve a converged viscous/inviscid solution for a wing with separated flow, computation times for the overall calculation become prohibitive. It should be noted at this stage that while the boundary layer method (Cumpsty and Head (42)) is formulated assuming infinite span, the use of the actual three-dimensional velocity components, streamline paths, streamline curvature and streamline divergence (convergence) make the approach quasi-three-dimensional in nature.

### 3.4 Estimation of Leading-edge Vortex Geometry

#### 3.4.1 Introduction

Flow separations are certain to occur on highly swept wings at moderate to high angles of attack. The separations usually produce free vortex layers, joined to the leading edges of the wing, which roll up to form spiral-shaped vortex sheets above the surface, a classical illustration being the vortices over delta wings. These separations lead to important non-linear lift characteristics because both the position and strength of the vortex sheets vary with angle of attack.

The aerodynamic analysis of aircraft with leading-edge vortices is best handled by panel methods such as VSAERO (32) or the Free Vortex Sheet computer code (27). These programs use an iterative procedure to determine the position of the vortex sheets. If the initial structure of the leading-edge vortices is unrealistic, a great deal of computational effort is required for a solution. Indeed, a poor initial structure can lead to an unstable iteration and no solution. A starting solution preprocessor that would decrease the labor involved in generating an initial structure and reduce the iterations necessary for convergence would produce significant cost savings.

Analytical Methods, Inc. has developed such a wake preprocessor for VSAERO. This preprocessor, VORSEP (28), (43), needs very little additional input above that required for VSAERO, and, for less computation effort than one wake iteration, produces an excellent starting solution for the three-dimensional code. In addition, VORSEP is applicable to very general configurations.

### 3.4.2 Theory

VORSEP is an unsteady potential flow code accurate for two-dimensional bodies with separation. It is also applicable to steady, three-dimensional, separated flow under the unsteady cross-flow analogy. In this analogy, Figure 3.4.1, the fluid motion in a plane perpendicular to the x-axis is assumed to be two-dimensional. Variations from one cross-flow plane to the next proceed as if the x-coordinate were time-like in nature. This two-dimensional cross-flow assumption is commonly used for the roll-up of vortices behind a wing (44), (45). In the case of attached flow, the theory has been used by Munk (46) and Tsien (47) for the lift of an elongated body of revolution and by Jones (48) for the flow around low aspect ratio wings. VORSEP, under this contract, has been adapted to handle all three cases, a wake without a body, a body without a wake, and bodies with separation.

A complete description of the panel method is presented in (29). Only a brief outline of the panel boundary condition equation is presented here.

The panel method in the VORSEP code is based on doublet and source singularities distributed on flat panels representing the section surface. The doublet distribution is continued onto the free sheet. At each time step the boundary condition of zero total velocity potential is applied on the inside of the section at a control point (mid) on each panel. With this formulation the total tangential velocity on the exterior (wetted) surface is the doublet gradient and the source value there is proportional to  $(1/2\pi)$ , the total normal velocity. In the present case the source distribution represents the normal component of the "growth" rate, and since the latter is just a function of the geometry, the source distribution can be evaluated at each section. The boundary condition equation, therefore, has the following form:

$$\sum_{k=1}^N A_{jk} \mu_k / 2\pi + F_j = 0$$

where

N is the number of surface panels;

$A_{jk}$  is the potential influence coefficient on the j<sup>th</sup> control point due to unit doublet distribution on the k<sup>th</sup> panel. (Note: for the panel acting on its own control point,  $A_{jj} = -\pi$ );

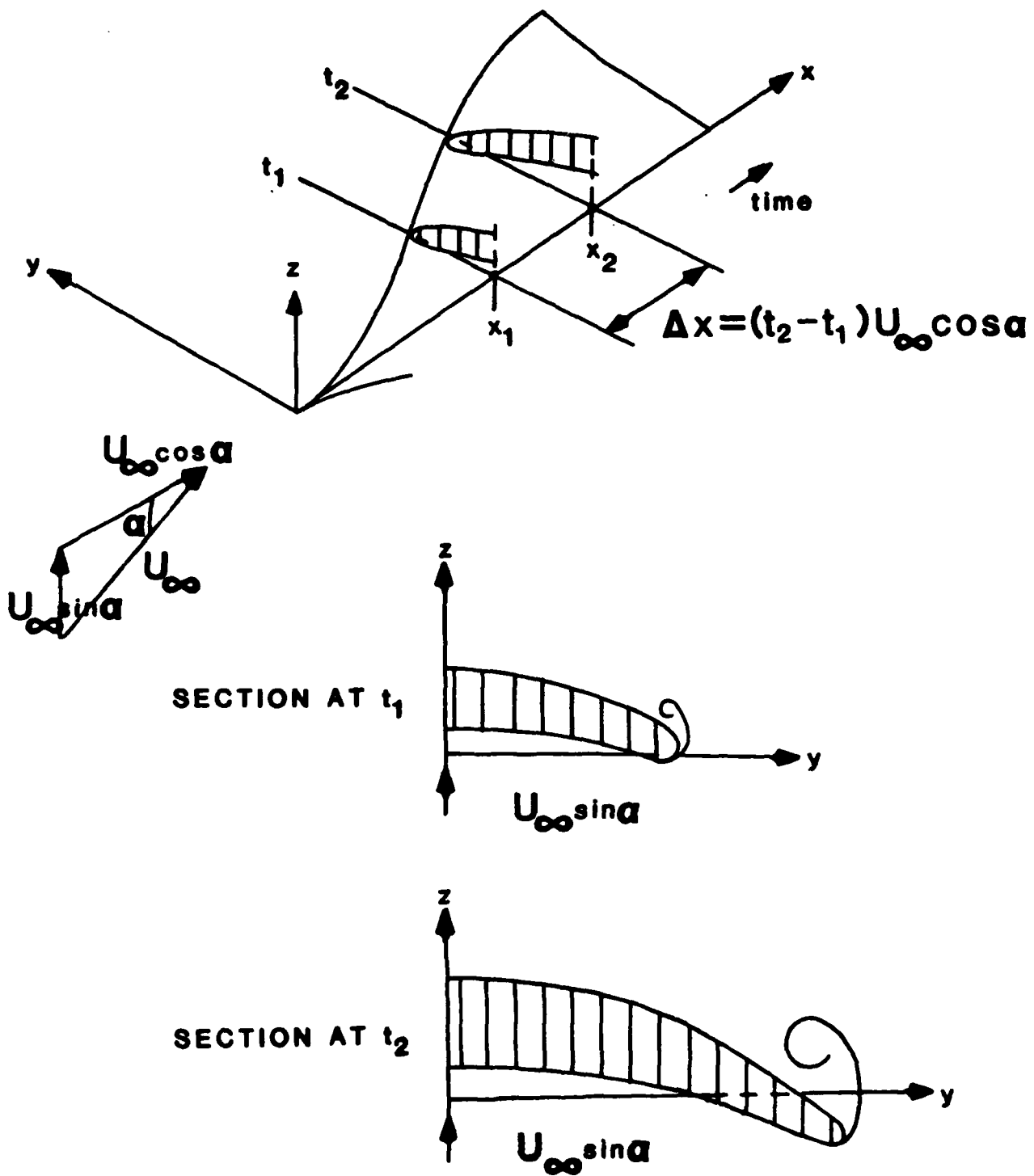


Figure 3.4.1. Unsteady Cross-flow Analogy.

$\mu_k$  is the surface panel ( $k^{\text{th}}$ ) doublet value (unknown); and

$$F_j = \phi_{\infty j} + \sum_{k=1}^M A_{jk} \mu_{wk}/2\pi + \sum_{k=1}^N B_{jk} \sigma_k/2\pi$$

where

$\phi_{\infty j}$  is the onset flow potential at the  $j^{\text{th}}$  control point;

$M$  is the number of free-sheet panels at this time step;

$\mu_{wk}$  is the free-sheet panel ( $k^{\text{th}}$ ) doublet value (known);

$B_{jk}$  is the potential influence coefficient on the  $j^{\text{th}}$  control point due to a unit source distribution on the  $k^{\text{th}}$  panel; and

$\sigma_k$  is the surface panel ( $k^{\text{th}}$ ) source value.

### 3.4.3 Wake Model

The choice of a wake model for computing the roll-up of a vortex sheet has three objectives. One is to neutralize the inherent instability often encountered by an arbitrary, infinitely thin shear layer (see Moore (49)). This mathematical instability produces a chaotic motion regardless of the detail of the wake structure. Judicious modifications to the model, such as minimum vortex spacing (or panel size for higher-order methods (50)), and viscous core vortices (51) can dampen the instability to an acceptable level. The second objective is to suppress small-scale structures that have no significant effect on the flow but require extensive computational effort. An example of this is the modeling of the core of a wing tip vortex. The infinite-spiral vortex sheet can be modelled to the limit allowed by the particular computer but a point is very quickly reached where viscous effects dominate in the real flow, making the idealized structure only of academic interest. Vortex amalgamation is a well known technique for eliminating small-scale structures. The final reason for selecting a wake model is economy. This is especially impor-

tant to VORSEP, which is intended to be a less expensive means of calculating a wake shape than three-dimensional wake relaxation in VSAERO. Some accuracy can be sacrificed for economy because the accuracy of the two-dimensional calculation is a moot question once the shape has been changed by VSAERO, and because wake roll-up, especially over a solid surface, is a three-dimensional process that can only be approximated by unsteady, two-dimensional calculations.

The fact that VORSEP is linked to VSAERO also bears on the first two points. Whether a wake model is ultimately unstable may be of little consequence to VORSEP if the instability affects only the wake structure far from the body. This determines what is an acceptable level for the instability. The three-dimensional model used in VSAERO is also limited in the amount of detail which can be included in the body and wake geometry, a limit that is far below the specifics VORSEP can generate. Therefore, it makes little sense for VORSEP to faithfully model the spiral shape of a wake produced by a strake or snag and then replace that spiral with a single vortex in the three-dimensional model.

The wake model developed for VORSEP is quite similar to that in the Free Vortex Sheet computer code. As seen in Figure 3.4.2, it consists of a free vortex sheet, modelled by doublet panels, and a vortex core which is an amalgamation of all the free vorticity that has passed a user-controlled merge angle. A feeding sheet connects the free vortex sheet and the core. At each time step the free vorticity is distributed at evenly spaced intervals over the free sheet. This redistribution, similar to that of Fink and Soh (45), stabilizes the motion of the wake. As a result, no stability problems have appeared in the time spans necessary to reach the trailing edge. Indeed, calculations have also proceeded beyond the trailing edge of several wings.

The increased circulation shed onto the wake is determined by the condition

$$d\mu_{sep}/dt = \frac{1}{2}\gamma_s^2$$

where  $\gamma_s$  is the surface velocity at the separation point. This follows the work of Clements (52).

Although, at this time, the wake model assumes there is only one core, multiple vortex cores can be modelled if they are in separate wakes. VORSEP has the capacity to include up to four wakes simultaneously. Expansion of the wake model to allow multiple cores is expected soon.

STATION 39.50

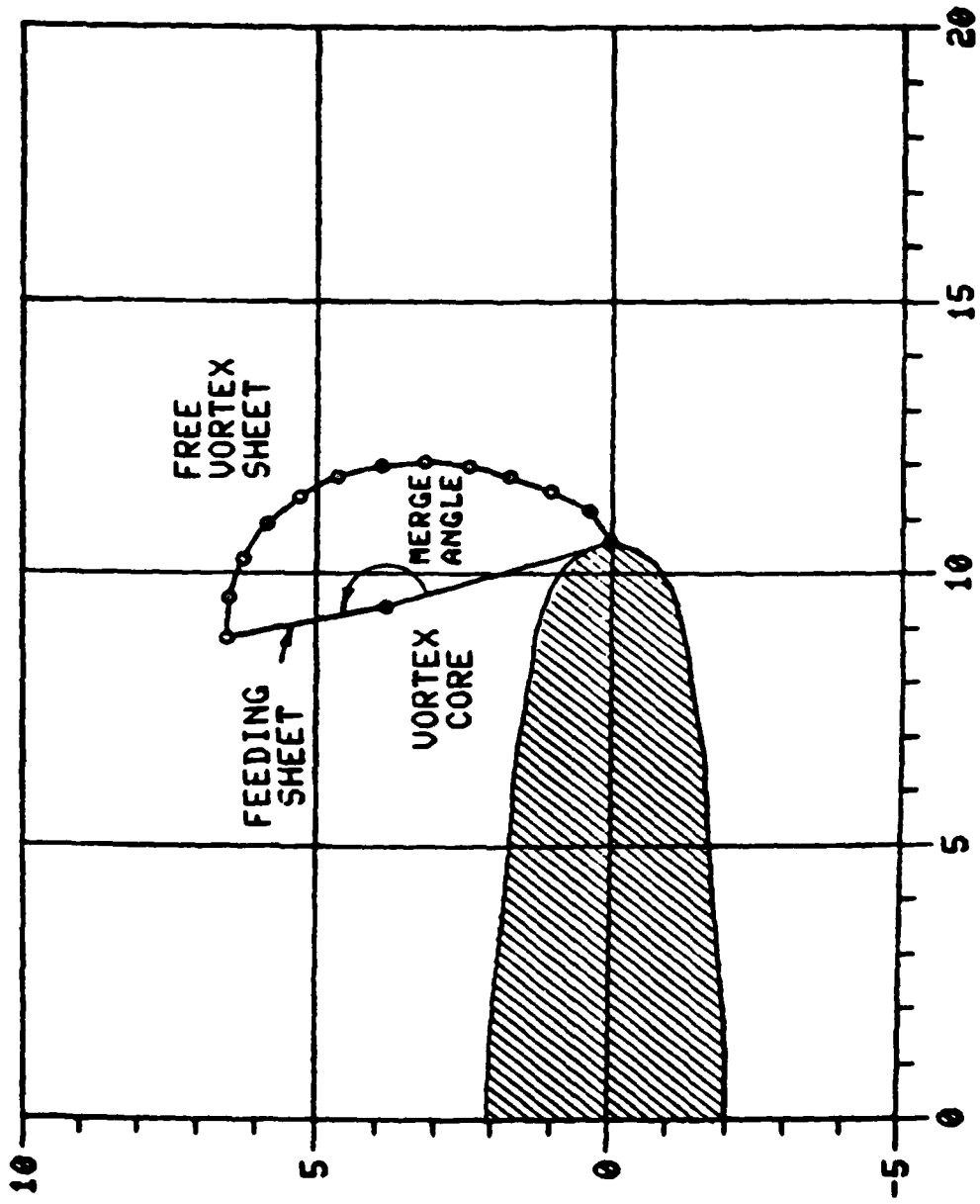


Figure 3.4.2. VORSEP Wake Model.

#### 3.4.4 Streamline Tracker

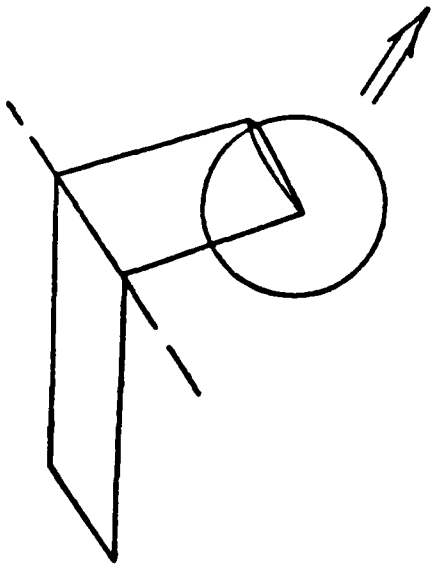
VORSEP redistributes the free vorticity to stabilize the calculation of wake motion. This complements the capability of paneling the body at each time step according to the instantaneous needs required by body and wake geometry. However, the redistribution destroys any connection between an individual vortex (the edge of a wake panel) and the position of a particle attached to the wake. The path of such a particle will be a streamline in the three-dimensional flow; in particular, it is the trajectory of a continuous wake vortex.

To track the trajectory of a streamline, it is conceivable to release imaginary particles from the desired starting points and follow their positions in space. It is preferable to use the velocities at nearby wake vortices instead of calculating the velocities at the particles because velocity calculations are expensive, and, since the particles are dispersed arbitrarily among the wake vortices, their velocities cannot be calculated accurately by direct application of the Biot-Savart law.

A method which avoids expensive velocity calculations and also obviates storing the position of imaginary particles was developed for VORSEP. This method uses the invariance of the doublet strength along a wake streamline to track the streamline trajectory. Referring to Figure 3.4.3, we see the vortex sheet shapes produced by VORSEP at four time steps over the tip of a swept wing. For each vortex sheet we can plot the value of the doublet strength of the sheet against the arc length, starting at the separation point, as in Figure 3.4.4. If the vorticity shed into the wake has always been of the same sign, the doublet strength will decrease monotonically from its value at the separation point to zero at the end of the wake sheet. The doublet strength at the separation point also grows monotonically with each time step.

To find the corresponding positions ( $S_2$ ,  $S_3$ ) at two time steps ( $t_2$ ,  $t_3$ ) on a streamline it is only necessary to find the points with equal doublet strength. This doublet strength is the same at every time step and is the doublet strength at the separation point at the time the particle left the body. To begin tracking a streamline, VORSEP requires only the station at which the streamline originates. When that station is passed, VORSEP interpolates between the time steps which bracket the starting station for the doublet strength at the separation point. This is stored and the corresponding point at each succeeding time step is readily interpolated from the known doublet strength distribution on the wake.

TIP VORTEX ROLL-UP



VORSEP VORTEX GEOMETRY

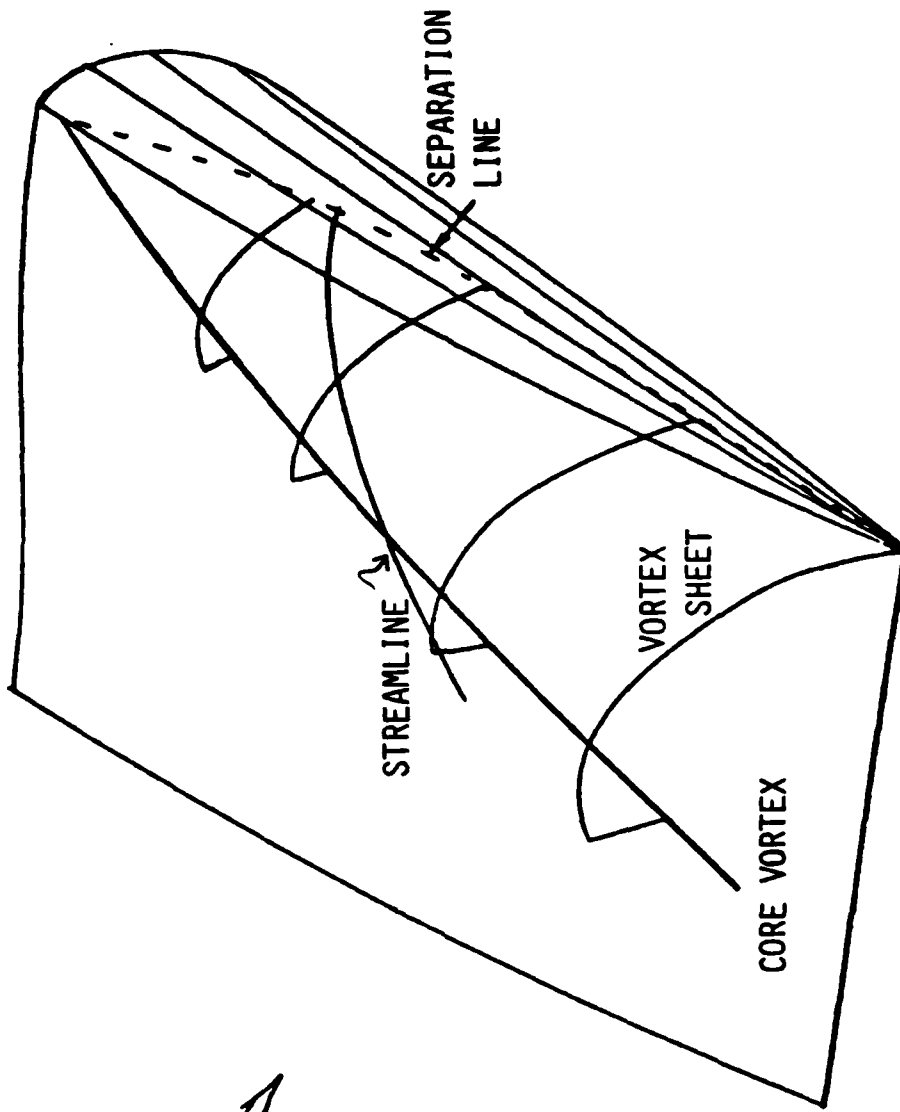


Figure 3.4.3. Streamline and Wake Geometry.

PREDICTION OF STREAMLINES

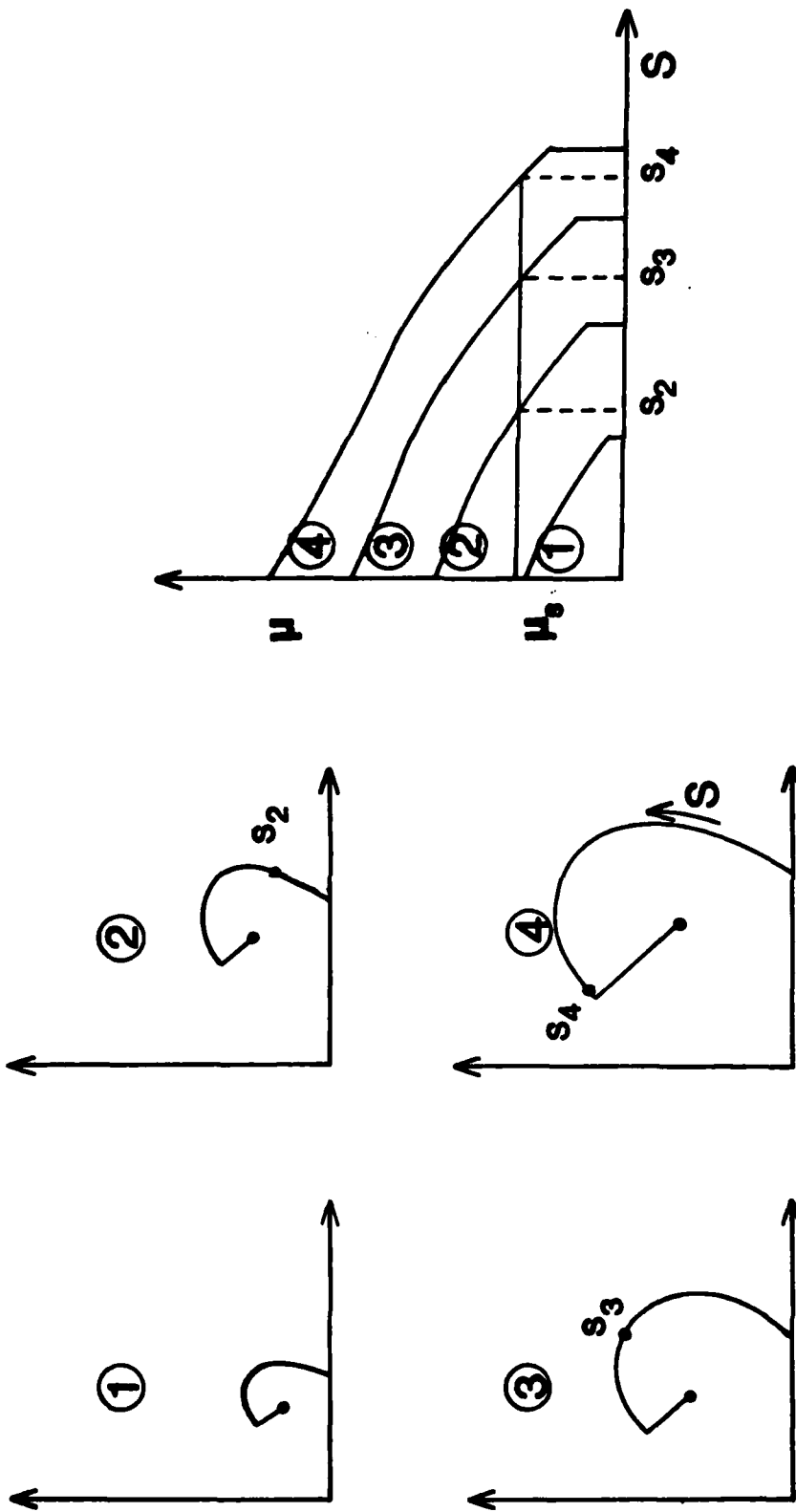


Figure 3.4.4. Prediction of Streamline Trajectory from Wake Doublet Distribution.

The doublet strength does not always vary monotonically along the arc of the wake. In such a case, the position of a particle as a function of the doublet strength becomes multi-valued for some doublet values. This can lead to more than one point from which to choose. The solution to this problem is to remember which wake panel the particle was on in the previous time step and select the point closest to that panel.

For the wakes considered so far, this has proven a reliable and economical means of generating three-dimensional streamline trajectories.

#### 4.0 NUMERICAL PROCEDURE

The coupling of the potential flow method, the surface streamline and boundary layer codes is outlined in Figure 4.1. The first step is to define the surface of the configuration relative to a body-fixed coordinate axis system, Figure 4.2. The x-axis is normally taken downstream with z upwards and y spanwise. The z-x plane is regarded as a plane of symmetry in unyawed flight.

The complete surface of the wing, including the tip-edge surface is represented by a number of flat quadrilateral panels over each of which the doublet and source distributions are assumed constant. The surfaces,  $S_{EW}$ , are also represented by flat quadrilateral panels but with linear doublet distribution in the streamwise direction. The geometry of  $S_{EW}$  is prescribed initially.

Using this model the boundary condition, Eqn. 3.1.8, is satisfied simultaneously at a control point under each of the surface panels on the wing. If there are N panels on the wing, then we have N simultaneous equations in N unknown doublet (i.e., perturbation velocity potential) values.

Following the solution of the surface doublet distribution, the surface perturbation velocity vectors are obtained from the gradient of the potential using a second-order approximation through three panel doublet values in two directions. Forces and moments are obtained by pressure integration. Pressures in the separated zone are corrected for the total pressure jump:

$$C_p = 1 - \left( v_w / v_\infty \right)^2 + \Delta H / q_\infty$$

where  $q_\infty$  is the free-stream dynamic head and H is obtained from Eqn. 3.1.12. This is applied for each spanwise station in the separated zone.

Following a doublet solution, velocities,  $V(s)$ , are computed along wake lines on surface,  $S_{EW}$ , and segments of those lines are aligned with the local flow direction using an Euler-Gauss scheme. When the new wake configuration has been formed, the matrix of influence coefficients is modified and a new doublet solution obtained and so on in the wake shape iteration loop, Figure 4.2.

When the wake shape has converged a set of inviscid surface streamlines (i.e., external to the boundary layer) may be computed (Section 3.2). We can then proceed through the viscous/potential iteration loop. One of two integral

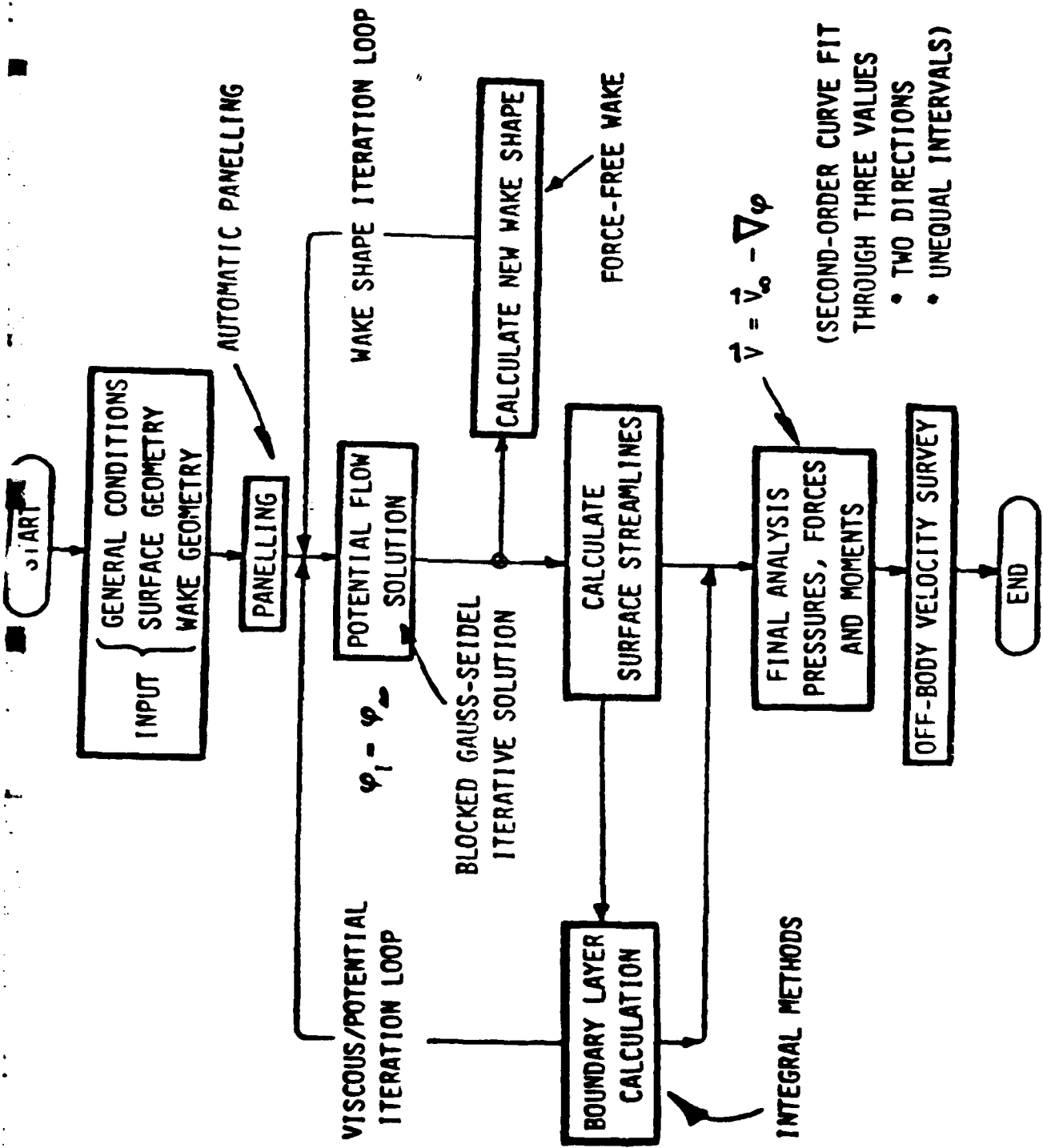


Figure 4.1. VSAERO Method Outline.

SEPARATION LINE  
FROM BOUNDARY LAYER ANALYSIS

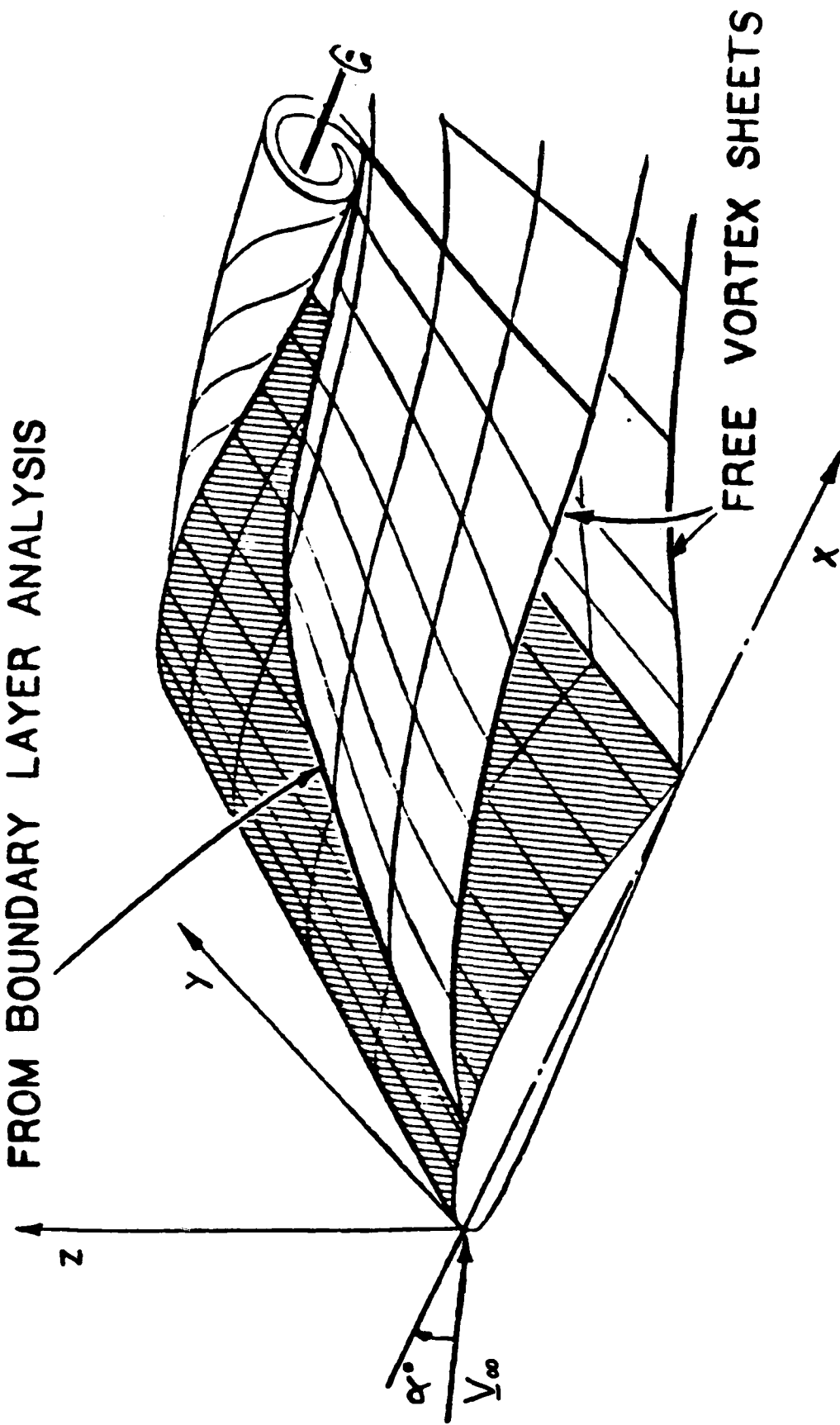


Figure 4.2. General Arrangement of the Configuration.

boundary layer options (Section 3.3) may be used. The infinite swept wing procedure is performed on a column by column basis and does not require the surface streamline calculation. For the streamline boundary layer calculation, an adequate family of surface streamlines must have been calculated. The boundary layer routines return the boundary layer displacement effect and also the location of separation points. The program redistributes the displacement effect terms so that each panel has the term evaluated at its control point. The locus of separation points defines the separation line or lines. For a single separation zone on a simple wing it is feasible to automatically couple a new wake geometry routine to start a new solution in the viscous/inviscid iteration. However, if the separation zone divides into two or more regions from one viscous/potential iteration to the next, then a very sophisticated scheme is required to identify this change and to generate a new multiple wake configuration. Such a scheme has not been attempted. Rather, for this research investigation, the separation points have been examined following a number of viscous/inviscid iterations with fixed separation line. Then the calculations are restarted with a new wake configuration based on the computed separation line. With present day editing facilities and file management on computers, this approach is not unreasonable and is certainly safer for the general case.

Most of the calculations have used approximate separation lines passing along panel edges. For many applications this approach is satisfactory; however, in the general case with strong vortical flow structures, this approach leads to a very rough treatment of the separation line. An arbitrary geometry separation line procedure has, therefore, been developed which has as input a string of separation points approximately lying on the surface of the wing. The program follows this string identifying separation panels and setting the local wake shedding parameters. The string of separation points can be taken directly from the boundary layer routine output, provided those calculations have followed a logical sequence.

When the iterative loops have been completed the final analysis is performed for surface pressures and integrated force and moment. Finally, off-body velocity surveys may be performed to generate details of the flow field including the separated flow region, W, Figure 4.1.

## 5.0 CALCULATIONS

### 5.1 Basic Test Cases

The method was applied to a number of basic test cases for the purpose of testing the coupling of the various routines and for validating the calculation procedure up to the onset of separation. Results from three of these cases are discussed below.

#### Swept Wing

Figure 5.1.1 shows the chordwise pressure distribution at  $\eta = 0.549$  on a thin swept wing at  $5^\circ$  incidence. The wing had a mid-chord sweep of  $30^\circ$ , aspect ratio 6, taper ratio 1/3, and a NACA 0012 section. The datum solution (53) for the case is by Roberts' third-order method using a 39 (chordwise) by 13 (spanwise) set of panels. The present calculations were run using 10 spanwise and 80 and 20 chordwise panels on a "cosine" spacing, giving increased panel density towards leading and trailing edges. Roberts' datum paneling is heavily weighted towards the leading edge; there are, in fact, four panels ahead of the most forward panels in the 80 cosine spacing case.

It is interesting to observe that where the control point density is the same, the low- and high-order solutions are essentially the same. The present calculations using 20 panels deviate from the datum solution near the leading and trailing edges where the control point densities are different. Good agreement is restored in those regions by the 80-panel case, which, at the trailing edge at least, has a similar panel density to the datum case. (Note: Not all the 80-panel pressure values are plotted in the central region of the chord.)

#### Wing with Strake

The fact that surface velocities are obtained by numerical differentiation in the present method might lead to inaccuracies in awkward situations. One situation that could be difficult and which has caused a problem for other methods is the evaluation of the spanwise velocity component,  $V_y$ , in the neighborhood of the kink on a wing with strake. In the case considered in (53), the leading-edge kink occurs at 25% of the semispan and the leading-edge sweep is  $75^\circ$  inboard and  $35^\circ$  outboard. The trailing-edge sweep is  $9^\circ$ . Again the wing section is a NACA 0002 and incidence is  $5^\circ$ .

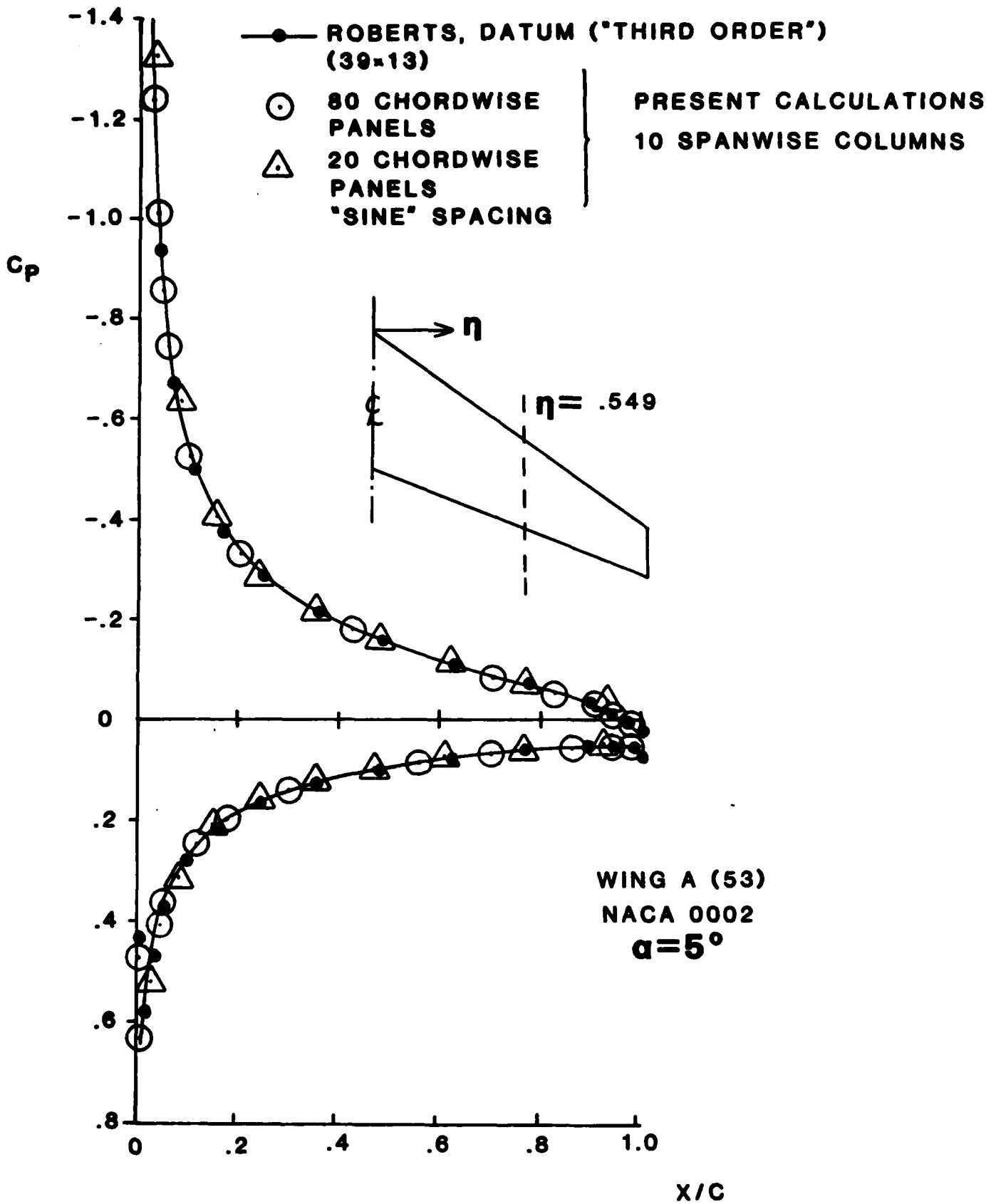


Figure 5.1.1. Comparison of Calculated Chordwise Pressure Distributions on a Thin Swept Wing.

The chordwise distribution of  $V_y$  is plotted in Figure 5.1.2 at stations  $\eta = 0.219$  and  $0.280$ ; i.e., just inboard and just outboard of the kink, respectively.

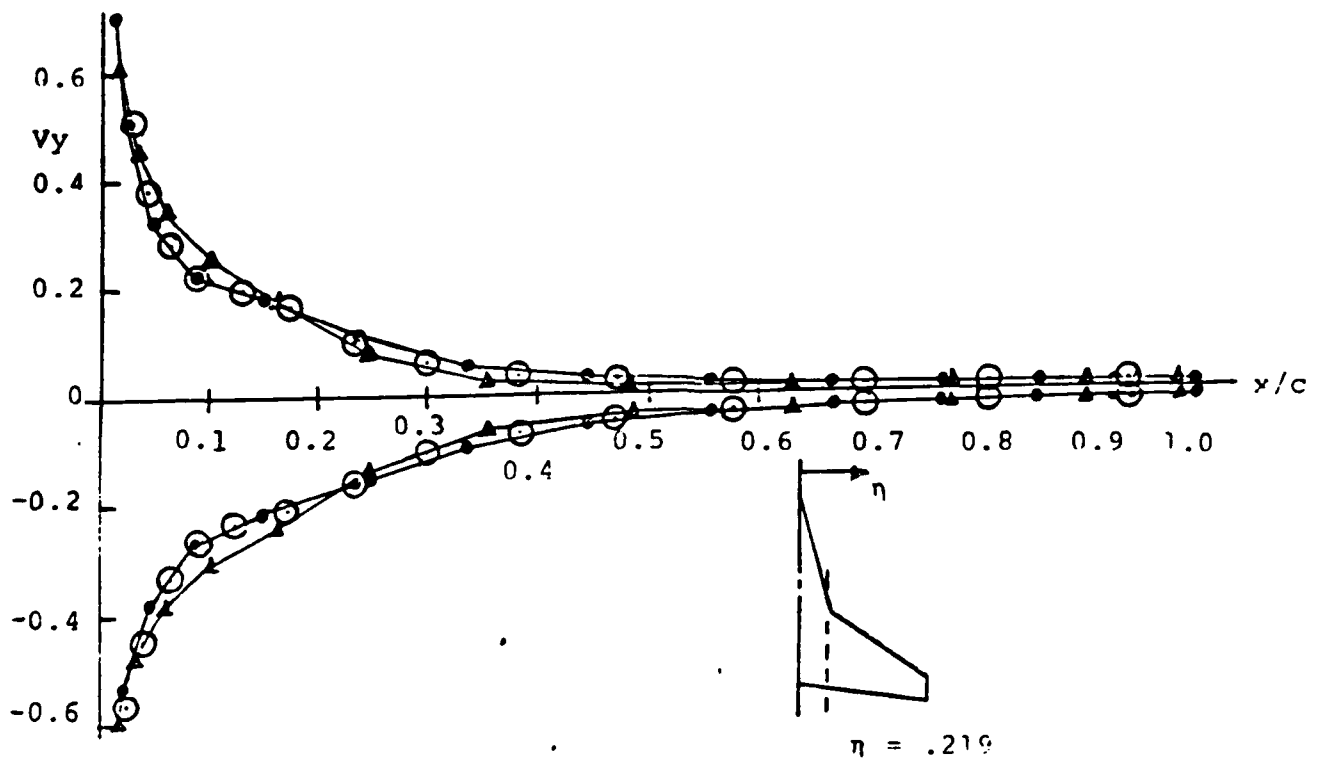
Two higher-order datum solutions are plotted (53) from Roberts' third-order method and from Johnson and Rubbert's second-order method. These datum solutions agree on the outboard distribution but disagree by a small amount on the inboard cut. The disagreement might be caused by the different ways the interpolation is set up across the kink; i.e., this could be a case of the higher-order assumption "flavoring" the solution.

The present calculations are in close agreement with the datum solutions and favor the second-order solution near the leading part of the inboard cut. The case was run as part of a "shakedown" exercise of the code and used 946 panels in a 44 (chordwise) by 20 (spanwise) array with 66 panels on the tip-edge surface. The chordwise paneling was on a "sine" distribution with density increasing towards the leading edge. Such a high number of panels was probably not needed for this case, but the calculation took less than 10 minutes on a CDC Cyber 175 (approximately 2.5 minutes on a CDC 7600).

The third case involves a complete pass through the viscous/inviscid iteration loop. The wing tested by Kolbe and Boltz (54) is examined at  $\alpha = 8^\circ$  and a Reynolds number of  $4 \times 10^6$ . The wing has 45 leading-edge sweep, aspect ratio 3 and taper ratio 0.5. Figure 5.1.3 shows very good agreement between the calculated and experimental spanwise lift distribution. The initial inviscid solution is also plotted for comparison. The viscous solution is after the second iteration. Details of the corresponding chordwise pressure distributions are shown in Figure 5.1.4 at three spanwise stations. Again, the agreement between the calculated and experimental distribution is very close.

## 5.2 Separated Flow Cases

The next series of test cases involves conditions with separation. The first of these cases investigated the calculation of separation boundaries on a rectangular wing of aspect ratio 4. The wing section is NACA 0012. Angles of attack of  $4^\circ$ ,  $8^\circ$ ,  $12^\circ$  and  $16^\circ$  were analyzed. In each case, a family of surface streamlines (e.g., as shown in Figure 5.2.1) was calculated. Separation points calculated by the boundary layer routine were then superimposed on the calculated streamlines to indicate the locus of separation. Figure 5.2.2 shows the extent of tip-edge separation as a function of angle of attack and two Reynolds numbers. The results represent the



—▲—	ROBERTS	} HIGHER-ORDER DATUM SOLUTIONS (53)
—●—	RUBBERT	
○	PRESENT CALCULATIONS PIECEWISE CONSTANT SINGULARITY PANELS	

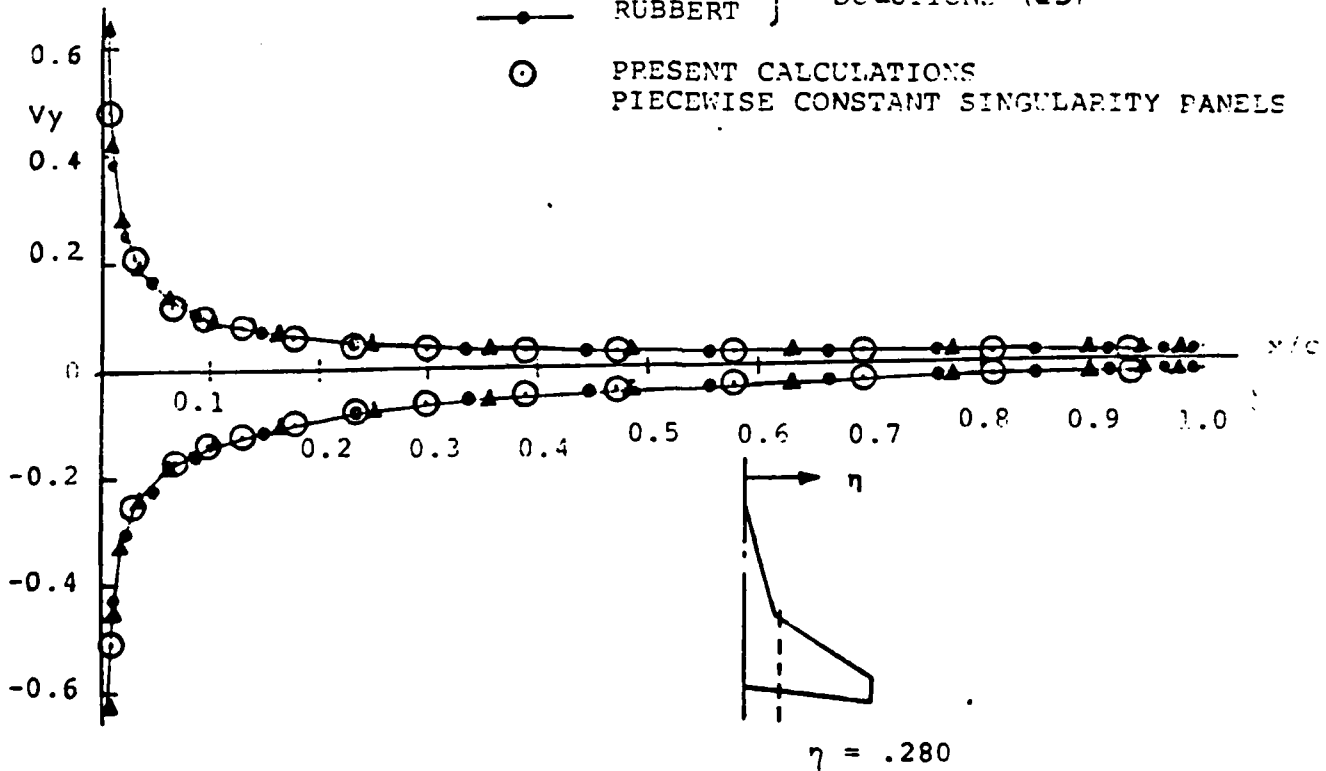


Figure 5.1.2. Comparison of Calculated y Component of Velocity at Two Stations on a Wing with Strake. NACA 0012 Section;  $\alpha = 5^\circ$ .

WING: SWEEPBACK 45°  
ASPECT RATIO 3  
TAPER RATIO .5

$R_e = 4 \times 10^6$   
 $\alpha = 8^\circ$   
 $M = .25$

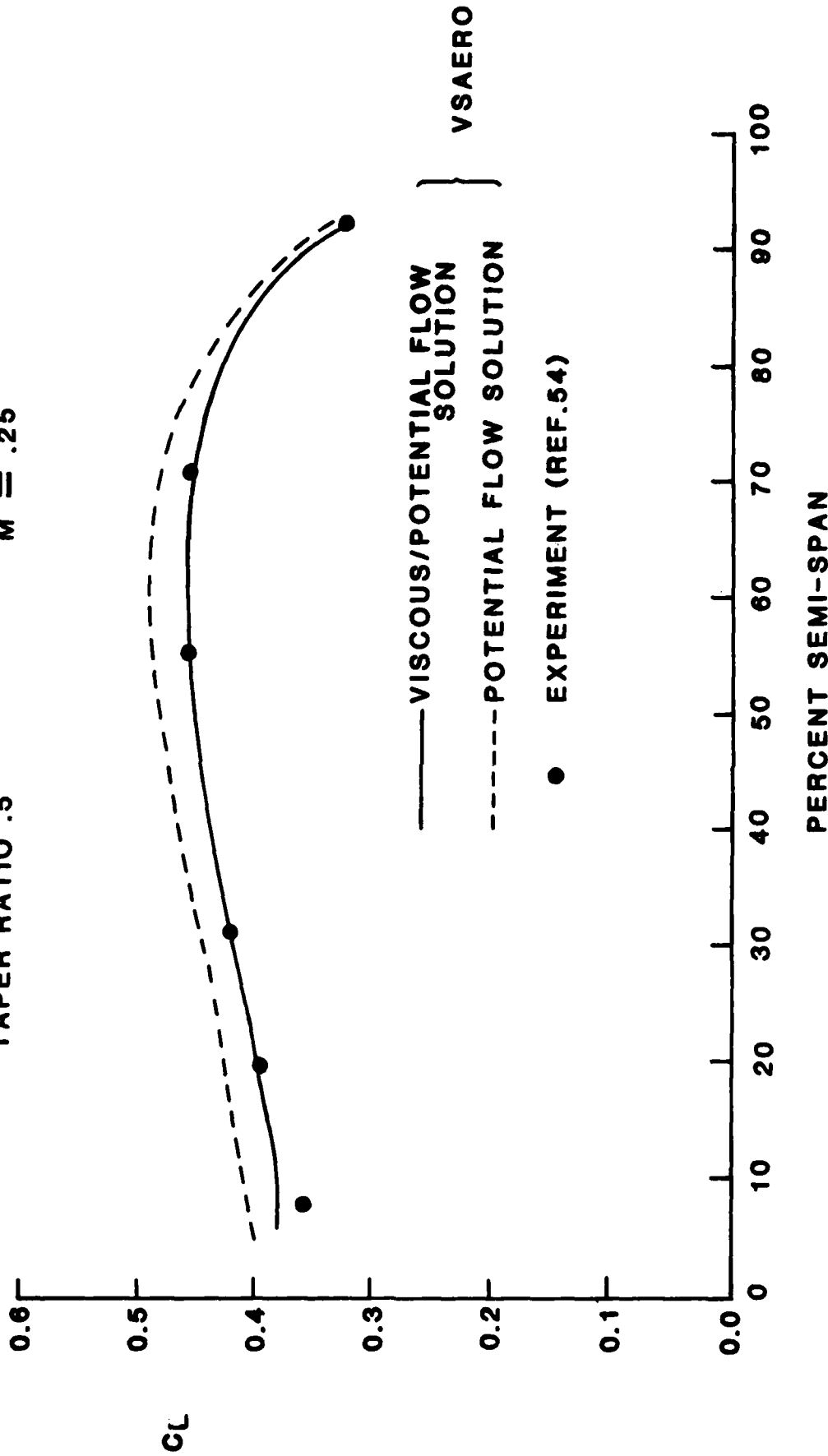
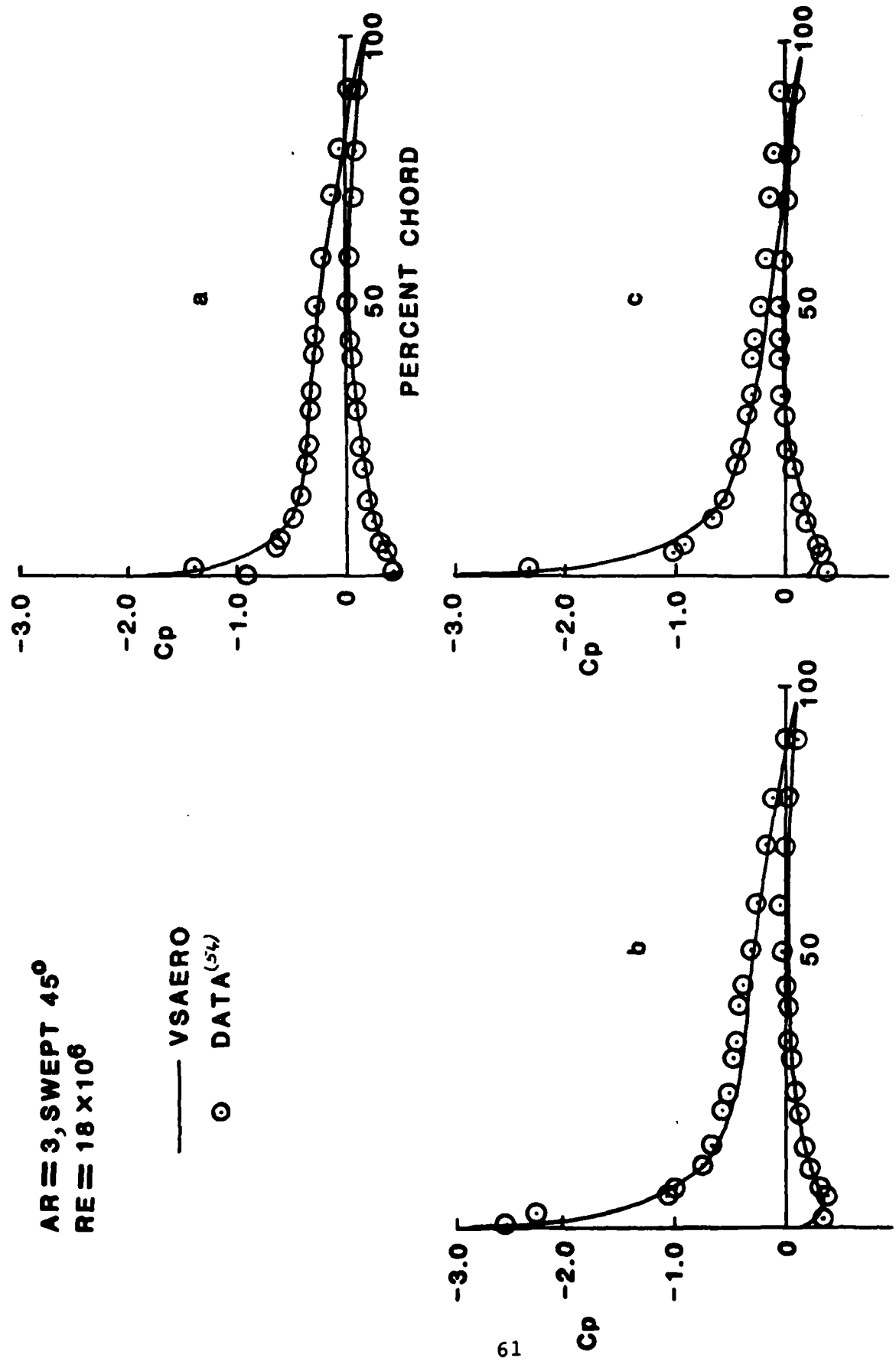


Figure 5.1.3. Comparison of Calculated and Experimental Spanwise Lift Distribution.

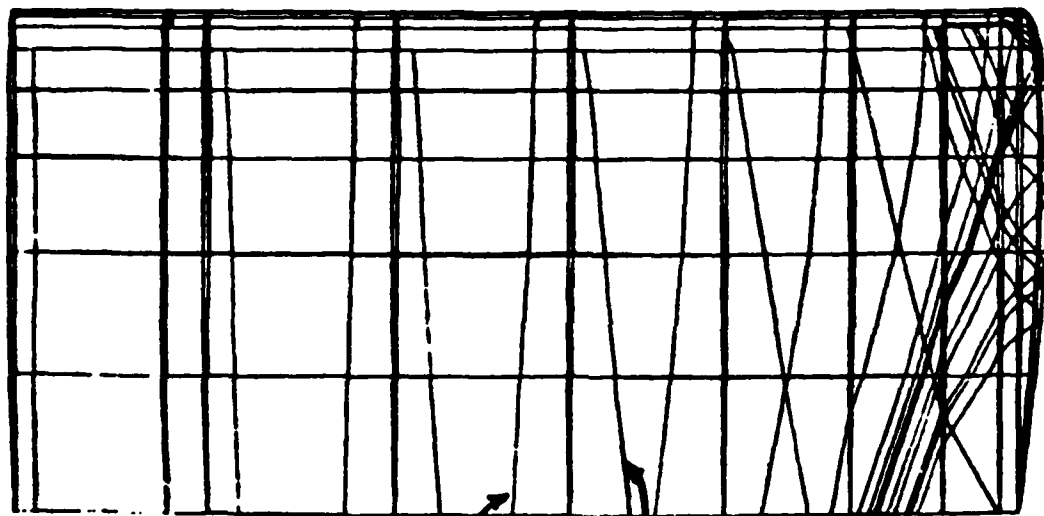
AR = 3, SWEEP 45°  
 RE = 18 x 10<sup>6</sup>

— VSAERO  
 ○ DATA (5%)



a) 19.5%, b) 70.7%, c) 92.5% SEMISPAN

Figure 5.1.4. Comparison of Measured and Predicted Pressure Distributions.



Top Surface  
Streamlines

Lower Surface  
Streamlines

**STREAMLINES ON WING**

XVUE= 0.00    YVUE= 10.00    ZVUE= 90.00

Figure 5.2.1. Calculated Streamlines on a Rectangular Wing.

RECTANGULAR TIP (HALF-ROUND SECTION)

ASPECT RATIO 4

NACA 0012 SECTION

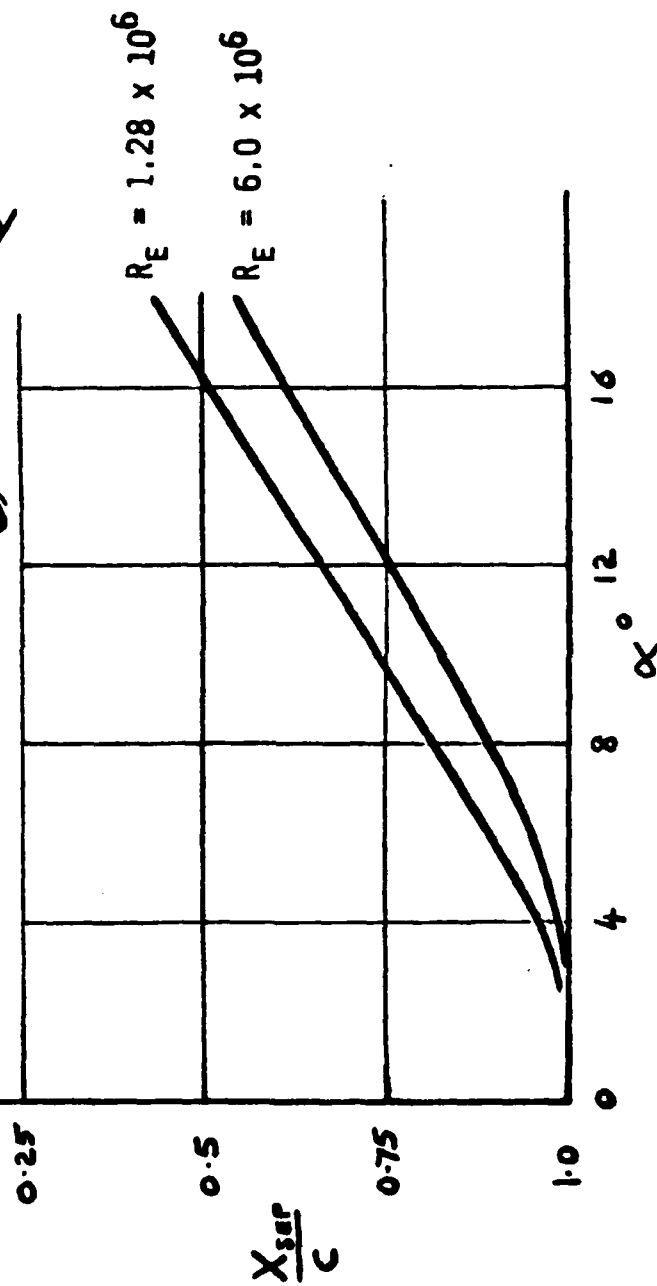
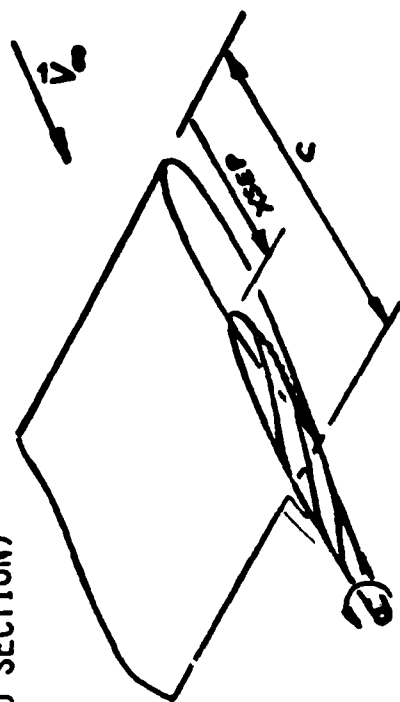


Figure 5.2.2. Effect of Angle of Attack on Extent of Tip-Edge Separation.

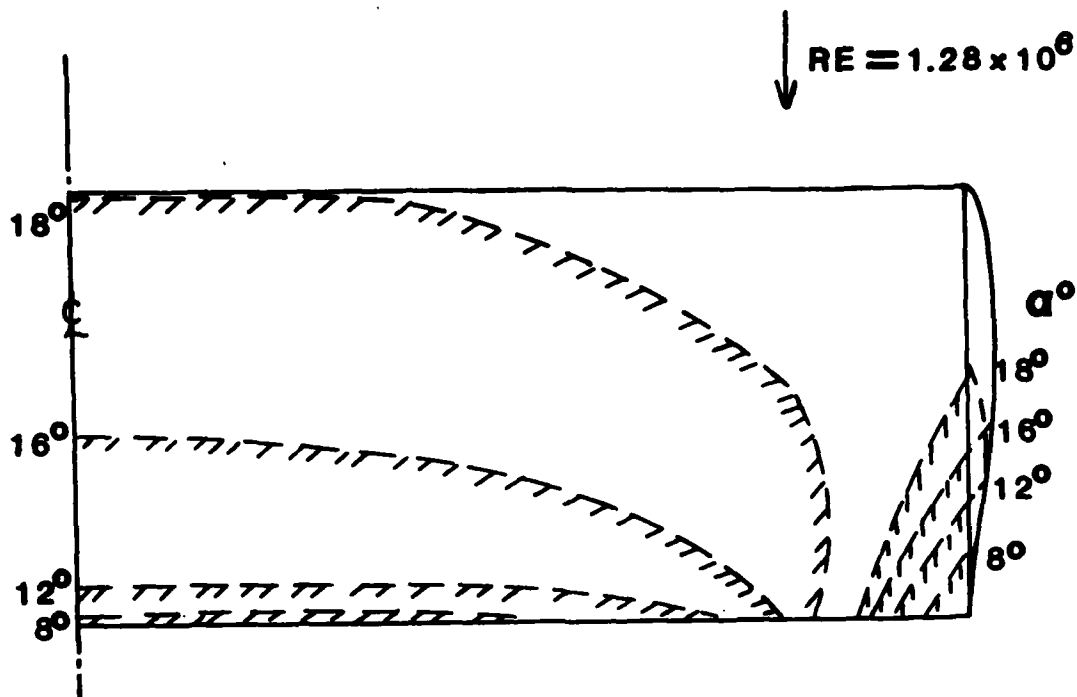
conditions for the first viscous/potential flow iteration cycle.

Figure 5.2.3 shows the plan view of the calculated separation boundaries for a range of angles of attack. Both tip-edge separation and separation boundaries over the inner part of the wing are indicated. Figure 5.2.3(a) shows the boundaries for a Reynolds number of  $1.28 \times 10^6$  and Figure 5.2.3(b) is for a Reynolds number of  $6 \times 10^6$ . At the lower Reynolds number, some laminar separation with no reattachment is indicated at  $18^\circ$  in the inboard region. At the higher Reynolds number, the extent of separation is considerably lower. It should be emphasized that the calculated separation boundaries in Figure 5.2.3 are for the initial solution only and would be expected to change when the separated vortex sheets are modelled in the analysis.

It is interesting to compare the shape of these calculated separation boundaries with experimental observations. Figure 5.2.4, taken from (7), is a sketch of the separated flow field of a rectangular wing. The calculated and experimental separation patterns are in remarkably close qualitative agreement.

An interesting feature of the separation boundaries (Figure 5.2.3) is that the inboard and tip-edge separation form two distinct zones even before the separated vortex sheets are modelled. A family of streamlines proceeding from the attachment line near the tip leading edge proceed over the upper surface and reach the trailing edge without separating and form a distinct attached flow zone between the inboard and tip-edge separation.

In Figure 5.2.5 three of these "attached" streamlines have been examined and show distinctly different characteristics. Streamline "A", starting just inboard of the tip on the lower surface, proceeds forward around the leading edge and then inboard over the upper surface. Streamline "B" starts at a point just outboard of "A" but "sneaks" around the tip edge onto the upper surface. Streamline "C" is predominantly a lower-surface streamline starting near "A"; however, it eventually passes around the tip edge and then proceeds over the upper surface to the trailing edge. The  $C_p$  history is plotted as a function of distance along the streamlines in Figure 5.2.5. Streamline "A" suffers a high suction peak during its passage over the leading edge and then negotiates a strong adverse pressure gradient over the upper surface. Streamline "B" passes through a mild suction peak on the tip edge and only a moderate adverse pressure gradient on the upper surface. Streamline "C" has a long favorable pressure gradient until it has passed around the tip edge.



WING ASPECT RATIO: 4  
 WING SECTION: NACA 0012  
 WING TIP: HALF-ROUND

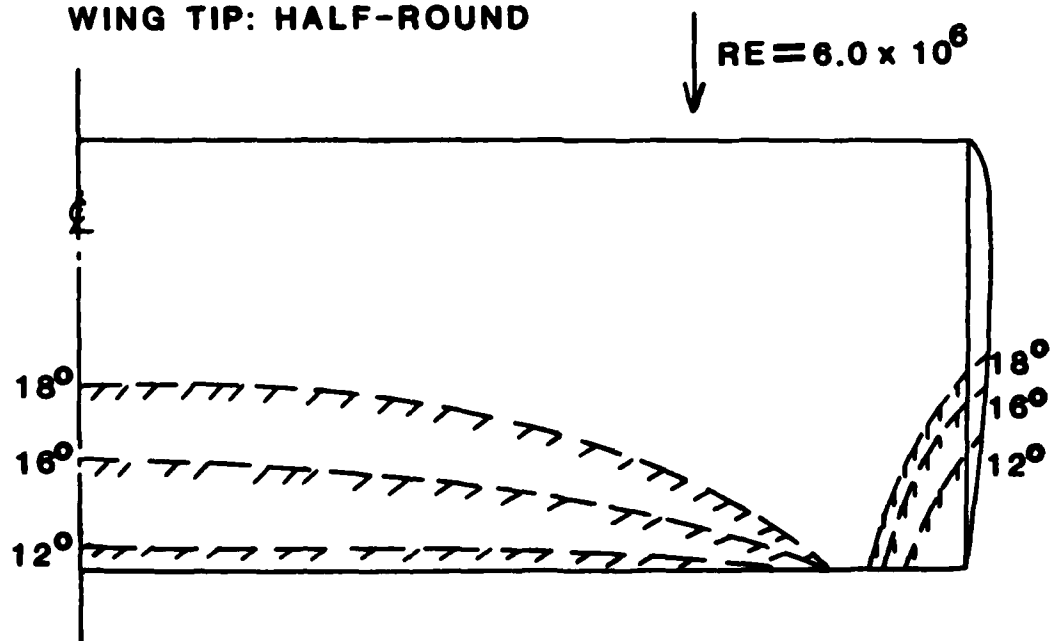


Figure 5.2.3. Calculated Separation Boundaries for a Range of Angles of Attack at Two Reynolds Numbers.

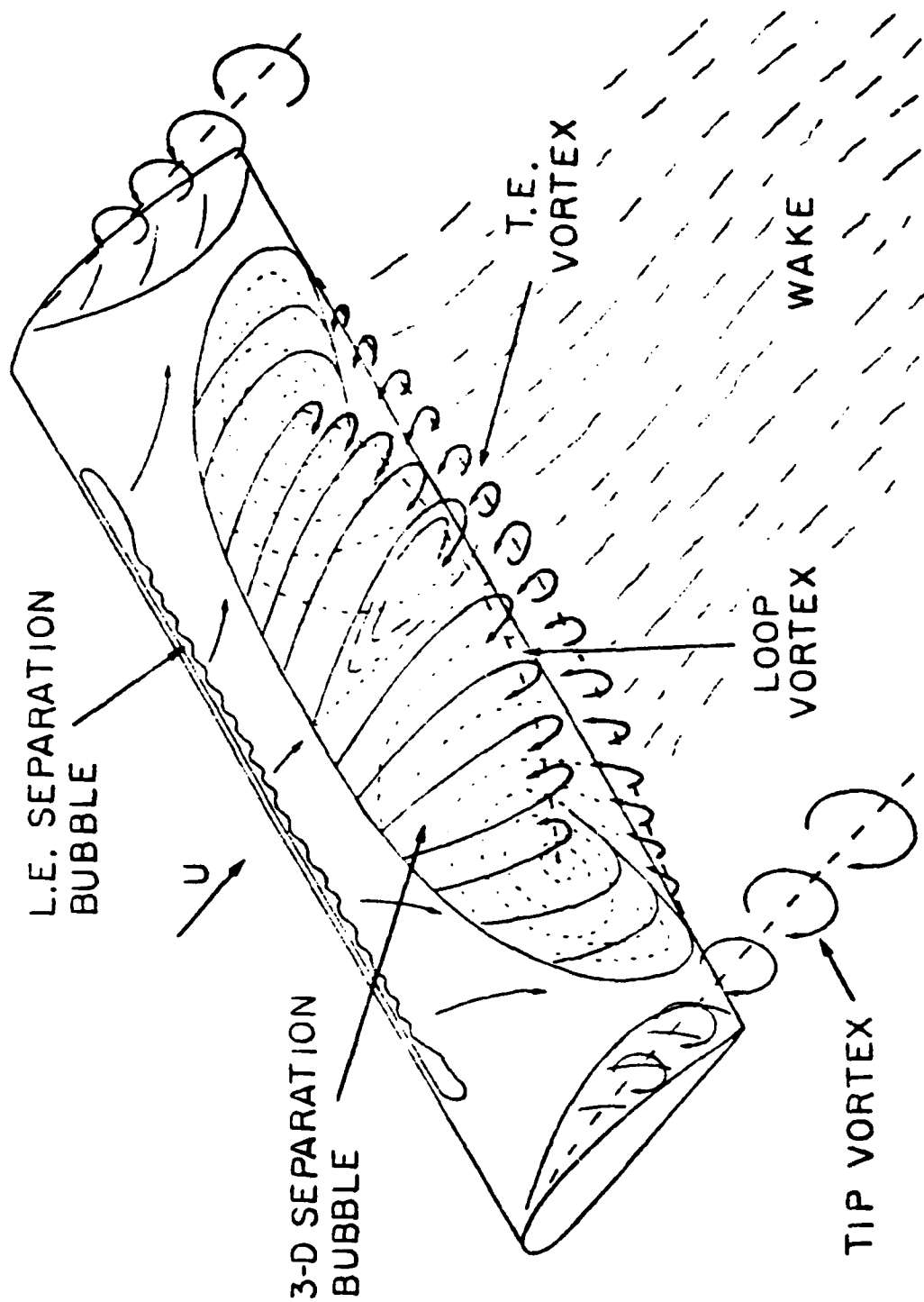
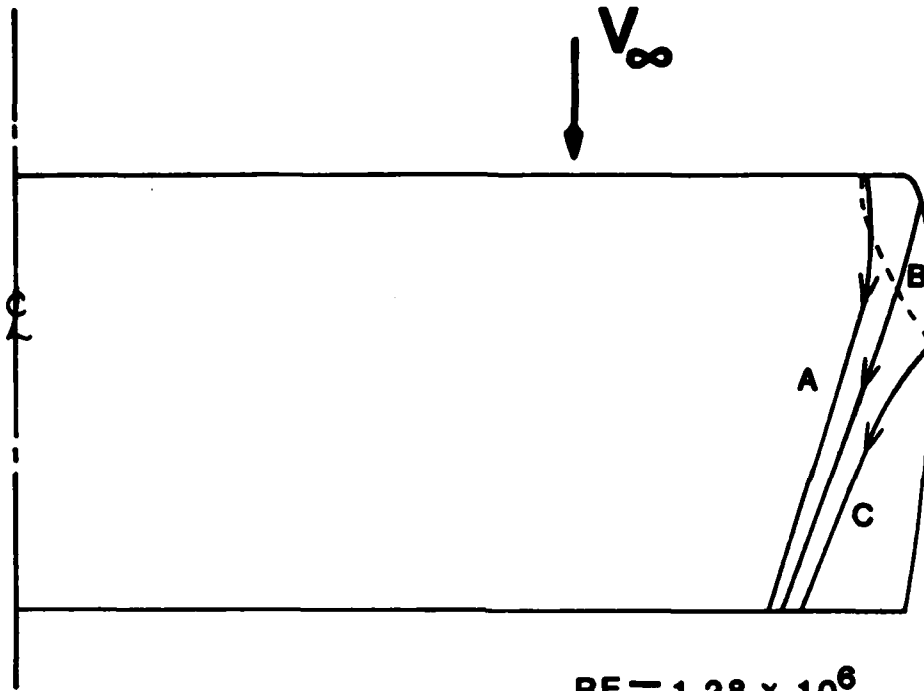


Figure 5.2.4. Tentative Flow Field Model for Low Aspect Ratio Wing just Beyond Stall (Winklemann (7)).



$RE = 1.28 \times 10^6$

$\alpha = 16^\circ$

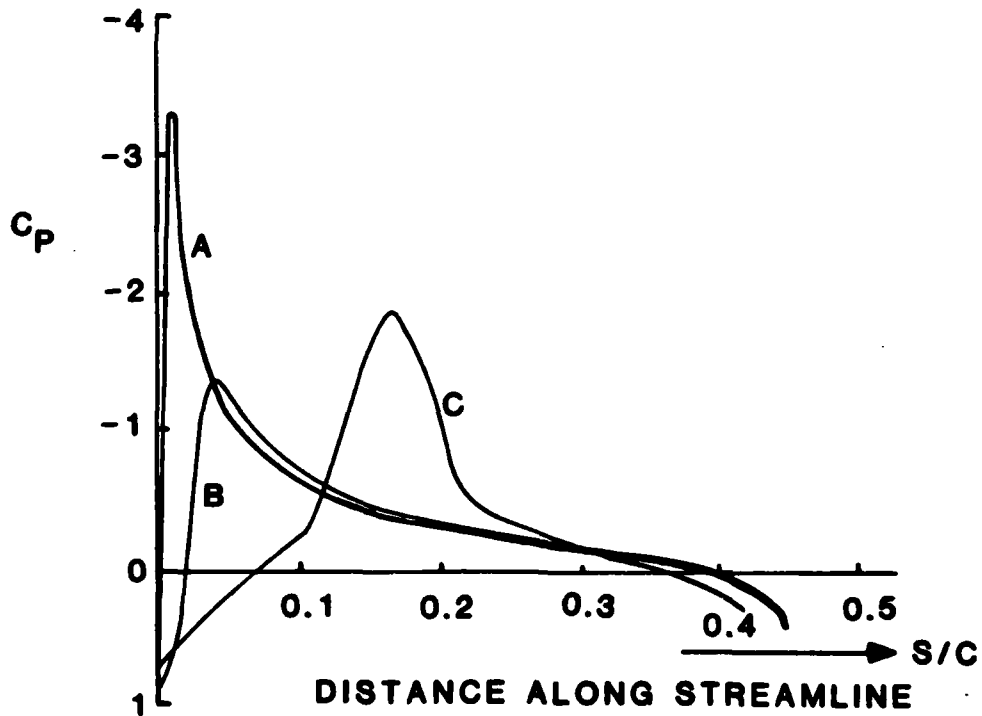


Figure 5.2.5. Calculated Pressure Distributions along Three (External) Streamlines Starting near the Tip.

Streamlines inboard of "A" have to negotiate higher leading-edge suction peaks and eventually define the inboard separation zone. Streamlines outboard of "C" see their suction peak occurring later along their length, but the peak value rises sharply at stations nearer the trailing edge and this leads to the tip-edge separation zone.

Clearly, the pattern of separation boundaries is very dependent on the section and planform shapes and also on the tip-edge profile. The latter, in particular, strongly influences the tip-edge separation and, hence, the formation of the tip-edge vortex. The VSAERO program is now capable of locating separation boundaries on any tip-edge shape (planform or section profile) and could clearly be applied to a more fundamental investigation of tip-edge vortex formation. Knowledge of the pressure histories and boundary layer characteristics could be used as a guide to suggest changes in tip geometry to control the edge vortex characteristics.

A number of calculations were performed for a  $30^\circ$  swept untapered wing. The wing has a twist of  $4^\circ$ , tip nose-down about the half-chord line, and a NACA 0012-64 section. The wing tip is a half-body of revolution based on the NACA section shape. The wing was extensively tested at the National Aerospace Laboratory (NLR) in Amsterdam (55).

Figure 5.2.6 compares calculated and measured pressures around the tip surface at a local  $x/c$  station of .72. (The experimental values were interpolated at the calculation station). The calculation includes the effect of tip-edge vortex separation after three wake-shape iteration cycles. The comparison in the pressure distribution is remarkably good except that the calculation underpredicts the suction level on the top surface under the tip vortex. Although the calculation has produced a reversal in the spanwise flow--outboard here under the vortex--the magnitude of this cross flow is probably underpredicted at this time. One possible reason is that the wake panels in this tip-edge roll-up are extremely skewed and so the flat projected panel model is certainly leaving large gaps in the effective surface for which the influence coefficients are evaluated. This will certainly have an effect on the doublet solution on the local surface panels under the vortex roll-up.

Figure 5.2.7 compares the calculated chordwise pressure distribution against experimental measurement at a section approximately one chord length outboard of the plane of symmetry for an angle of attack of  $16^\circ$ . A detailed comparison between calculated pressure distribution on the wing and experimentally measured values at various spanwise sections is presented in Figure 5.2.8. The separation of flow from the

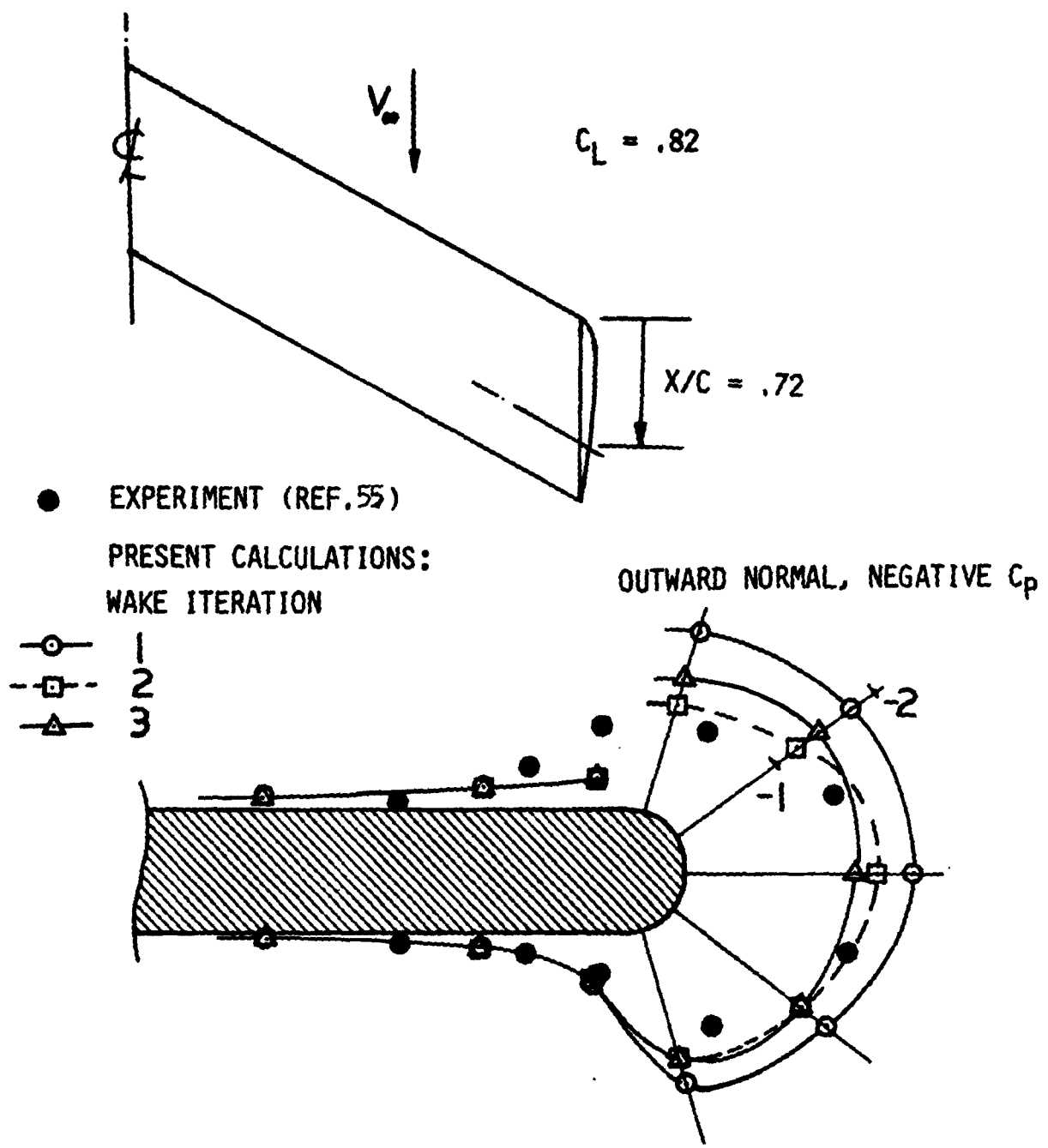
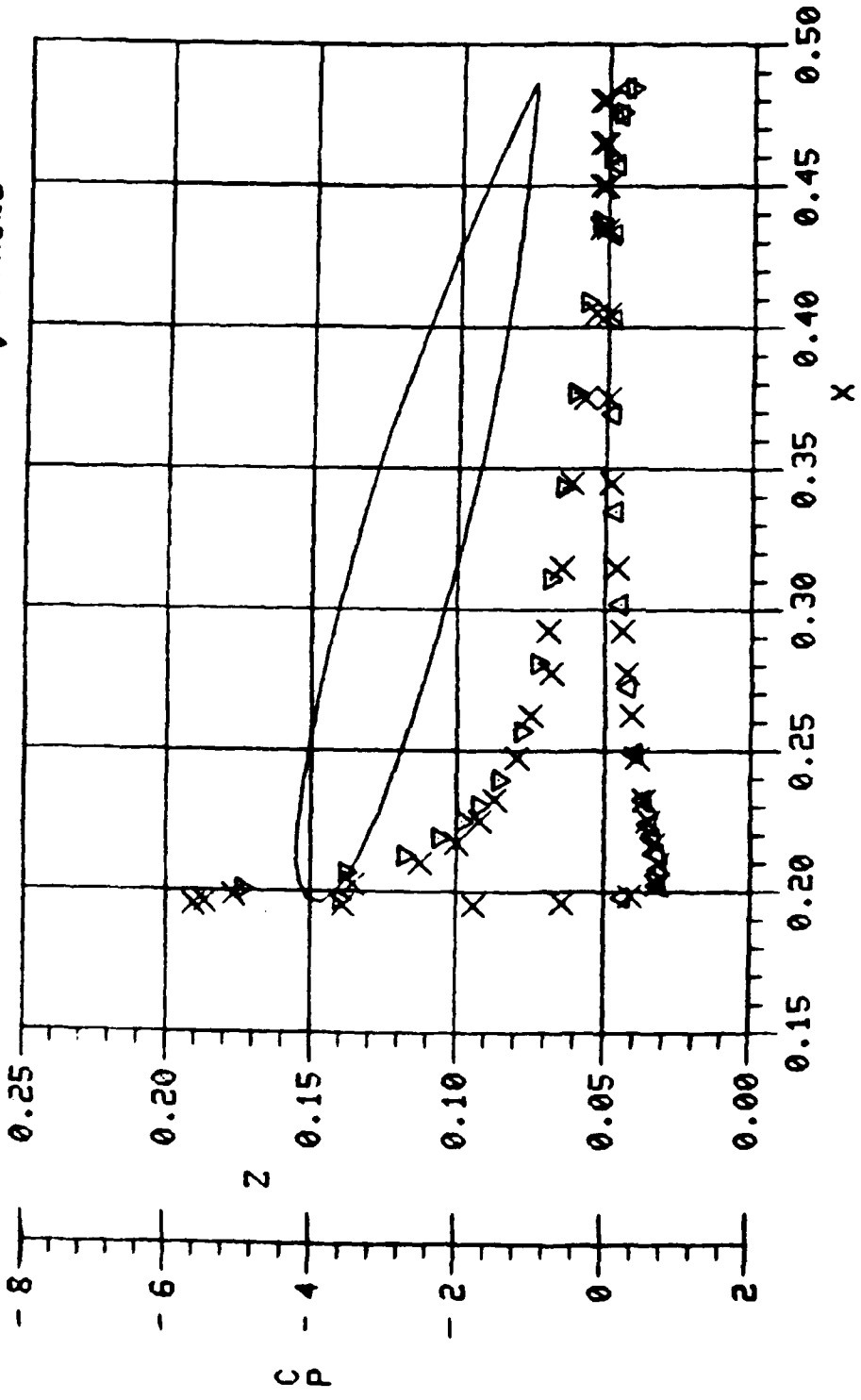


Figure 5.2.6. Spanwise Pressure Distribution Calculated Near the Tip of a Swept Wing with Prescribed Edge Separation.

X Exp. (55)  
 ▽ vsnro

AERODYNAMICS DATA



COMPARISON WITH EXP. DATA, ALPHA=16.0, IT=1, NLRWING  
 BUTTLINE CUT Y = 0.31

Figure 5.2.7. Chordwise Pressure Compared against Experiment at y/c = 1.0.

# Pressure Comparison

□ Experiment  
— Theory

Angle Of Attack  $16^\circ$

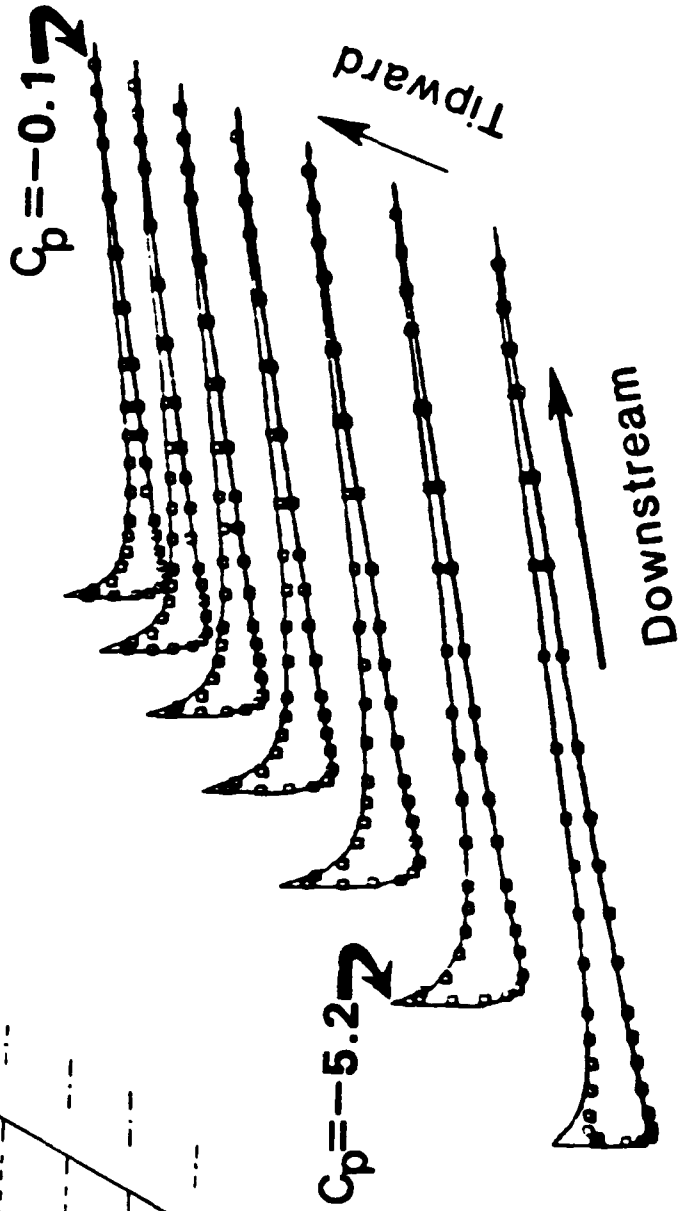
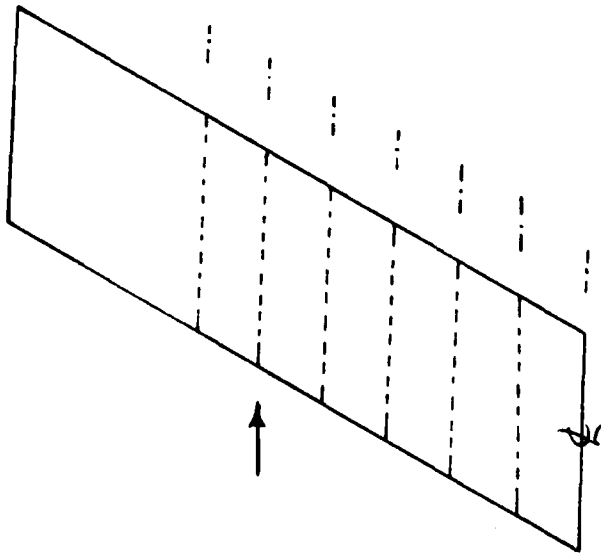
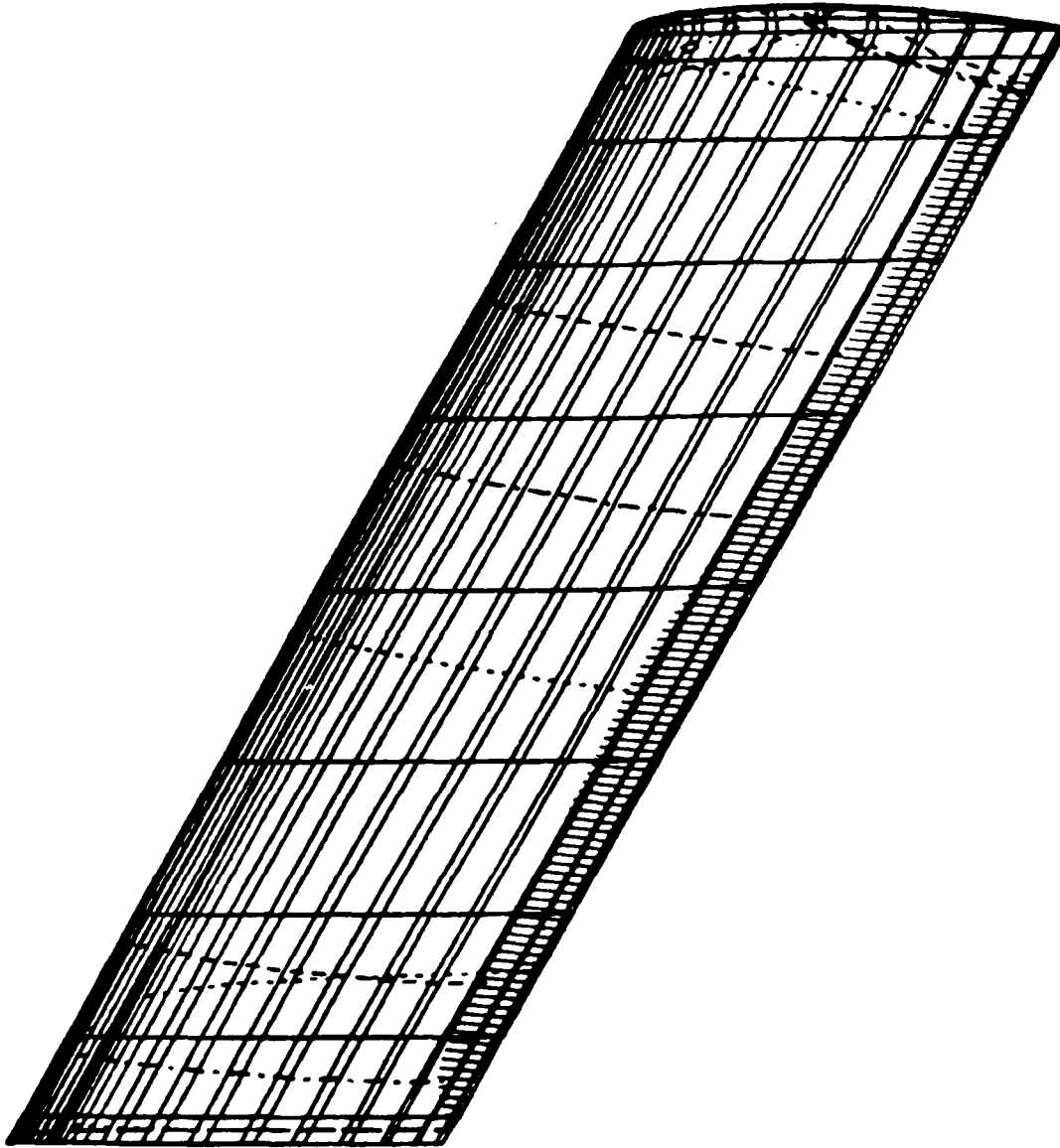


Figure 5.2.8. Chordwise Pressure at Various Spanwise Stations Compared against Experiment.

wing surface as calculated by the boundary layer procedure along the streamlines is shown in Figure 5.2.9, while the experimentally photographed oil patterns are reproduced from (55) in Figure 5.2.10. Experiment shows a slightly more extensive separation. The separation predicted by the calculation uses a wake attached to the trailing edge, whereas the actual wake emanates from the separation line. Past experience as reported in (4) indicates that the separation line tends to move forward as the iteration proceeds. The present calculation, being the first iteration in wake positioning the prediction of less extensive separation, is correct.

Vector plots of the off-body velocity calculation in planes normal to the free stream flow direction are presented in Figure 5.2.11(a) through (c) at three-x-locations downstream of the wing. The inboard movement of the tip vortex with distance downstream is obvious from the figure. Experimentally measured sidewash (velocity in the y-direction) is compared against the calculation in Figure 5.2.12. The x-location of the scan is 20% of the chord downstream of the wing tip while the y-location is about 3% of the chord inboard of the tip. The agreement is very good except for the peak velocity value. The calculated value depends on the applied core model. In this calculation, a Rankine core of radius 2.5% of  $\bar{c}$  was applied to remove the infinite velocity of the potential vortex.

A basic challenge for separated flow modeling is provided by the sphere. Calculations of surface streamlines over the surface of a sphere were examined in Section 3.2. We now continue that calculation through a viscous/inviscid iteration cycle at a Reynolds number of  $4.25 \times 10^6$  based on diameter. Figure 5.2.13 shows the prescribed wake geometry, separation line and external surface streamlines for the calculation. The separation is at  $132^\circ$  in the experiment. Manually stepping the program for a separation just ahead and just behind this location has analytically confirmed this position within one panel dimension. The calculated pressure distribution is compared with experimental data (56) in Figure 5.2.14. Two ordinate scales are included in this figure--one for the coefficient of pressure and another for the corresponding body geometry outline. It is seen that the boundary layer source distribution (i.e., the difference between the first and second iteration) fills and smooths the dimple in the pressure field of the first iteration such that the calculated pressure is continuous through the separation region. Further, the computed and experimental pressures agree quite favorably even in the separated zone. In addition, the computed drag coefficient (integrated skin friction drag not included) based on frontal area is .06, while that measured was .085.



NLRWING ,ALPHA=16.0,ITR=3

XVUE= 0.00

YVUE=

0.00

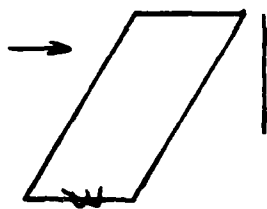
ZVUE= 14.35E+06

Figure 5.2.9. Calculated Flow Separation Boundary.

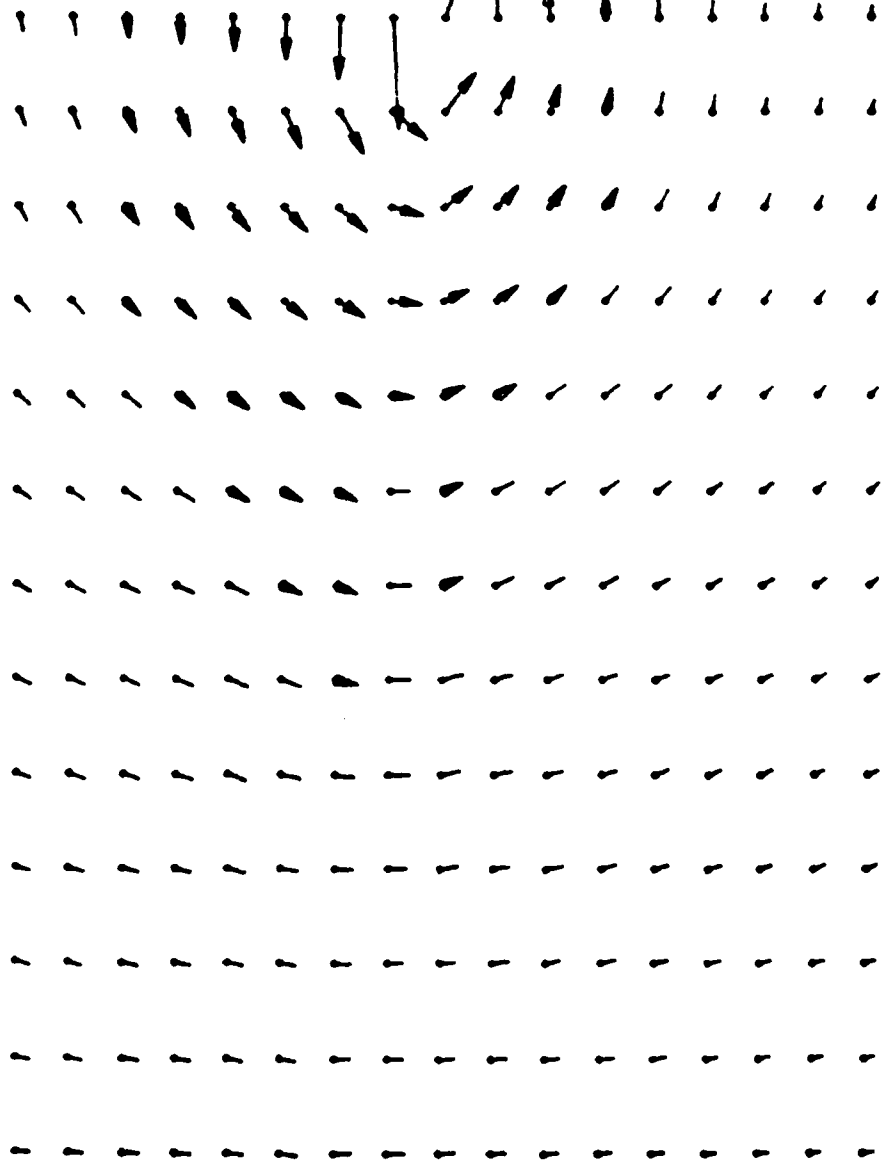


$\alpha = 16^\circ$ . NOTICE THE SEPARATED FLOW REGION ALONG  
THE TRAILING EDGE, WHICH KEEPS FREE OF OIL.

Figure 5.2.10. Oil Patterns on the Upper Surface of the  
Wing Reproduced from Reference 55.



OFF BODY DATA      BLOCK 1      I-PLANE 1



U<sub>Z</sub>

L

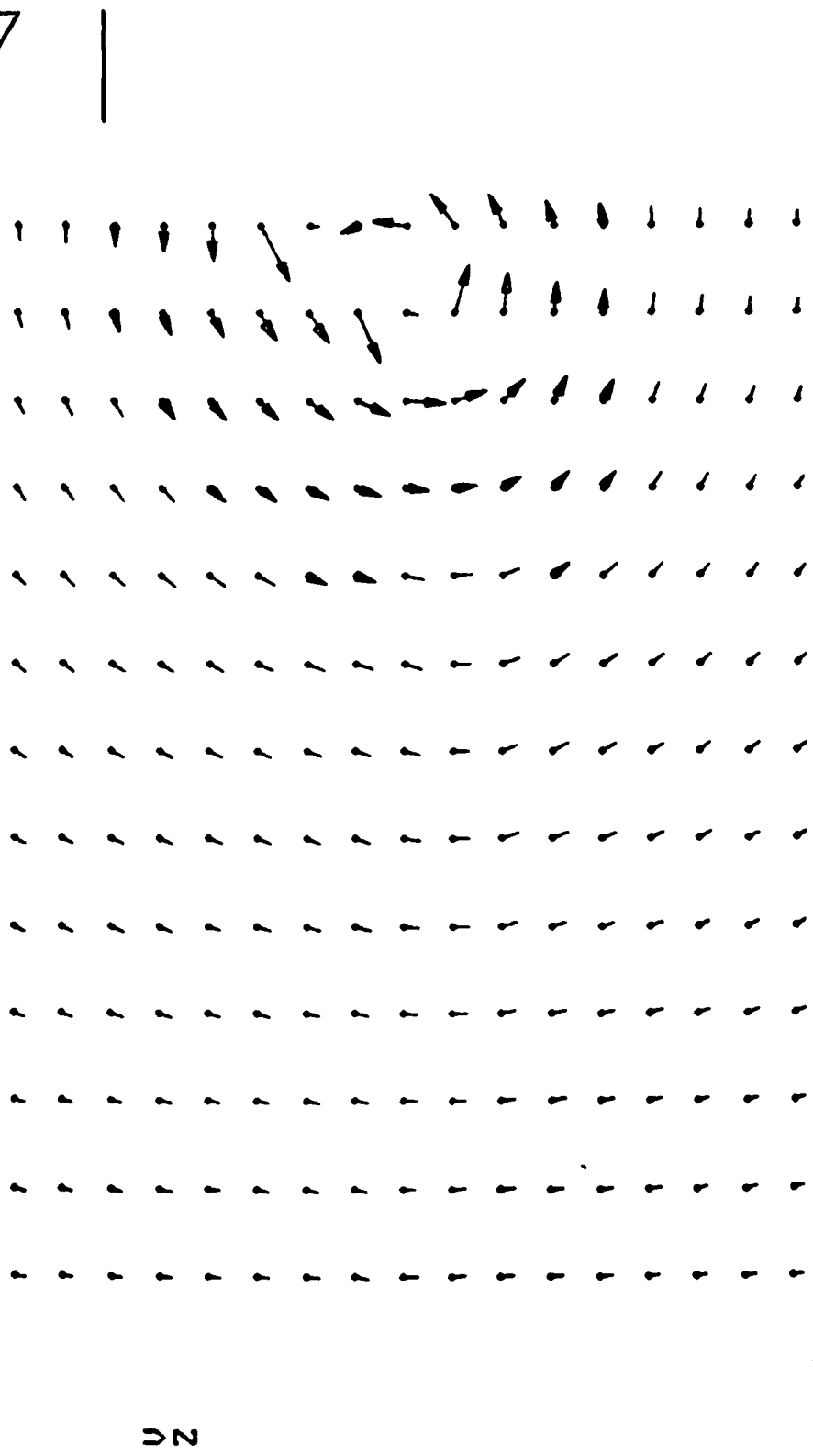
U<sub>Y</sub>

**NLRWING WITH RELAXED WAKE**

(a) x-Station Close to Wing Tip.

Figure 5.2.11. Vector Plot of Off-Body Velocity in y-z Plane Normal to Free Stream Direction.

OFF BODY DATA      BLOCK 2 I-PLANE 1



U Z

L

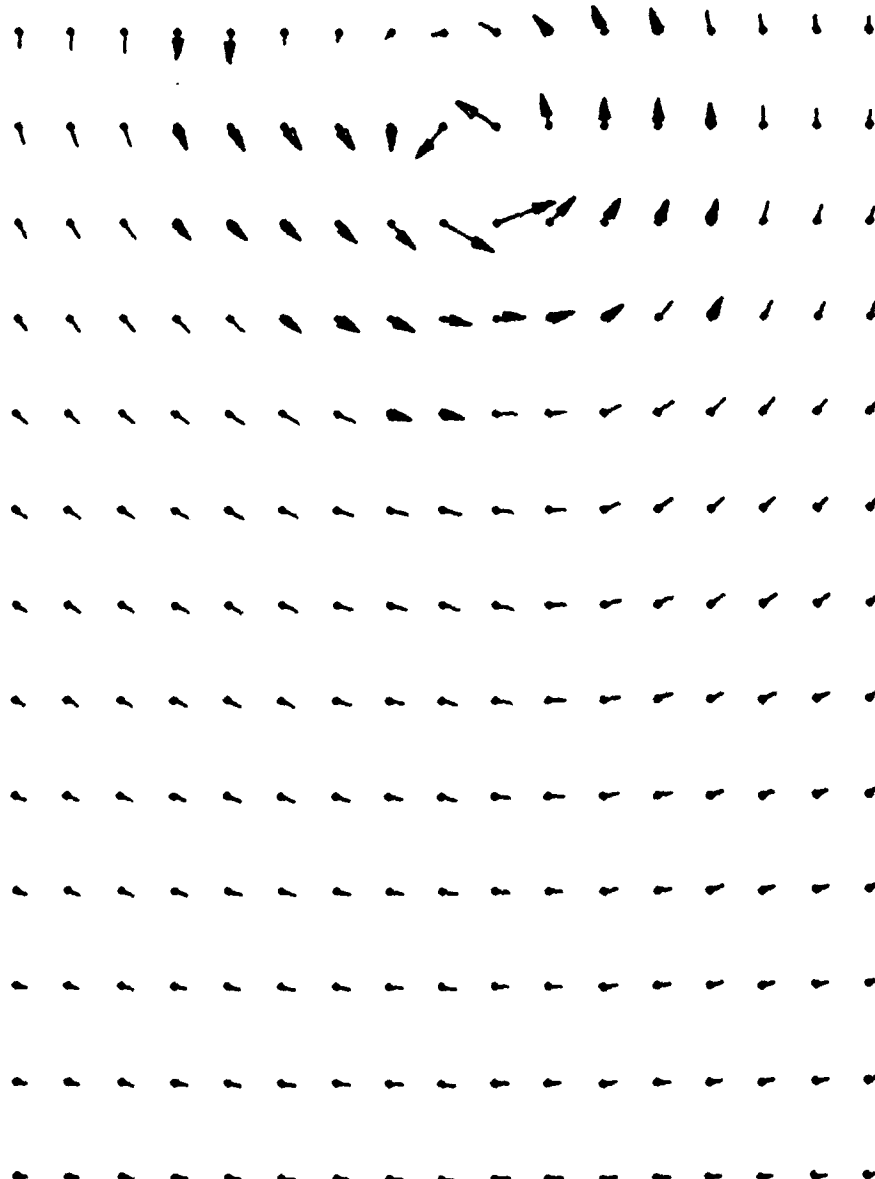
UY

NLRWING WITH RELAXED WAKE

(b) x-Station One Chord Length Downstream of Tip.

Figure 5.2.11. Continued.

OFF BODY DATA      BLOCK 3 I-PLANE 1



U<sub>Z</sub>

L

UY

NLRWING WITH RELAXED WAKE

(c) x-Station Two Chord Lengths Downstream of Tip.

Figure 5.2.11. Concluded.

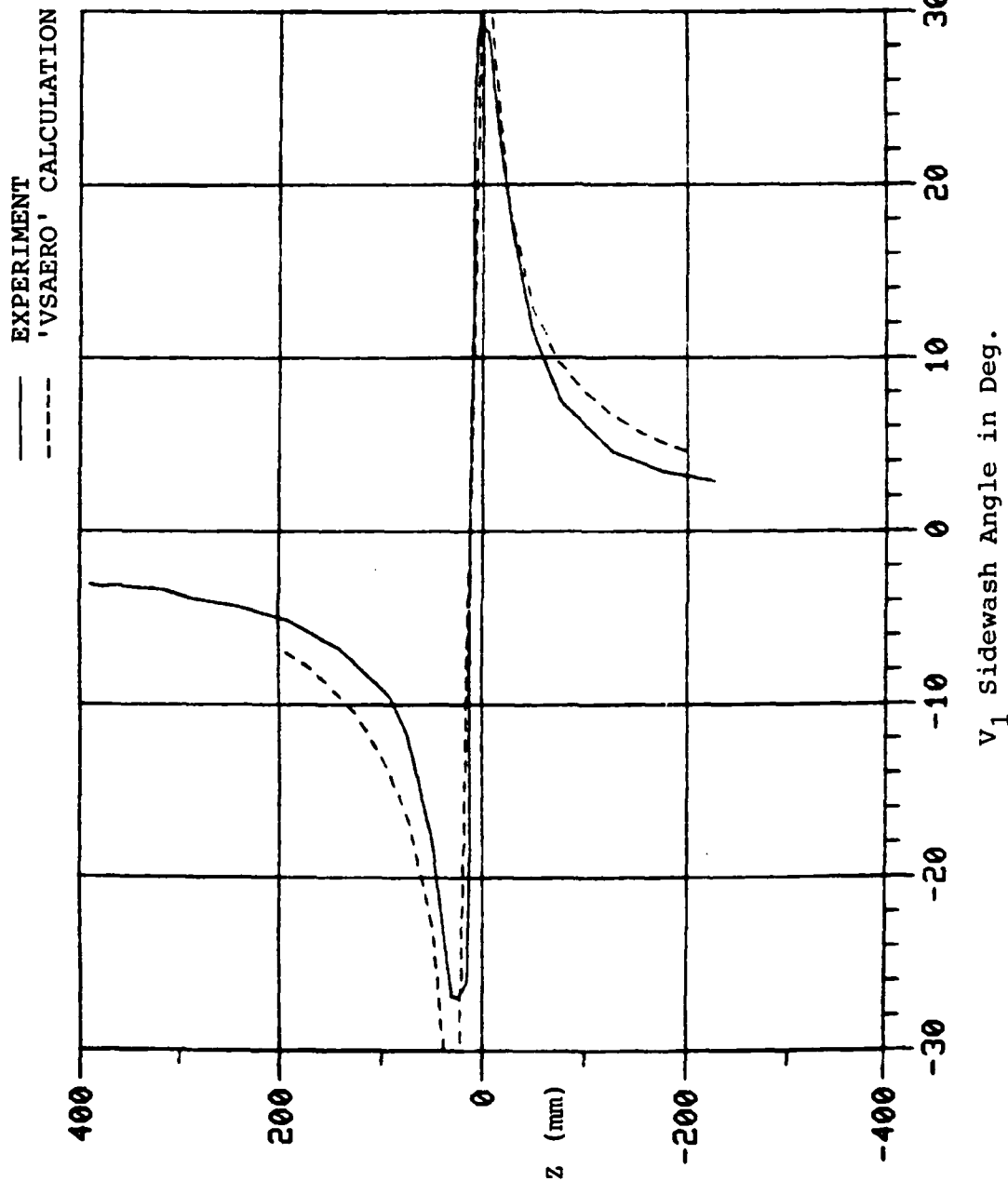
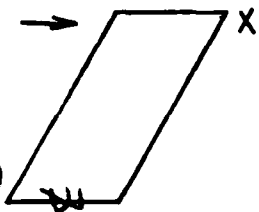


Figure 5.2.12. Off-Body Velocity Compared Against Experiment (Ref. 55);  
 Angle of Attack  $16^\circ$ ,  $x = 60$  mm Downstream of Tip,  
 $y = 10$  mm Inboard of Tip.

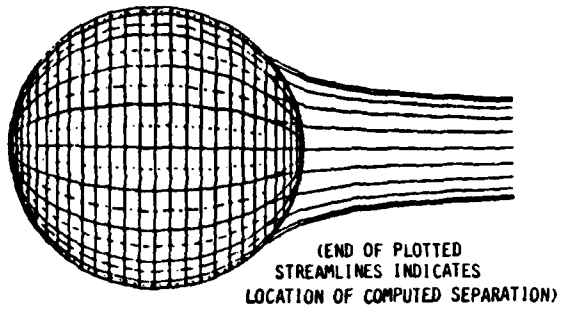


Figure 5.2.13.

Calculated Streamlines and Separated Flow Wake on a Sphere for  $Re = 4.28 \times 10^5$ .

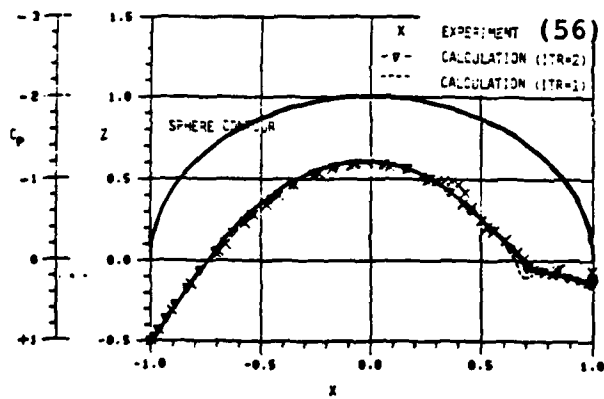


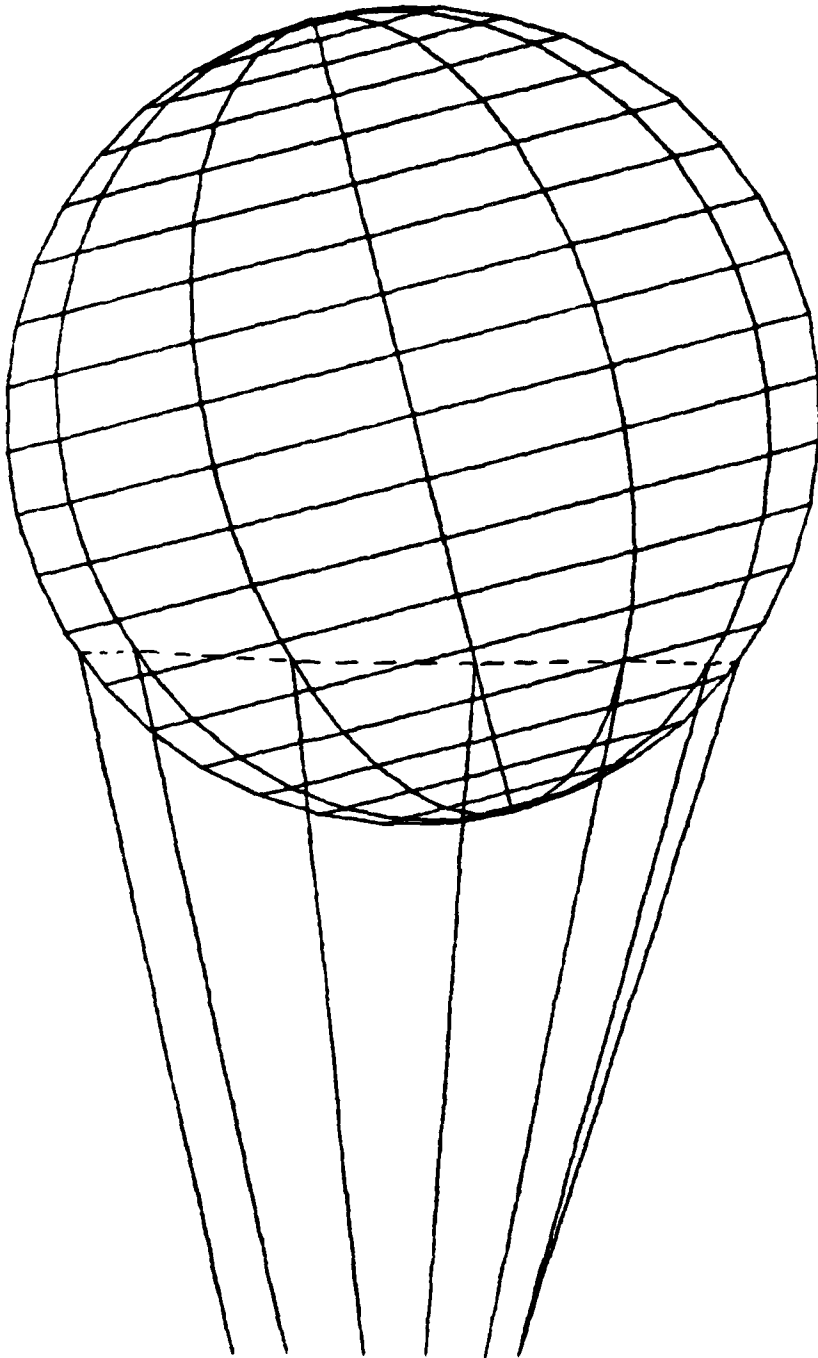
Figure 5.2.14.

Comparison of Calculated and Experimental Pressure Distributions on a Sphere at  $Re = 4.25 \times 10^5$ .

The sphere case is also a useful case to test the arbitrary separation line procedure. The program was first run with a prescribed separation line at  $\theta = 126^\circ$ . The paneling was then rotated through  $15^\circ$ , Figure 5.2.15, leaving the separation line fixed in space. The arbitrary separation line routine then identified the new set of separation panels and an approximation to the previous separation line by projecting it onto the "new" surface, Figure 5.2.16. While the new solution gave good agreement with the previous solution in the attached flow zone, the pressures in the base region showed some sensitivity to the relative location of the separation boundary and the next panel upstream. While the average base pressure agrees with the earlier solution, there is some variation in local values. This sensitivity would be expected to decrease with a higher panel density.

The separated flow model was tested on a  $10^\circ$  swept wing at  $21^\circ$  incidence. The constant chord wing had an aspect ratio of 3. The number of panels representing the wing was 260, arranged in a 40 (chordwise) by 5 (spanwise) array on the main surface and a  $3 \times 20$  array on the tip surface. The latter was a half-body of revolution based on the NACA 0012 profile of the wing. Calculations were performed using a prescribed separation line corresponding to experimental measurements (57); the x-location of this line was approximately .06 of the chord back from the leading edge. For these calculations, region W of the wake (Figure 3.1.1) extended about 5 chord lengths beyond the trailing edge. (Preliminary calculations had confirmed earlier findings (2) that unlike the two-dimensional case (4), the solution in the three dimensions is relatively insensitive to the length of the vortex sheet modeling the shear layer.) In the present calculations, 18 panels were used to represent the linear doublet distribution on each streamwise strip of wake panels. The wake geometry was prescribed, leaving the surface at approximately  $\gamma/2$ , based on earlier experience (4), (5). The wake was shed continuously along the upper surface separation line to the tip, down the tip edge to the trailing edge and back along the lower side of the trailing edge.

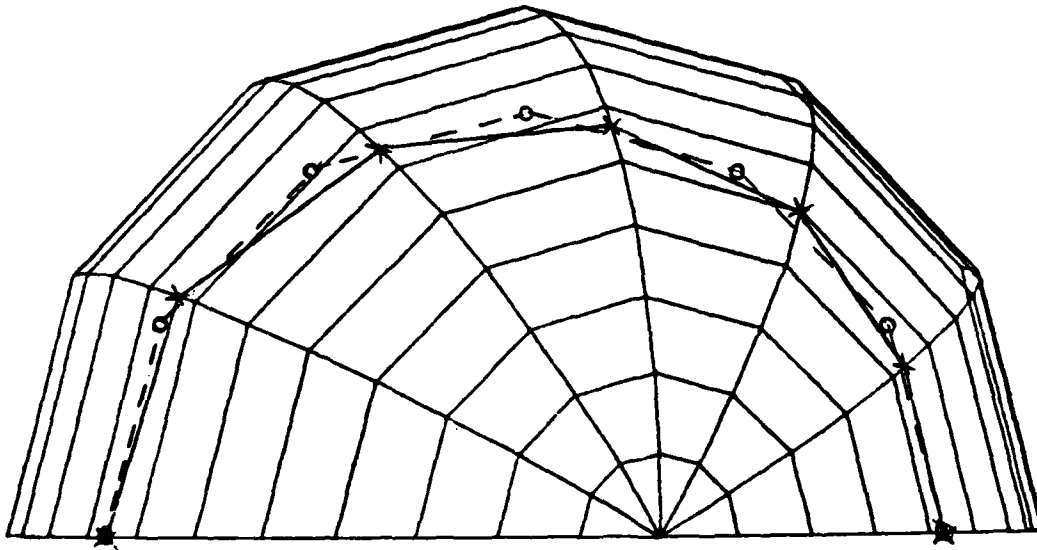
Figure 5.2.17 shows calculated pressure distributions compared with experimental measurements (57) at two spanwise stations,  $\eta = .6$  and  $.9$  of the semispan approximately. The calculations include the case of fully attached as well as separated flows and indicate the large influence of the separated flow model. (Note that the attached flow pressures at the  $\eta = .9$  station are perhaps shifted too much in the negative direction over the downstream half of the chord. This is because this station is at the last column of panels before the tip edge and so the spanwise acceleration of the flow as



XUUE• 0.00 YUUE• 14.35E+06 ZUUE• 0.00

Figure 5.2.15. Sphere with Paneling Rotated 15°.

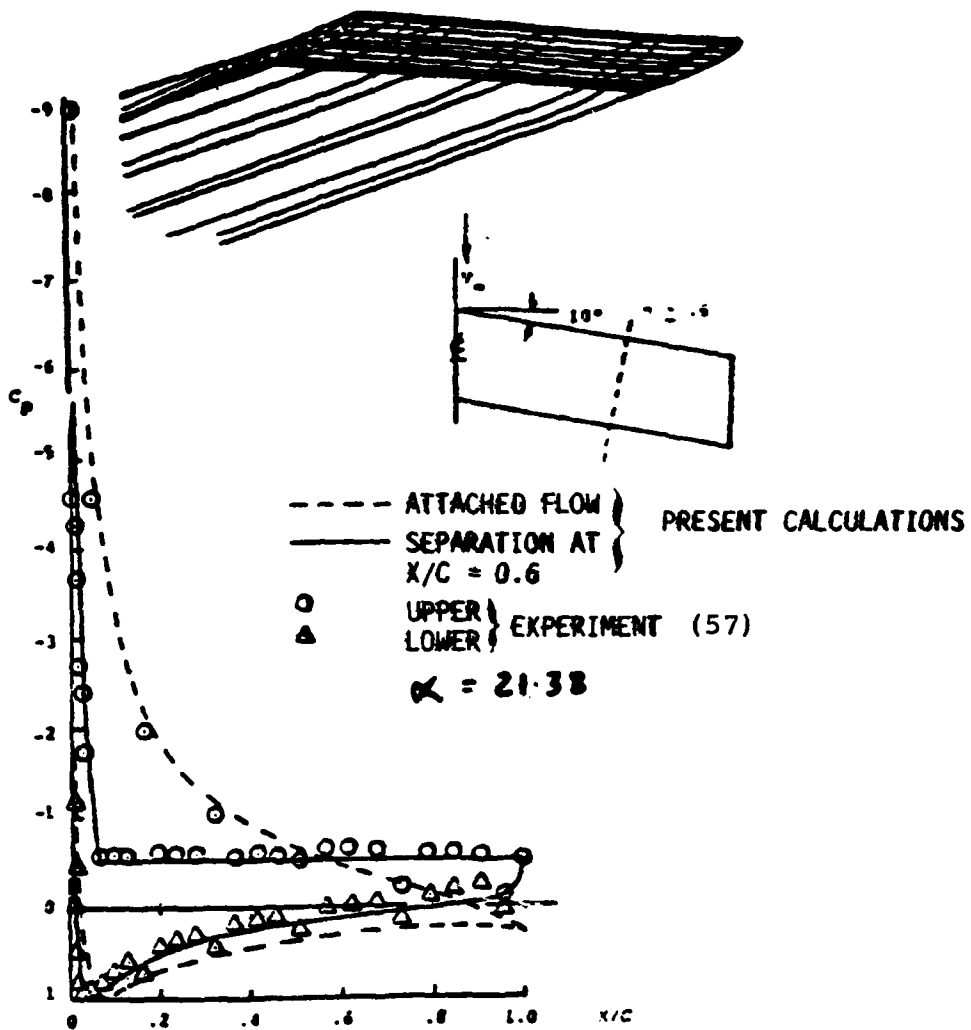
--o-- SEPARATION POINTS (INPUT)  
 -x- POINTS LOCATED BY NEW PROCEDURE



SPHERE TEST ROTATED 15.0 REAR VIEW

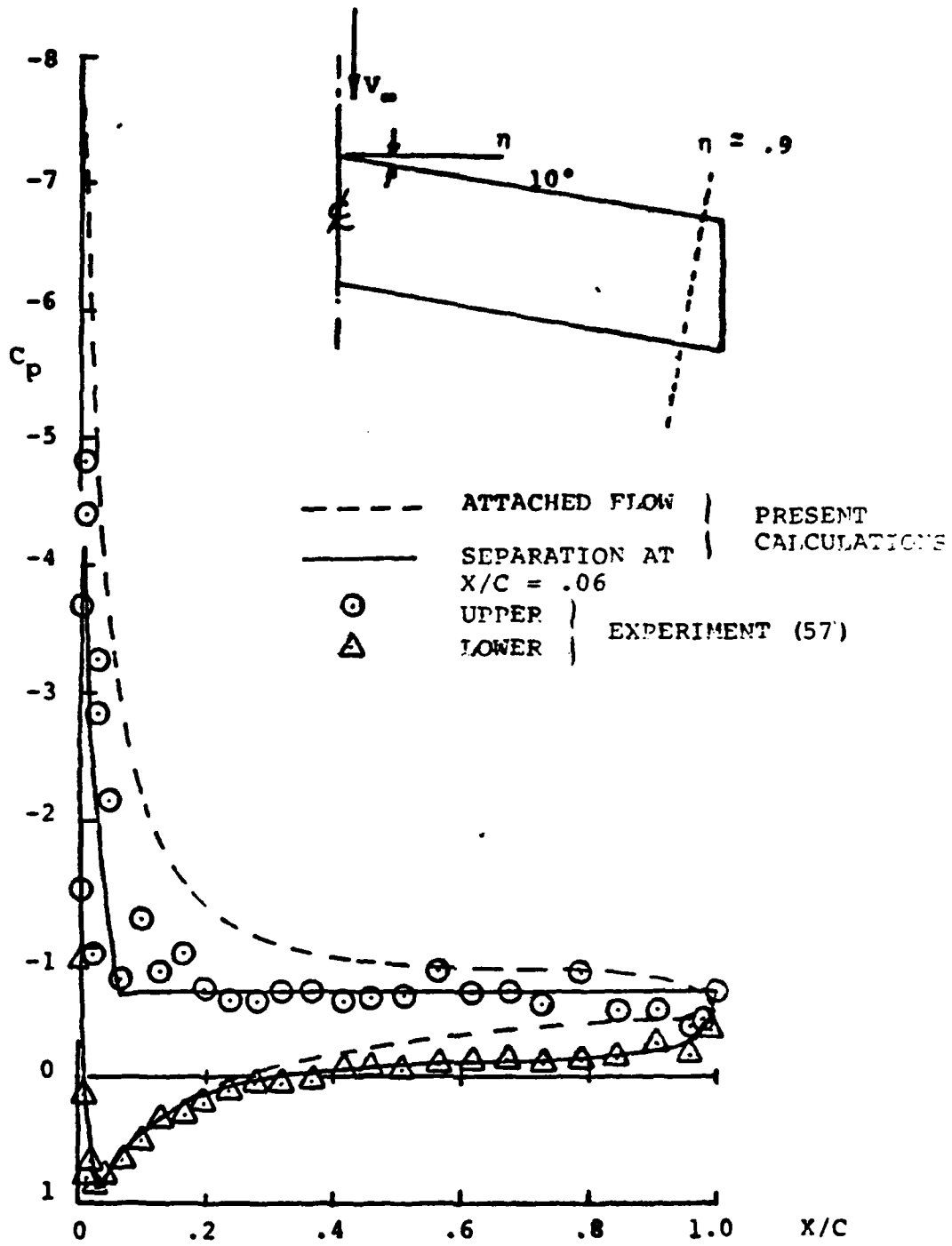
X/VE= 14.35E+06      Y/VE= 0.00      Z/VE= 0.00

Figure 5.2.16. Separation Line Identified by New Procedure.



(a)  $\eta = 0.6$ .

Figure 5.2.16. Comparison of Calculated and Experimental Pressure Distributions at Two Stations on a Wing with Extensive Separation.



(b)  $\eta = .9$ .

Figure 5.2.17. Concluded.

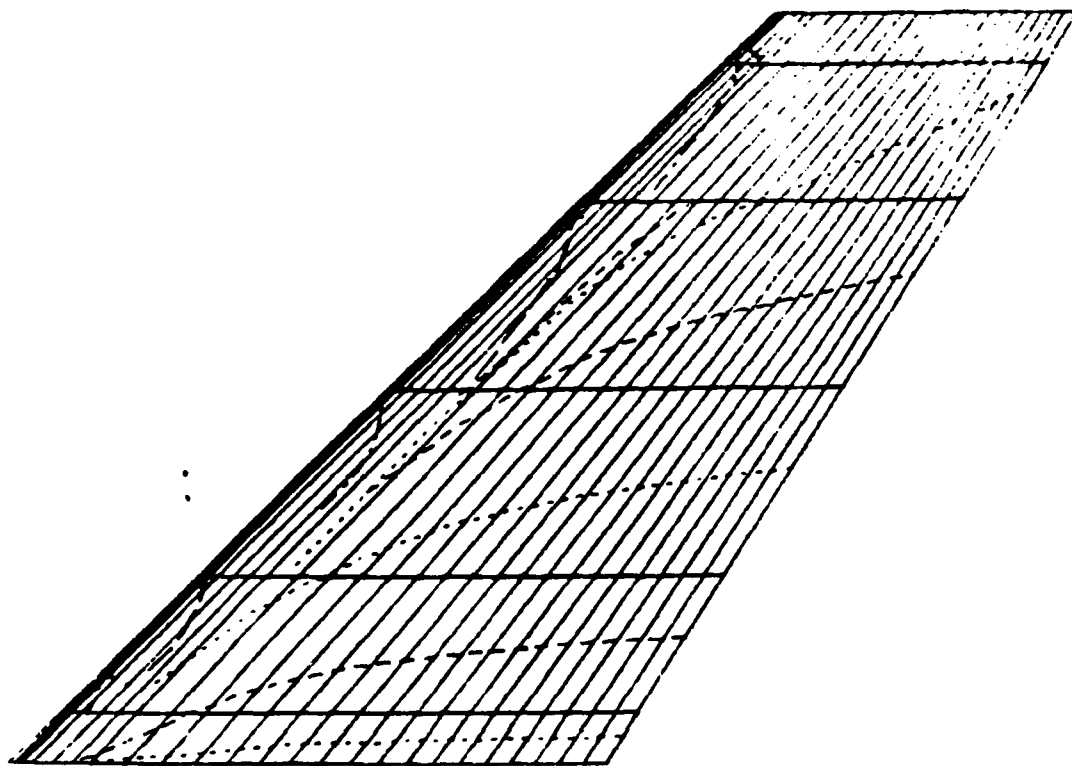
it passes around the tip surface (see Figure 5.2.6) is calculated prematurely. This problem is less severe for the separated flow case because of the influence of the tip-edge separation model. In any event, more columns of panels would normally be used in the tip region.

The results from the separated flow model compare very favorably with the experimental data. In particular, the pressure in the separated region is in very good agreement and should lead to a good prediction of the drag force. Differences in the peak suction area may be caused by incorrect location of the separation line; i.e., a small forward movement at the inboard station and a small rearward movement at the outboard station would improve the predictions.

It is clear from the experimental results in Figure 5.2.17 that the separation was unsteady and it is interesting to observe that some of the apparently "bad" values are, in fact, very close to the attached flow calculation. This is particularly so at the  $\eta = .6$  station.

The computation time for the separated flow case was 96 seconds of CDC Cyber 175 time, which is approximately equivalent to 24 seconds on the CDC 7600. It should be emphasized, however, that this calculation represents just the first pass through a complete solution. Even so, such a computation time is a good basis for practical computing costs for a complete iterative procedure.

Finally, the Kolbe and Boltz (54) wing considered earlier for the basic viscous/inviscid calculation was examined over a range of angles of attack including modeling of the predicted separation flow zones. Figure 5.2.18 shows a family of calculated (external) streamlines at  $\alpha = 24^\circ$ , Reynolds No.  $8 \times 10^6$ , and Mach number .25. The upper and lower streamlines indicate the location of the attachment line. The lower surface streamlines then sweep outboard while the upper surface set pass outboard and around the leading edge. Separation is predicted just downstream of the leading edge. The predicted  $C_L \sim \alpha$  curve is compared with the experimental measurement in Figure 5.2.19. The comparison is very favorable; however, further correlation studies should be pursued for this set of data. In particular, the data includes the effect of Reynolds number on the extent of leading-edge vortex formation which was not included in this initial correlation study.



KOLBE/BOLTZ WING    ALPHA=24,    M=0.25,    RE=4 MILLION  
 XVUE= 0.00    YVUE= 0.00    ZVUE= 1.40E+07

Figure 5.2.18. Calculated Streamlines on a Swept Wing.

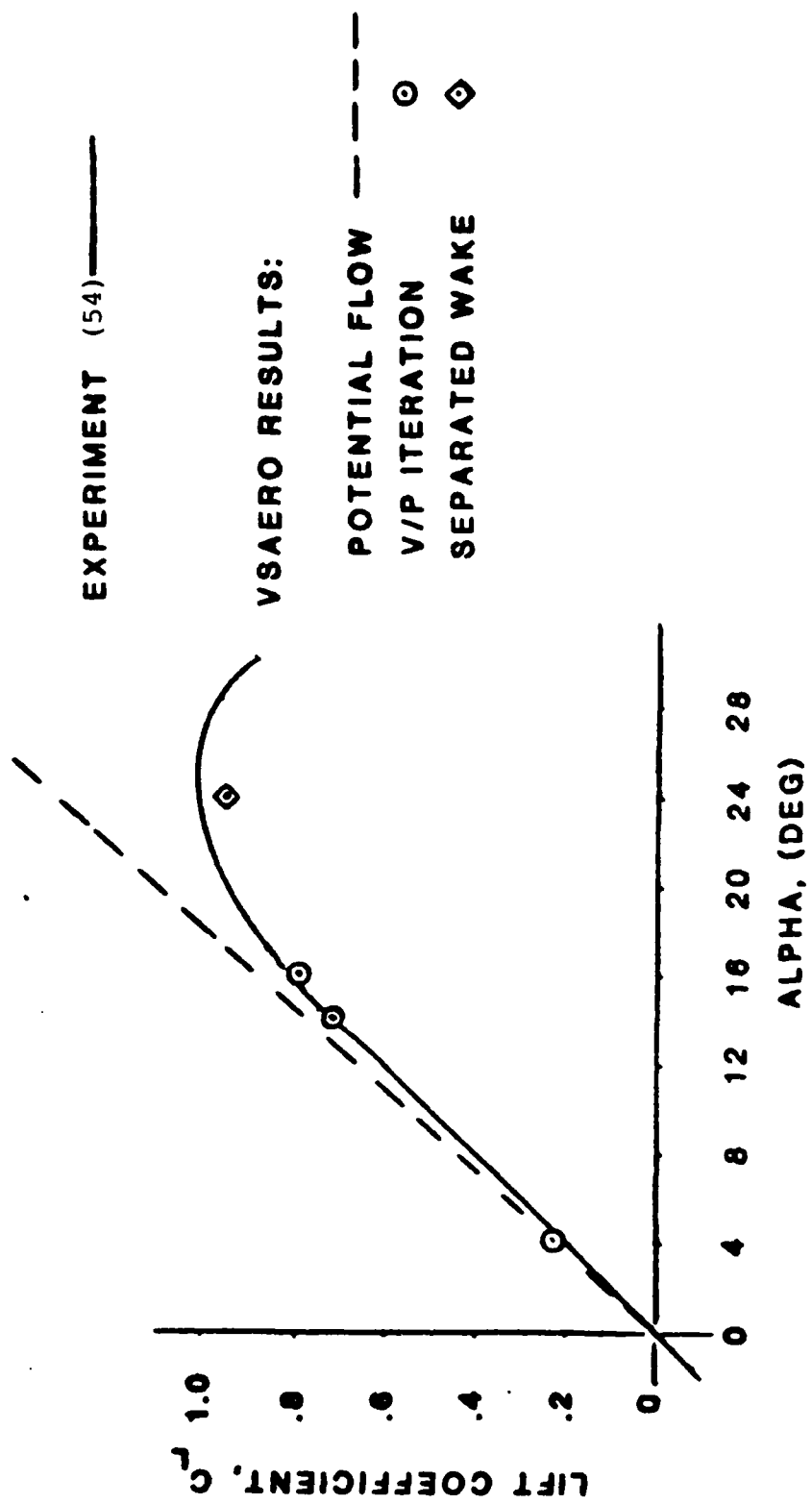


Figure 5.2.19. Low-Speed Aerodynamic Characteristics of the Kolbe and Boltz Wing;  $M = 0.25$ ,  $Re = 8$  Million.

AD-A145 107

PREDICTION OF AERODYNAMIC CHARACTERISTICS OF FIGHTER  
WINGS AT HIGH ANGLES OF ATTACK(U) ANALYTICAL METHODS  
INC REDMOND A B MASKEW ET AL. MAR 84 ARI-8485

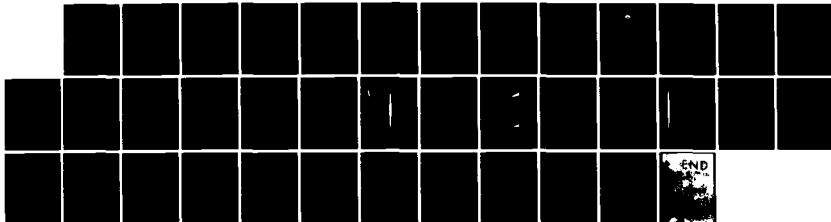
2/2

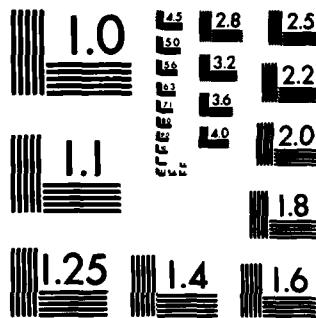
UNCLASSIFIED

N00014-82-C-0354

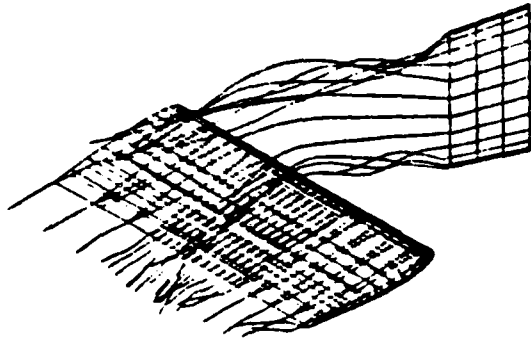
F/G 20/4

NL

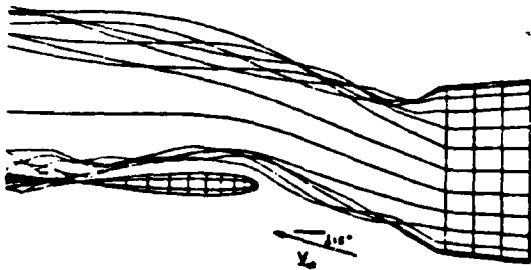




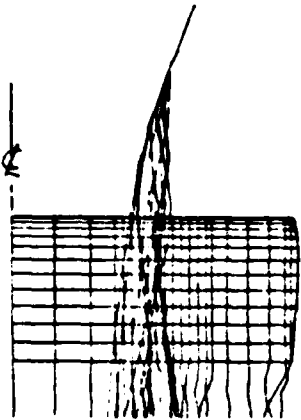
MICROCOPY RESOLUTION TEST CHART  
NATIONAL BUREAU OF STANDARDS-1963-A



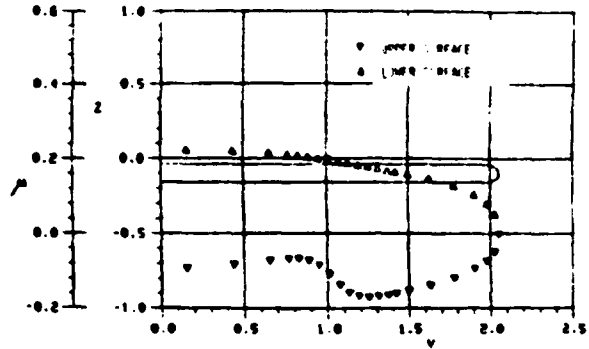
(a) General View



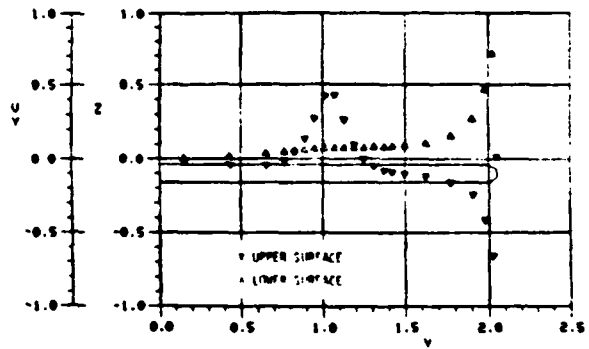
(b) Side View



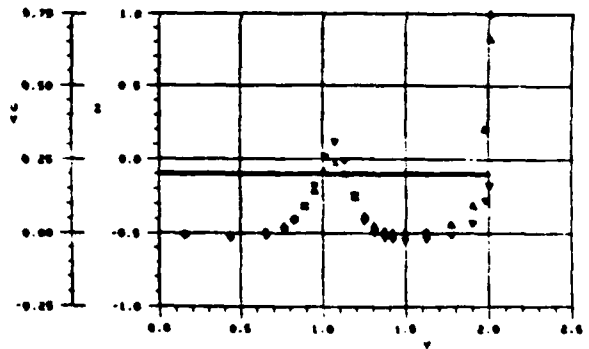
(c) Top View



(d) Spanwise Cut through the Doublet Distribution at  $x/c = .25$



$x/c = .25$



$x/c = .004$

(e) Spanwise Cuts through the  $V_y$  Distribution at  $x/c = .25$  and  $.004$

Figure 5.3.1. Calculations of a Vortex/Wing Encounter.

### 5.3 Vortex/Surface Interaction

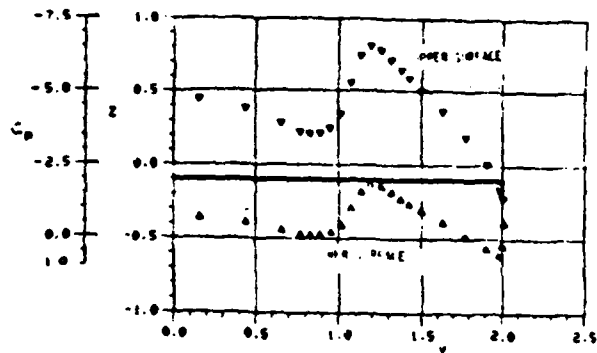
The vortical flow regions that exist near a vehicle generating lift have varying degrees of non-linear interaction with the vehicle's surface, depending on the form of the configuration. Through their effects on the integrated forces and moments, these vortical flows can strongly influence the performance and stability characteristics of a vehicle. For the most part, predicting the aerodynamic characteristics of modern high-performance vehicles requires the non-linear effects of vortical flows to be included in the modeling (e.g., see reviews in (58) and (59)).

Earlier calculations of vortex/wing interaction considered a straight onset vortex passing over a wing (e.g., (60), (61) and (62)). Patel and Hancock (61) warned of the need to complement such calculations with experimental work since the non-linear aspects of modifying the wing boundary layer and the effect of the wing on the path of the vortex were not included. The present investigation includes these aspects in the computation. Several exploratory calculations have been performed on the basic problem of a wing in the presence of an oncoming vortex wake; these calculations are of the nature of numerical experiments whose main purpose is to explore the behavior of the program. In the case discussed here, a tip vortex from an upstream wing passes close to the upper surface of a downstream wing. A general view of the configuration and vortex wake is shown in Figure 5.3.1(a) after three wake shape iterations and one viscous/potential iteration. The initial wake consisted of a set of streamwise wake lines, some of which intersected the downstream wing. The oncoming vortex system--which passes over the downstream wing at about mid-semispan--is generated by a vertical flat plate set at 20° (horizontal) angle of attack. The plate has an aspect ratio of 2.0 and a chord of .5. The tip edges are raked back at 5°. The horizontal wing has an aspect ratio of 4.0, a chord of 1.0 and a NACA 0012 section. The wing leading edge is placed at one wing chord length downstream of the plate trailing edge. The vertical plate is represented by a 3 x 12 panel array; the wing has a 24 x 20 array of panels on the main wing surface and a 3 x 12 array on the half-round tip. The complete configuration shown in Figure 5.3.1 was run with a vertical plane of symmetry at  $y = 0$  and a (vertical) angle of attack of 15°.

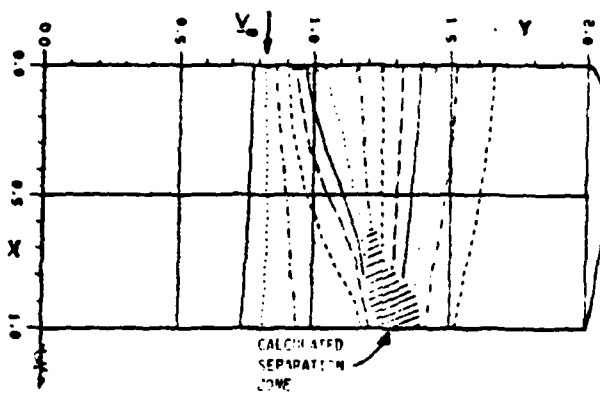
The side view of the configuration (Figure 5.3.1(b)) after the wake shape calculations shows different roll-up characteristics on the two tip vortices from the plane, which is effectively at 15° of "yaw" due to the general onset flow. The lower vortex roll-up and trajectory are clearly influenced by the presence of the wing. The general view, Figure

5.3.1(a), and the top view, Figure 5.3.1(b) show evidence of a secondary vortex roll-up in the wing wake occurring just outboard of the oncoming vortex location. This secondary vortex contains "negative" circulation induced on the wing by the oncoming vortex. The build-up towards this secondary shedding is very evident in spanwise cuts through the surface doublet (i.e., velocity potential) distribution; e.g., Figure 5.3.1(d) shows a cut at  $x/c = .25$ . The effect is clearly predominant on the upper surface where we can see the reversed doublet gradient in the vicinity of the passing vortex: the lower-surface doublet distribution has negligible local disturbance due to the vortex. It is encouraging to see such remarkably good behavior of the doublet solution especially in the vicinity of the vortex and also around the tip edge where the paneling was left very sparse.

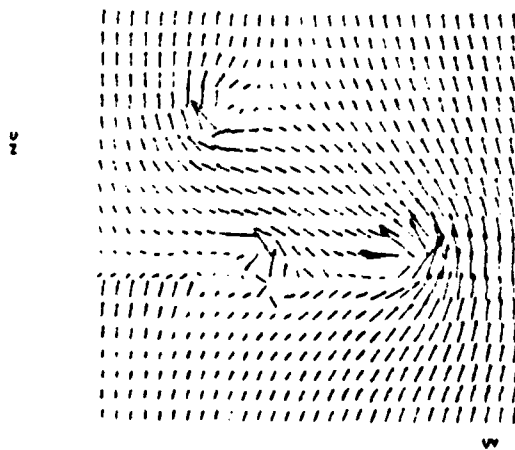
The spanwise distribution of  $V_y$ , derived from the doublet distribution in Figure 5.3.1(d), is given in Figure 5.3.1(e) for the station  $x/c = .25$ . The positive peak in  $V_y$  on the upper surface at  $y = 1.05$  stands out in contrast to the almost monotonic behavior of the lower surface  $V_y$  distribution. The latter gradually builds up in the positive spanwise sense, finally speeding up to go around the tip edge then back again (negative) on the outboard upper surface. This characteristic shows a marked rapid change in comparison with the  $V_y$  spanwise distribution near the leading edge at  $x/c = .004$ , Figure 5.3.1(e). At this station the oncoming vortex induces essentially the same (positive) spanwise flow on both upper and lower lines. Also, the differential flow pattern between upper and lower surfaces around the tip edge has not had a chance to develop at this station. The corresponding spanwise cut through the pressure distribution, Figure 5.3.1(f), shows the characteristic "upwash/downwash" effect on either side of the initial vortex encounter; this increases the suction peak on one side and suppresses it on the other. This interaction is accompanied by a differential movement of the stagnation line (or attachment line) on the lower surface as we pass through the vortex location. Further downstream the disturbance in the pressure distribution is primarily related to the positive peak in  $V_y$  on the upper surface (Figure 5.3.1(e) for  $x/c = .15$ ). The presence of this positive  $V_y$  region in what would have been a monotonic negative  $V_y$  distribution in the absence of the vortex causes two points of zero  $V_y$  to occur at stations  $y = 1.3$  and  $.72$ . The latter is a point near a line of streamline divergence; i.e., an attachment line associated with flow coming over the top of the vortex, impinging on the wing and dividing to go either inboard, or outboard back under the vortex. The outboard zero  $V_y$  station is a point near a line of streamline convergence; i.e., a line of flow departure from the surface. It is interesting to observe that this



(f) Spanwise Cut through the Pressure Distribution at  $x/c = .004$



(g) Streamlines (External) Calculated on Wing Upper Surface



(h) Velocity Survey in Cross-Flow Plane at  $x/c = 1.3$

Figure 5.3.1. Concluded.

station essentially coincides with the location of the secondary vortex observed in Figure 5.3.1.

The convergent/divergent characteristics of the local streamlines is confirmed in Figure 5.3.1(g). This shows the path of several calculated (external) upper-surface streamlines in the vicinity of the vortex. Boundary layer calculations (see later) performed along these streamlines indicate a zone of separation towards the wing trailing edge and just outboard of the vortex track.

Finally, a vertical cut through the field velocities calculated just behind the wing trailing edge at station  $x/c = 1.3$  (Figure 5.3.1(h)) shows the strong interaction vortex flows of this configuration. The wing tip vortex and the velocity shear associated with the wing wake are very evident on the right of the figure. Comparing the locations of the two vortices from the vertical, upstream plate, the lower vortex has clearly tracked outboard due to its encounter with the wing. The flow field survey was taken between spanwise stations  $y = .3$  to 2.4 (the wing semispan is 2.0).

The entire calculation described above took 430 CP seconds on a Cyber 176 computer. It involved 550 surface panels and 400 wake panels on one side of the assumed vertical plane of symmetry. Three wake shape iterations were performed with one viscous/potential iteration (i.e., a total of 4 potential flow solutions for surface velocity and pressures). Sixteen surface streamlines were calculated for the boundary layer analysis, and finally, 600 off-body points were analyzed in the cross-flow velocity survey.

The main purpose of the above calculation was to explore the behavior of the program applied to this type of problem. Following the encouraging results obtained in this and other similar calculations, correlations (63) with data from a water tunnel experiment (64) were performed.

The general layout of the model used in the water tunnel experiment is shown in Figure 5.3.2. Basically, a vertical wing with a NACA 0015 section set at  $10^\circ$  to the onset flow is placed ahead of a horizontal wing with a NACA 0012 section. The tip of the forward wing is level with the quarter-chord line of the aft wing. The forward wing has a chord of 2 inches and the aft wing, 4 inches. The distance between the two quarter-chord lines is 8 inches. The quarter-chord lines form the pivot axes for the two wings. For the calculations, the rear wing is considered at three setting angles,  $8^\circ$ ,  $12^\circ$ , and  $16^\circ$ . The rear wing is mounted between the water tunnel walls, with the tunnel 8.4 inches wide and 12 inches deep.

The Reynolds number of the flow based on the aft wing chord is 125,000.

For the present calculations, the tunnel surfaces are not panelled; instead, pseudo two-dimensional conditions are represented for the aft wing by extending its wing tips, giving an aspect ratio of about 8. The forward wing has been given a span of 12 inches so that its center section coincides with the tunnel roof location; it has 8 panels around the chord, 9 panels vertically and a 3 x 4 panel array closing the bottom tip edge. Panel size distributions are weighted towards the leading edge and towards the bottom tip edge using equal angle increments in a simple cosine formula.

The rear wing is panelled in three parts: the two parts outside the tunnel wall location each have 16 panels chordwise and 3 panels spanwise. The wing "inside" the tunnel has 32 panels chordwise with density increasing towards the leading edge. The spanwise panel arrangement has a central zone with 12 columns equally spaced and two outer zones of 3 panel columns increasing in size away from the wing center. This central piece of the wing--which corresponds with the actual wing in the experiment--was declared a separate component in the present program in order to obtain the force and moment acting on it for comparison with the experimental data.

The calculations start with the wake lines proceeding straight back parallel to the onset flow, Figure 5.3.3. This figure also shows the location of the wake-grid planes. The figure does not show the downstream part of the wake where the wake-grid planes are located at ever widening intervals. Notice that in the starting condition shown in Figure 5.3.3, the vortex lines actually pass through the aft wing. This is not a recommended practice in general, but was employed here as part of the checkout of the behavior of the calculations. This is considered further in the 12° case below.

#### Wing Alone

Preliminary runs were made with the aft wing alone at 8°, 12° and 16° angle of attack. the main objective was to make sure that the flow was essentially parallel at the tunnel wall location; however, the calculation of the basic flow condition was also of interest. The calculations included a second pass through the viscous/potential iteration cycle bringing in the effect of boundary layer displacement but not modeling separation at this time. The calculated flow conditions (upper surface) are summarized below.

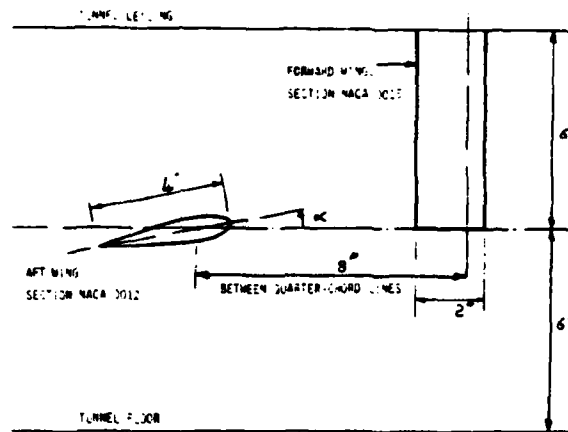


Figure 5.3.2. Layout of the Model for the Vortex/Wing Encounter.

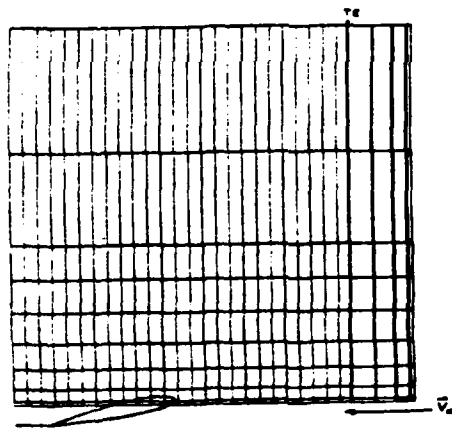


Figure 5.3.3. Starting Condition for the Wake Calculations Showing Wake-Grid Plane Locations.

- (i) 8°:- Laminar separation with turbulent reattachment occurred near the leading edge and the turbulent boundary layer remained attached back to the trailing edge.
- (ii) 12°:- Again, laminar separation with turbulent reattachment occurred near the leading edge, and turbulent separation occurred at about 85% of the chord. Normally, further viscous/potential flow iterations would be performed for this case using the separated flow model.
- (iii) 16°:- Catastrophic laminar separation occurred from near the leading edge over the full span.

As far as the extent of separation is concerned, the above results are essentially confirmed by experimental observations with the forward wing at 0° and using hydrogen bubble flow visualization. However, force and moment data (64), not shown here, indicate a significant loss in lift curve slope after about 8°. Certainly, from past experience with this type of calculation, modeling the separated flow in the 12° case would be expected to move the predicted separation forward.

#### Two Wings

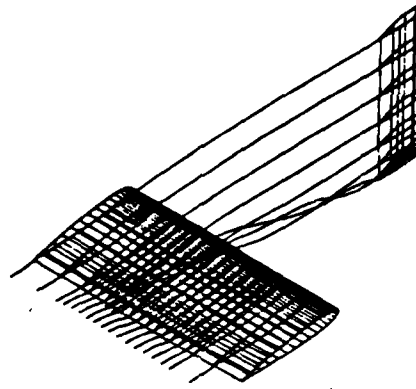
With the forward wing in place and set at 10°, the calculations were performed over three wake-shape iterations; i.e., three complete potential flow calculations were performed, the first with the prescribed wake in Figure 5.3.3 and then with two calculated shapes. (Convergence of the results will be discussed later under the 12° case.) Surface streamline and boundary layer calculations were then carried out.

A typical calculation takes about 160 CP seconds on the CRAY computer and requires 163,000 memory words; this evaluation involves a total of 756 surface panels (i.e., 756 unknowns), 33 wake columns with about 400 wake panel, 15 on-body streamlines--each with a boundary layer calculation--and 450 off-body velocity calculations.

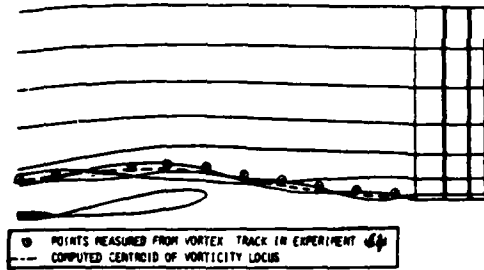
Calculations were performed for aft wing incidences of 8°, 12° and 16°.

#### Aft Wing at 8°

A general view of the final calculated wake shape for the 8° case is shown in Figure 5.3.4(a); only the "real part" of the aft wing is plotted. Figure 5.3.4(b) shows a side view of this. The computation of the roll-up of the tip vortex lines



(a) General View.



(b) Side View and Comparison with Experimental Vortex Track.

Figure 5.3.4. Final Calculated Wake Configuration for the 8° Case.

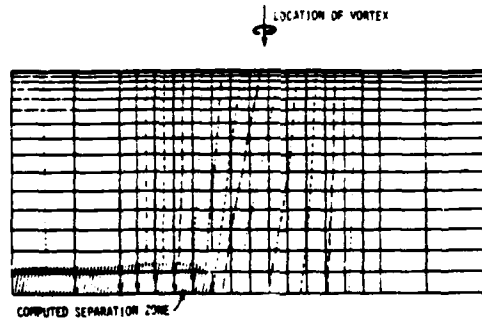


Figure 5.3.5. Plan View of the Calculated (External) Streamlines for the Aft Wing at 8° in Presence of Vortex.

is clearly affected by the presence of the aft wing; there is a tendency for the rate of roll-up to decrease in the acceleration zone ahead of the wing and then to increase again in the recovery zone towards the wing trailing edge. This behavior is very plausible and merits further investigation in the future in relation to the implied helix angle in the roll-up and the connection between this and the onset of vortex breakdown.

The dotted line in Figure 5.3.4 indicates the locus of computed centroid of vorticity for the vortex lines involved directly with the tip roll-up. This locus is in remarkably good agreement with points representing the path of the vortex core in the experiment. These points were measured from the flow field photograph (64). The small vertical shift in the vortex path is due to tip-edge separation occurring ahead of the trailing edge. This tip-edge vortex formation was not modelled in the present calculation.

After the third wake shape solution, a family of inviscid surface streamlines was calculated on the aft wing and boundary layer calculations were performed. Figure 5.3.5 shows a plan view of these streamlines, each of which is stopped at the point of calculated separation. Whereas the wing-alone case remained fully attached, we now see a region of turbulent separation on the left side of the wing brought on by the increased loading on the upwash side of the vortex. It is difficult to positively confirm this feature from the flow field photograph at this time. The thickness of the region highlighted by the bubbles and located beneath the vortex has certainly thickened slightly relative to the wing-alone case (64).

The computed force and moment coefficients for the aft wing at  $8^\circ$  are compared with experimental measurements in Figure 5.3.6 and show remarkably good agreement.

#### Aft Wing at $16^\circ$

With the aft wing set at  $16^\circ$ , the streamline/boundary layer calculations--performed after the wake-shape iterations--gave essentially the same result as for the case with wing alone; i.e., laminar separation along the entire leading edge, except in this case there was a small zone just on the downwash side of the vortex where turbulent reattachment was predicted (i.e., under the slight alleviation of the leading-edge suction peaks). However, turbulent separation occurred within 10 to 15% back from the leading edge. Although these tendencies seem plausible, such flow details have not been obtained from the experiment at this time.

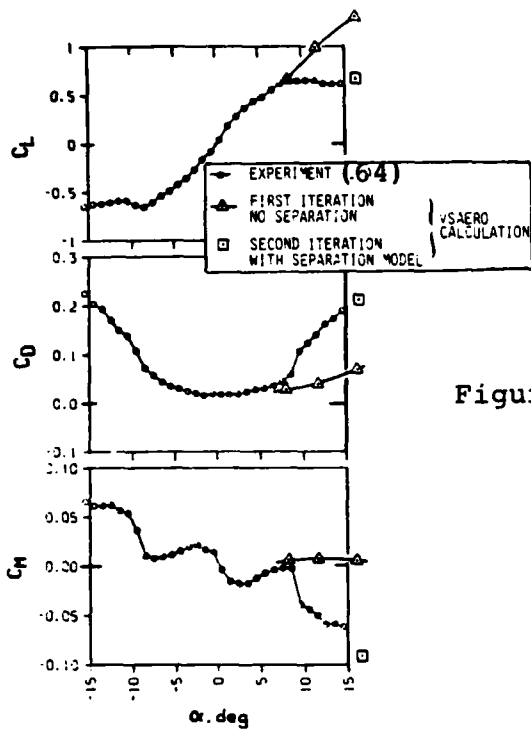
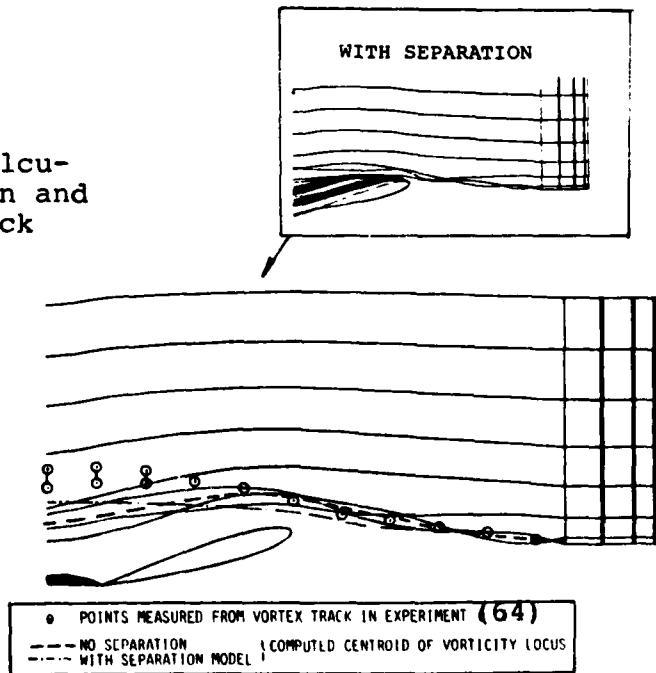


Figure 5.3.6. Comparison of Calculated and Experimental Force and Moment Coefficients in Presence of Vortex.

Figure 5.3.7. Side View of Calculated Wake Configuration and Experimental Vortex Track with Aft Wing at 16°.



The trajectories of the calculated wake lines for the above case are shown in side view in Figure 5.3.7. The locus of the calculated vorticity centroid for this initial solution follows closely the experimental vortex track ahead of the aft wing. The calculated path shows a slightly larger upswing just before the leading edge--this is consistent with the larger level of circulation, see Figure 5.3.6, in the initial calculation which has attached flow. Due to this additional circulation, the computed vorticity centroid locus is pulled quickly down over the upper surface of the wing, whereas the experimental vortex path passes more freely higher above the surface.

A second calculation was performed in which the predicted separation zone was enclosed within free vortex sheets. Initially, there was some conflict between the two wakes as they were relaxed simultaneously--the initial wake lines from the front wing (Figure 5.3.3) actually pass inside the rear separated wake. The calculated wake shape after the third solution is shown inset in Figure 5.3.7. Another pass should be performed in this case. A better approach would probably be to first relax the oncoming wake while holding the aft wing wakes rigid, then releasing the latter in the third pass. In any event, this calculation was not pursued to a complete convergence at this time. Also, there were indications (see 12° case below) that the vorticity separation model may require further ingredients for these highly three-dimensional situations where considerable vortex sheet stretching can occur.

Even though this calculation is incomplete at this stage, the track of the calculated vorticity centroid shows a plausible change relative to the attached flow solution, showing a smaller upswing ahead of the wing leading edge and passing more freely above the wing. In fact, the track over the wing now runs approximately parallel to the experimental vortex path except it is too low. The reason for the latter discrepancy is not clear at this stage, especially since the computed lift coefficient--and also the drag coefficient--are now in close agreement with the experimental measurements, Figure 5.3.6. The pitching moment coefficient also is in reasonably good agreement with the experiment. All three quantities show quite large changes due to including the separation model.

#### Aft Wing at 12°

The convergence of the wake-relaxation iteration was examined for the 12° case. Figure 5.3.8 compares the computed wake-line shapes for the second and third wake solutions. The recovery from the initial "bad" setup (Figure 5.3.3) is

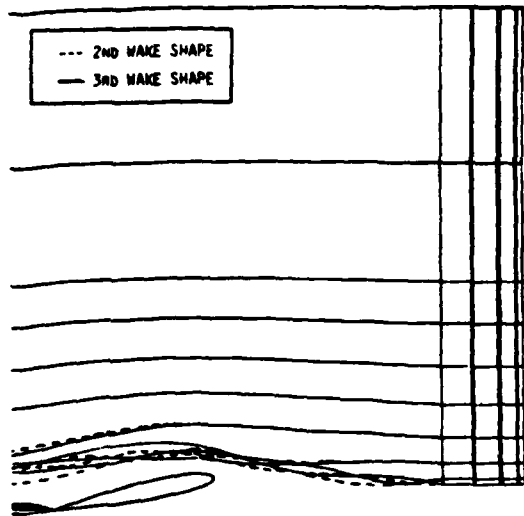


Figure 5.3.8. Comparison of Second and Third Calculated Wake Shapes for Aft Wing at 12°.

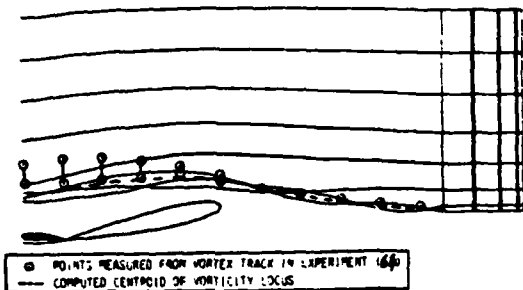


Figure 5.3.9. Comparison of Computed Wake and Experimental Vortex Track for Aft Wing at 12°.

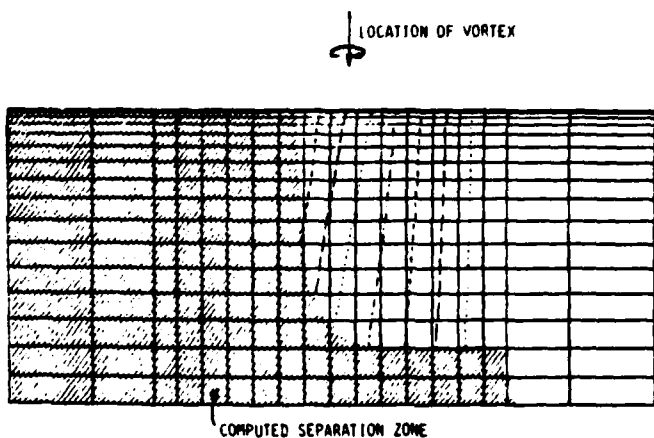


Figure 5.3.10. Top View of Calculated Surface Streamlines on Aft Wing at 12° in Presence of Vortex and Showing Calculated Separation Zone (First Iteration).

clearly very rapid for the basic attached flow case. Also, there is very little change in the geometry between the second and third wakes. Comparisons of wing pressure distributions (not shown here) also confirm the convergence of the solution.

The calculated locus of vorticity centroid for the tip vortex lines is in remarkably good agreement, Figure 5.3.9, with the track of the experimental vortex. As it passes over the aft wing, the latter appears to cover a wider zone than was the case at  $8^\circ$  and  $16^\circ$ ; real-time observation in the experiment suggests an unsteadiness in the vortex path rather than a broader vortical region (64). The calculated vorticity locus seems to favor the lower edge of the region--this would be consistent with the fully attached assumption of the calculation and perhaps an intermittent separation in the experiment caused by the mutual interaction between the vortex path and the extent of separation; i.e., a low vortex path may induce separation causing the vortex to move up, at which time the decreased interaction may allow a reattachment or at least a reduced extent of separation--and this would bring the vortex back down again.

The streamline/boundary layer calculations for the  $12^\circ$  case do, in fact, indicate an interesting situation, Figure 5.3.10. The calculations predict a catastrophic laminar separation from the leading edge over the entire upwash side of the oncoming vortex; elsewhere, the laminar separation is followed by turbulent reattachment and eventual separation occurs well back on the upper surface. The present upwash-side separation is clearly vortex induced.

These calculations, of course, represent the first pass of an iterative solution; i.e., the separation has not been modelled at this stage. Attempts at modeling the part-span separation have so far met with mixed success. Certainly, section lift, drag and pitching moment calculated at sections both on the upwash and on the downwash side of the vortex have values closely related to the total experimental values; however, in the region of the predicted edge of the part-span separation, the interaction between the onset vortex and the "end" of the separation model are clearly very strong.

Modeling these part-span separations, which involve strong vortical flow action, clearly requires further development. Further information on the actual vortical flow pattern in the experiment, including surface flow visualization and pressures, would be very helpful to any modeling improvements.

## 5.4 Leading-Edge Vortex Flows

### 5.4.1 Delta Wing

When applied to a unit aspect-ratio delta wing at  $20^\circ$  angle of attack, VORSEP generates the smooth wake spiral shown in Figure 5.4.1. If we compare the position of the vortex core to experimental measurement (65), we find that its vertical position, Figure 5.4.2, is predicted well by VORSEP. For a conical geometry, VORSEP will show a nearly linear increase in height with distance downstream; any non-linearity is due to the amalgamation scheme and initial transients from starting at a finite distance from the apex. In this case, where the wing has a biconvex airfoil section, the vortex height tends to increase more rapidly near the nose, and less so near the trailing edge. The discrepancy between VORSEP and experiment at the trailing edge is mainly due to the three-dimensional quality of the flow in which the core begins to parallel the free stream as it approaches the trailing edge. In plan view, Figure 5.4.3, the predictions are markedly more outboard than the experiment.

Using the aforementioned wake tracking scheme, the trajectories of the wake filaments attached to the leading edge were constructed and shown in Figure 5.4.4. It should be noted that all the filaments are well behaved in that they leave the leading edge at approximately the same angle and wind about the core evenly. The noticeable kinks in each filament occur at the grid planes which divide each wake strip into panels.

The pressure distributions obtained from VSAERO are shown in Figure 5.4.5. The upper surface distribution at 30% of root chord compares favorably to Smith's (65) conical flow theory or experiment inboard of the secondary separation line. The other upper surface pressure peaks are too narrow and further outboard than experiment. The lower surface pressures at 70 and 90% root chord do not approach the upper surface pressures at the leading edge but behave somewhat like the pressures found in attached flow.

### 5.4.2 Swept Wing with Strake

To investigate the utility of VORSEP for a more complex planform, wake structures were generated over a swept wing with strake. The wing modelled was used by White et al. in wind tunnel tests during an investigation of vortex flow control for high-lift generation (8). The planform is best described by Figure 5.4.6. Basically, the wing is made of a sharp-edged strake with  $57^\circ$  leading-edge sweep attached to a tapered wing with  $50^\circ$  leading-edge sweep. During the experiment various devices were attached to the wing including a

STATION 67.10

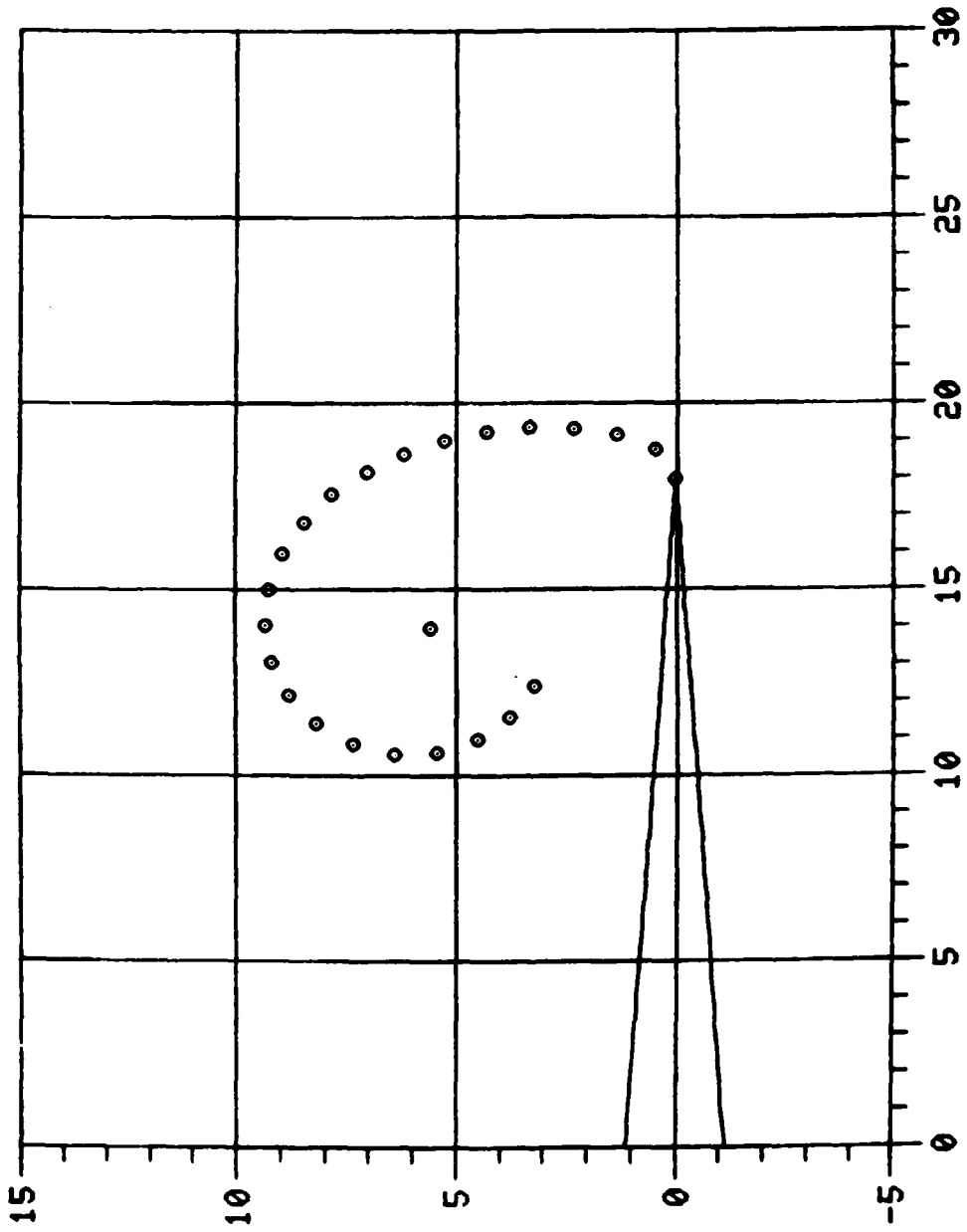


Figure 5.4.1. Delta Wing Leading-edge Vortex Shape.

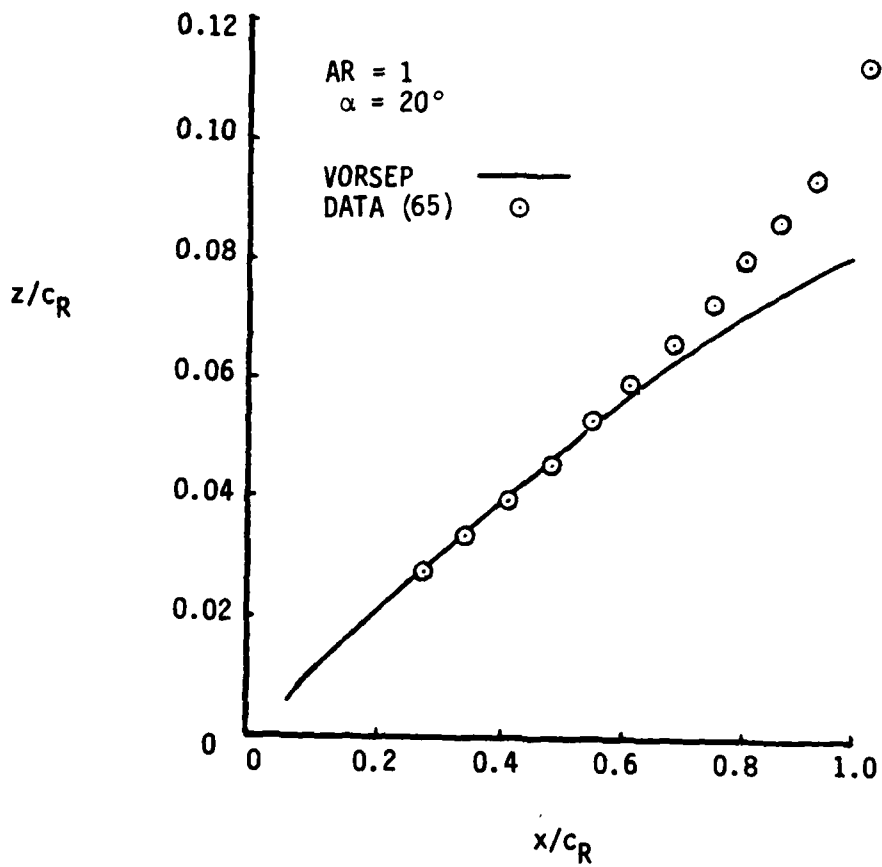


Figure 5.4.2. Predicted and Observed Elevation of Vortex Core over Delta Wing.

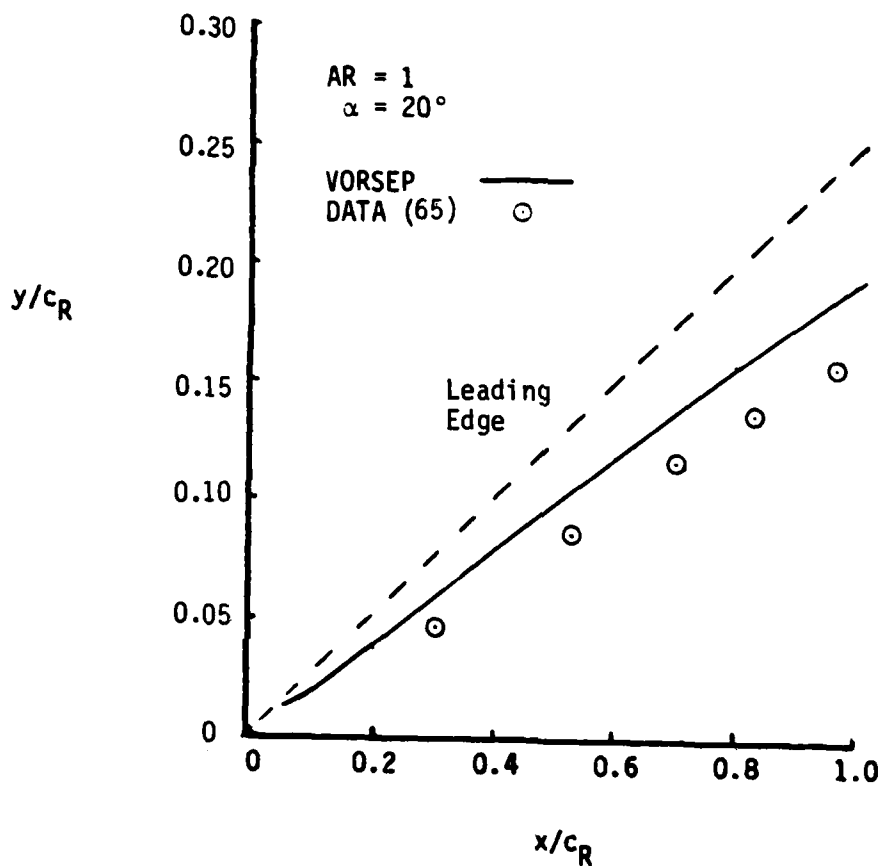


Figure 5.4.3. Predicted and Observed Span Position of Vortex Core over Delta Wing.

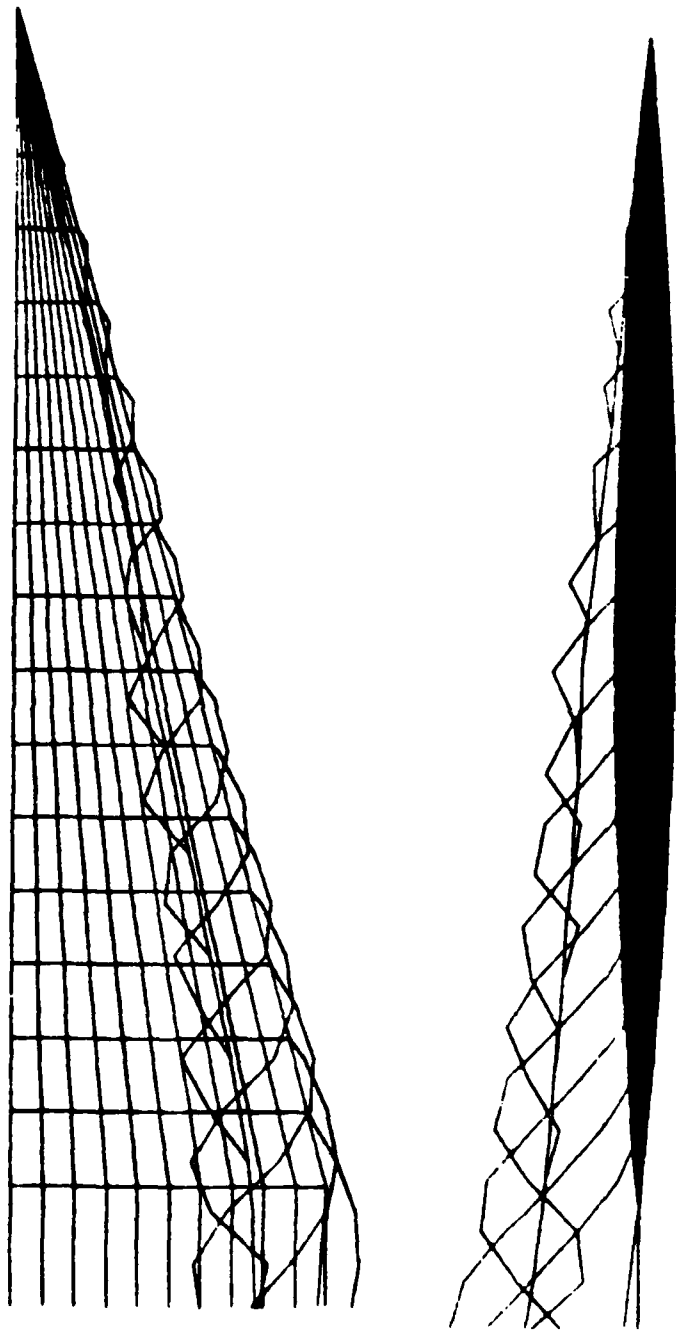


Figure 5.4.4. Delta Wing with VORSEP-Generated Leading-Edge Wake.

Symbol	$x/c_R$
○	0.3
□	0.5
▽	0.7
◇	0.9

AR = 1  
 $\alpha = 20^\circ$

--- Smith (66)  
 -.- Jones (48)

VSAERO

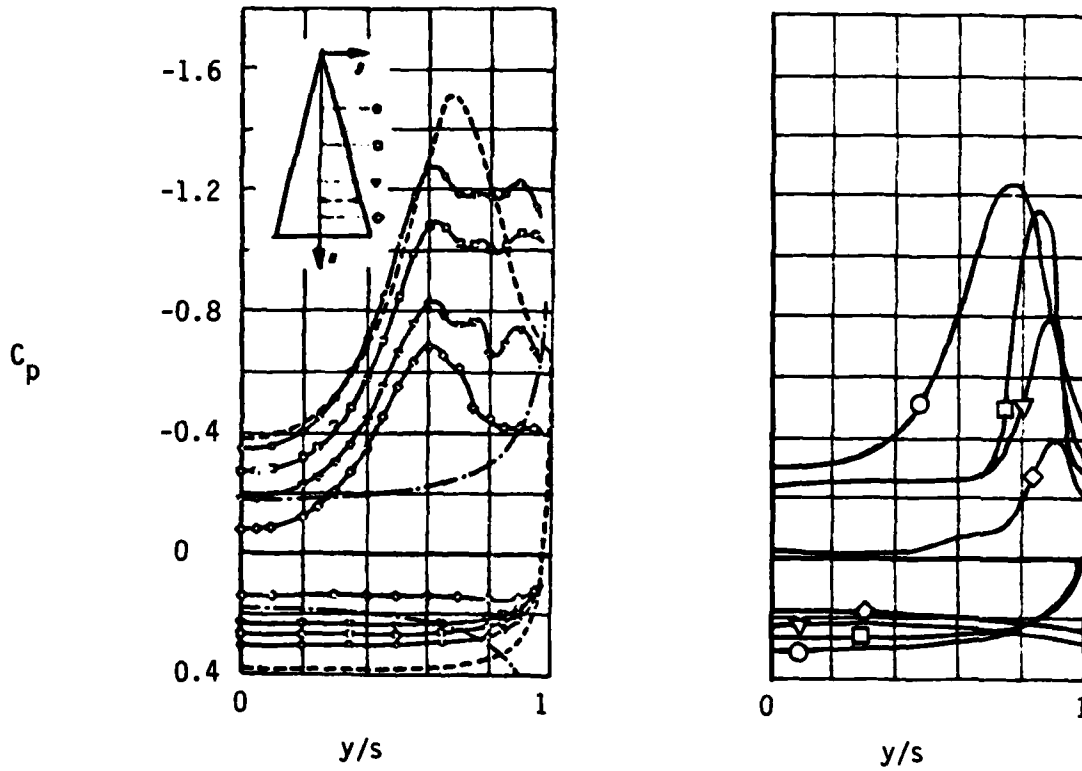
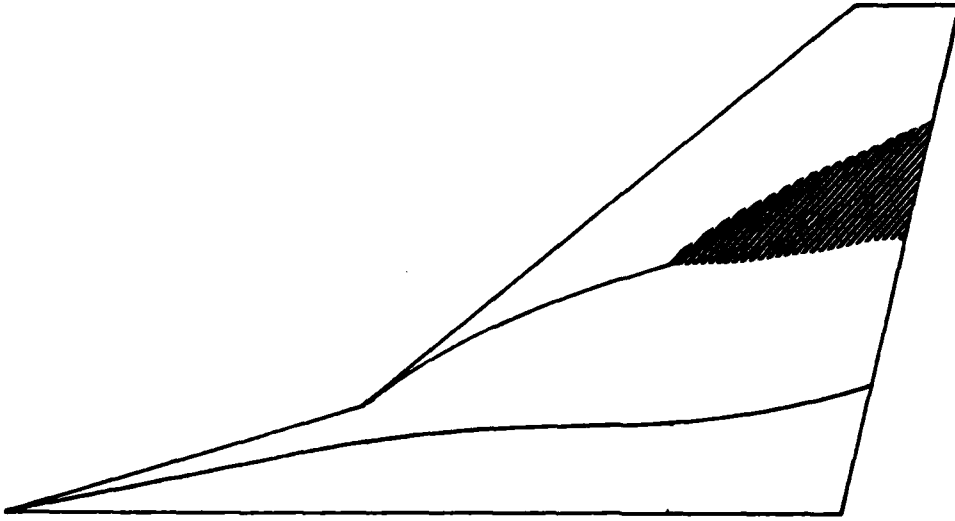
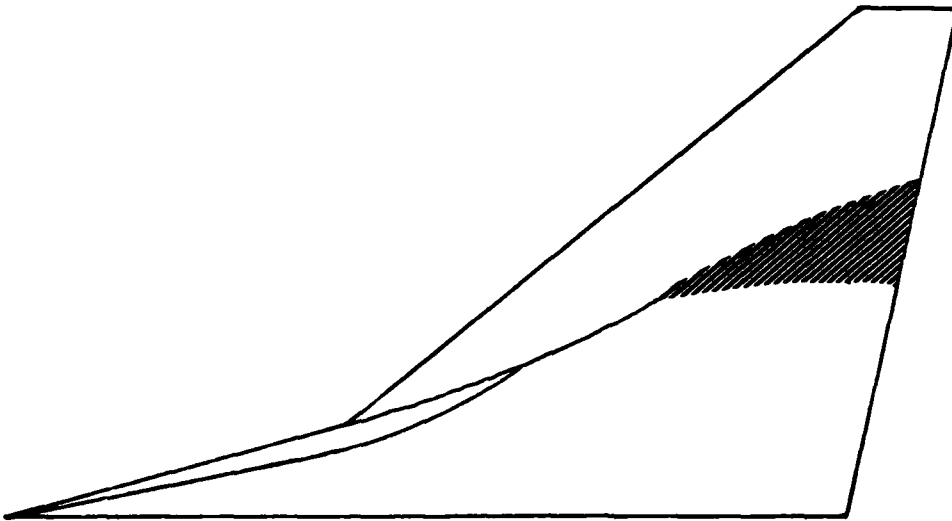


Figure 5.4.5. Comparison of VSAERO Pressure Distribution on Delta Wing with Experiment.



CONFIGURATION 3A



CONFIGURATION 6

Figure 5.4.6. Experimentally Observed Vortex Core Behavior over Straked Wing.

separator plate which changed the rounded leading edge of configuration 3A into the sharp edge of configuration 6.

At low angles of attack the vorticity shed by the strake and wing rolls up into two distinct vortex cores. At higher angles of attack when the vortices are stronger, these two cores intertwine just downstream of the strake/wing juncture, forming one vortex core. This behavior is influenced not only by the angle of attack but also by the leading-edge shape which affects the amount of vorticity shed into the wake. Experimental observations at the same angle of attack show that the vortices over the sharp-edged configuration 6 intertwine at much lower angles of attack as shown in Figure 5.4.7. Also shown is the position of the vortex bursts.

The purpose of this review is to point out the salient features of the wake over the straked wing. This is important in considering how VORSEP will model the wake, because, for the present, each wake model in VORSEP allows for only one vortex core.

If the wake is modelled with one wake in VORSEP, then the resulting structure at an angle of attack of  $20^\circ$  is shown in Figure 5.4.8. The single-wake model has biased the solution towards combining all the vorticity into one core. The path of the vortex core is not unlike that seen over configuration 6. The vorticity shed near the trailing edge is higher in VORSEP, so the core is further outboard than experiment.

If we decide to allow more detail in the wing wake by modeling it as a second wake in VORSEP, Figure 5.4.9, then the wake structure appears more like that found on configuration 3A. In fact, it appears remarkably close to the wake found at a slightly higher angle of attack,  $26^\circ$ . If less vorticity had been shed into the wake, the strake vortex would remain separate from the wing vortex.

The second wake structure was chosen to couple VORSEP with VSAERO. The pressure distributions predicted by VSAERO at 10, 30, 50 and 90% local wing chord are shown in Figures 5.4.9(a) through 5.4.9(d). At 10% local chord, the predicted pressure distribution agrees very well with experiment in the position of the pressure peaks under the strake and wing vortices. The prediction is markedly higher under the wing vortex. At 30 and 50% chord, the prediction continues to show a separate pressure peak under the strake vortex as does experiment, but qualitatively the pressures are too high. Also, the leading-edge pressures indicate the flow is not leaving the wing smoothly. At 90% chord, the strake vortex is predicted to have merged with the wing vortex so no separate peak is predicted, while a slight peak can be seen in experiment. The

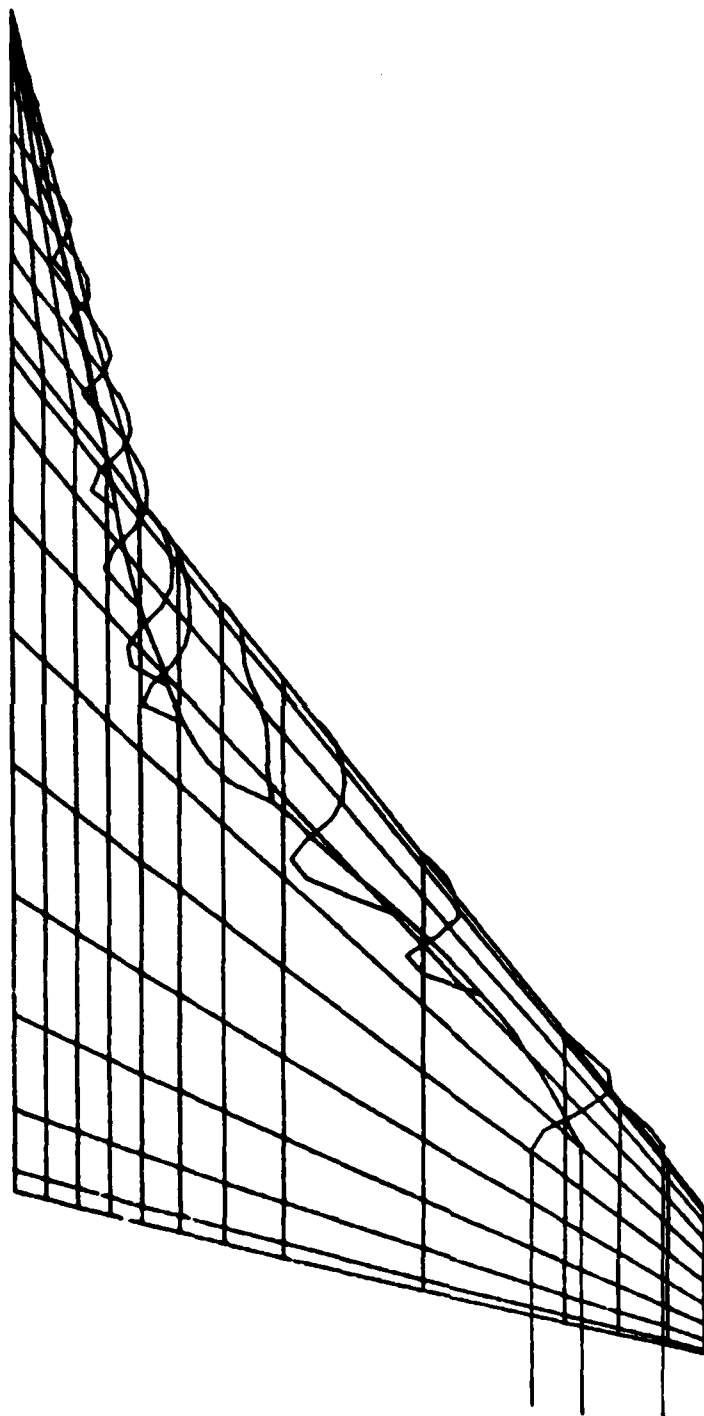


Figure 5.4.7.

SINGLE-WAKE MODEL OF LEADING-EDGE SEPARATION OVER STRAKED WING  
XVUE= 0.00    YVUE= 100.00    ZVUE=0.14E+08

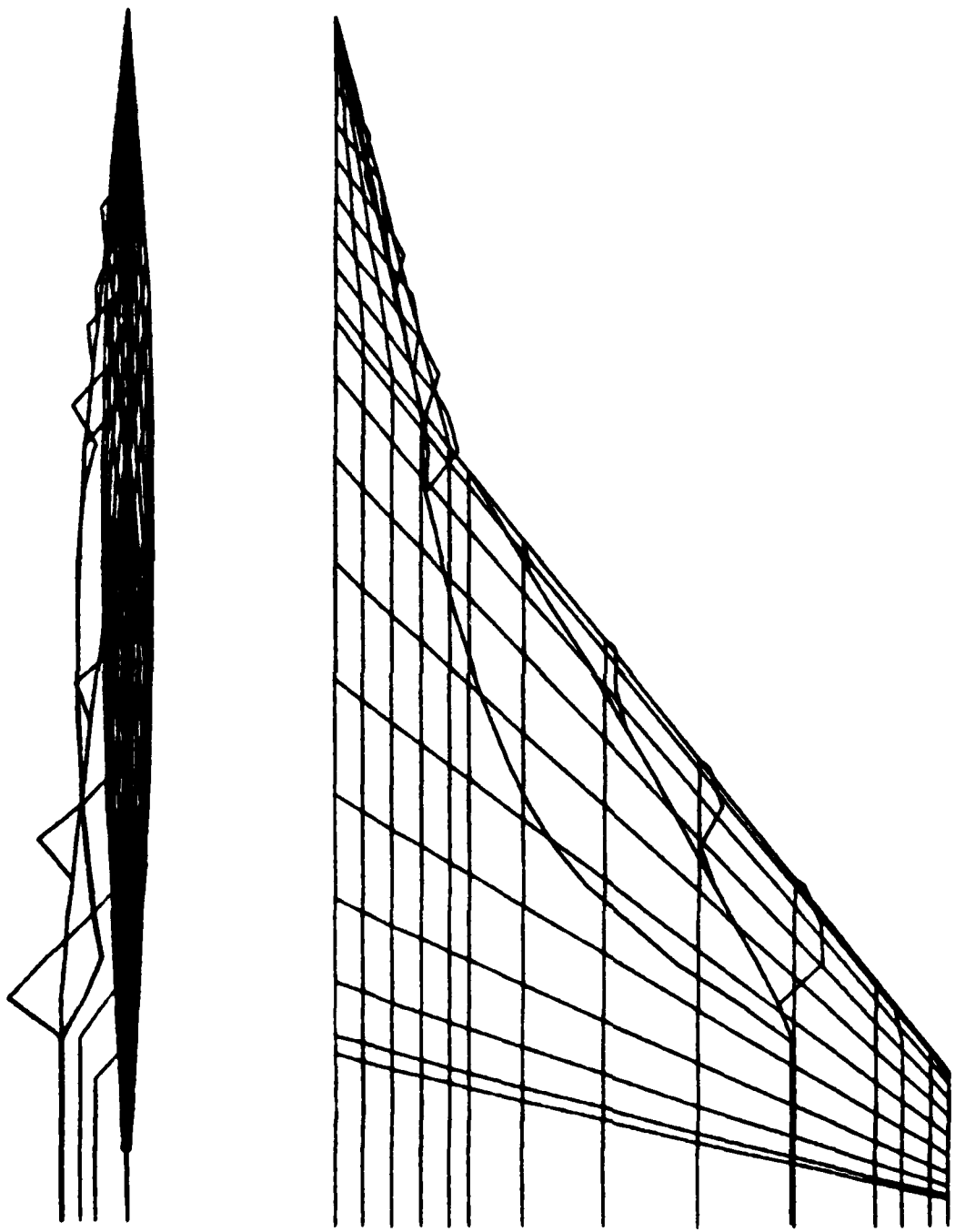


Figure 5.4.8. VORSEP-Generated Wake over Straked Wing.

AERODYNAMICS DATA

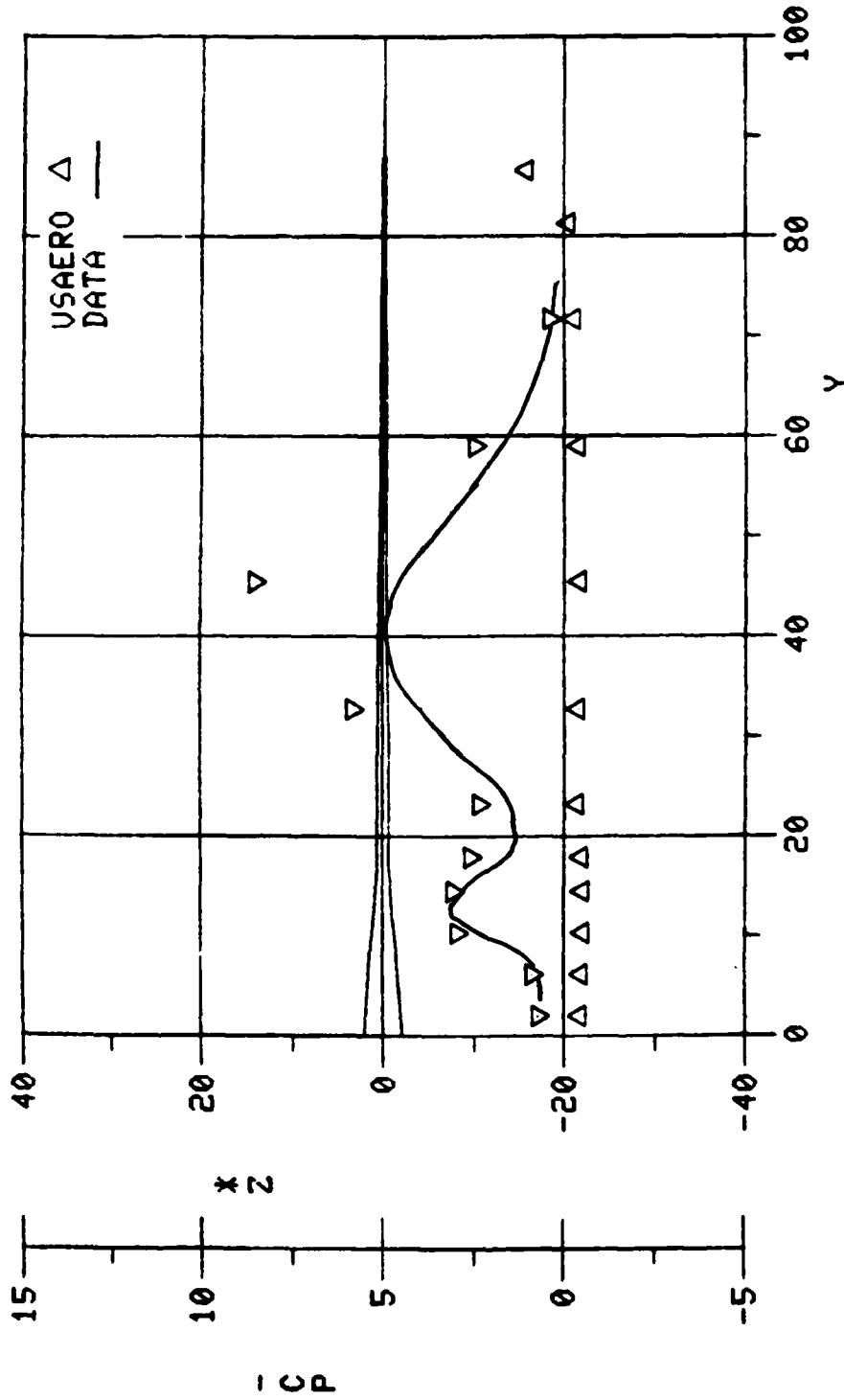


Figure 5.4.9(a).

STRAKED WING WITH VORSEP-GENERATED WAKE

\* YAWED STATION CUT X,Y,BETA 33.85 0.00 49.07

AERODYNAMICS DATA

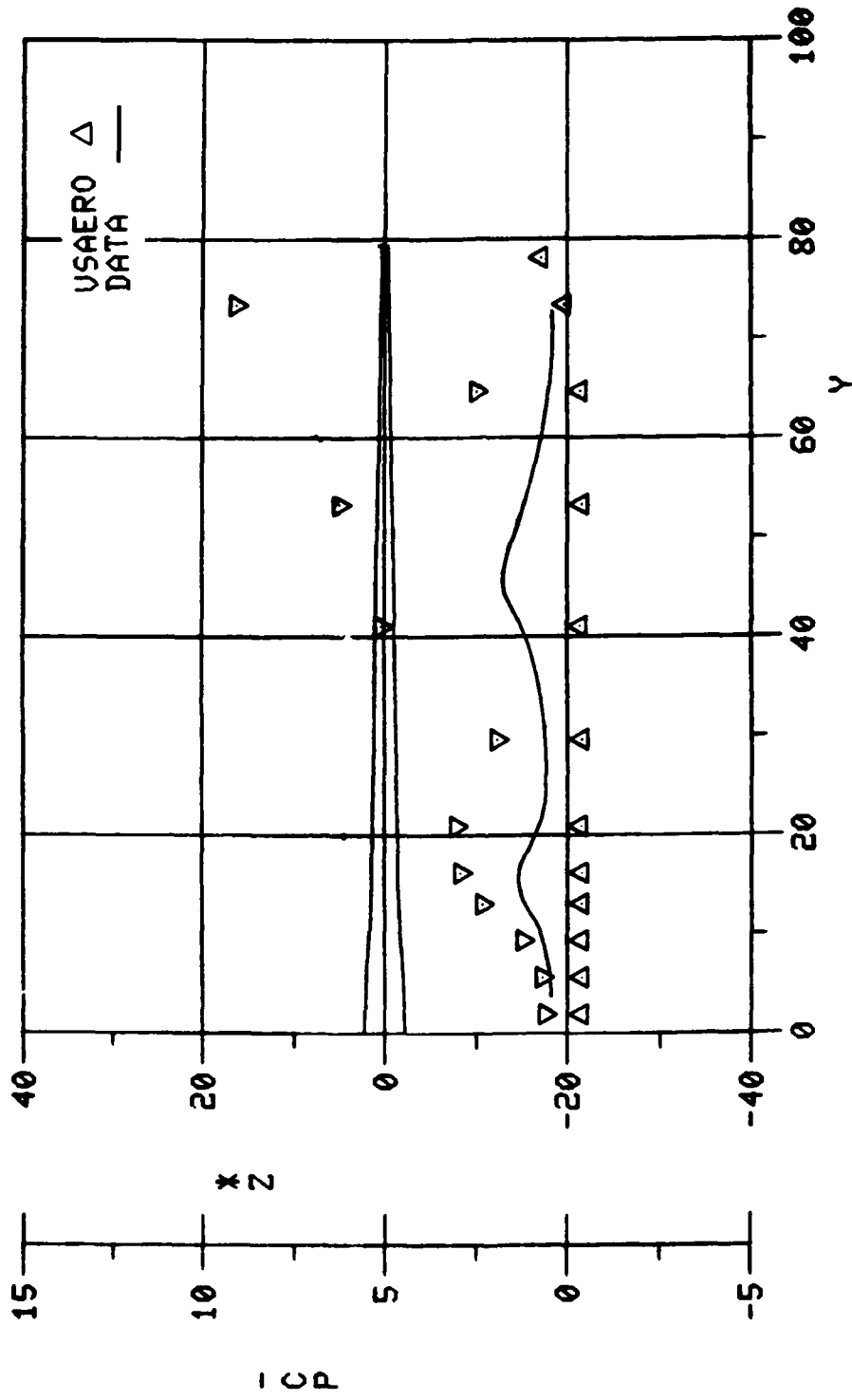


Figure 5.4.9(b).

STRAKED WING WITH VORSEP-GENERATED WAKE

X YAWED STATION CUT X, Y, BETA 47.95 0.00 43.50

AERODYNAMICS DATA

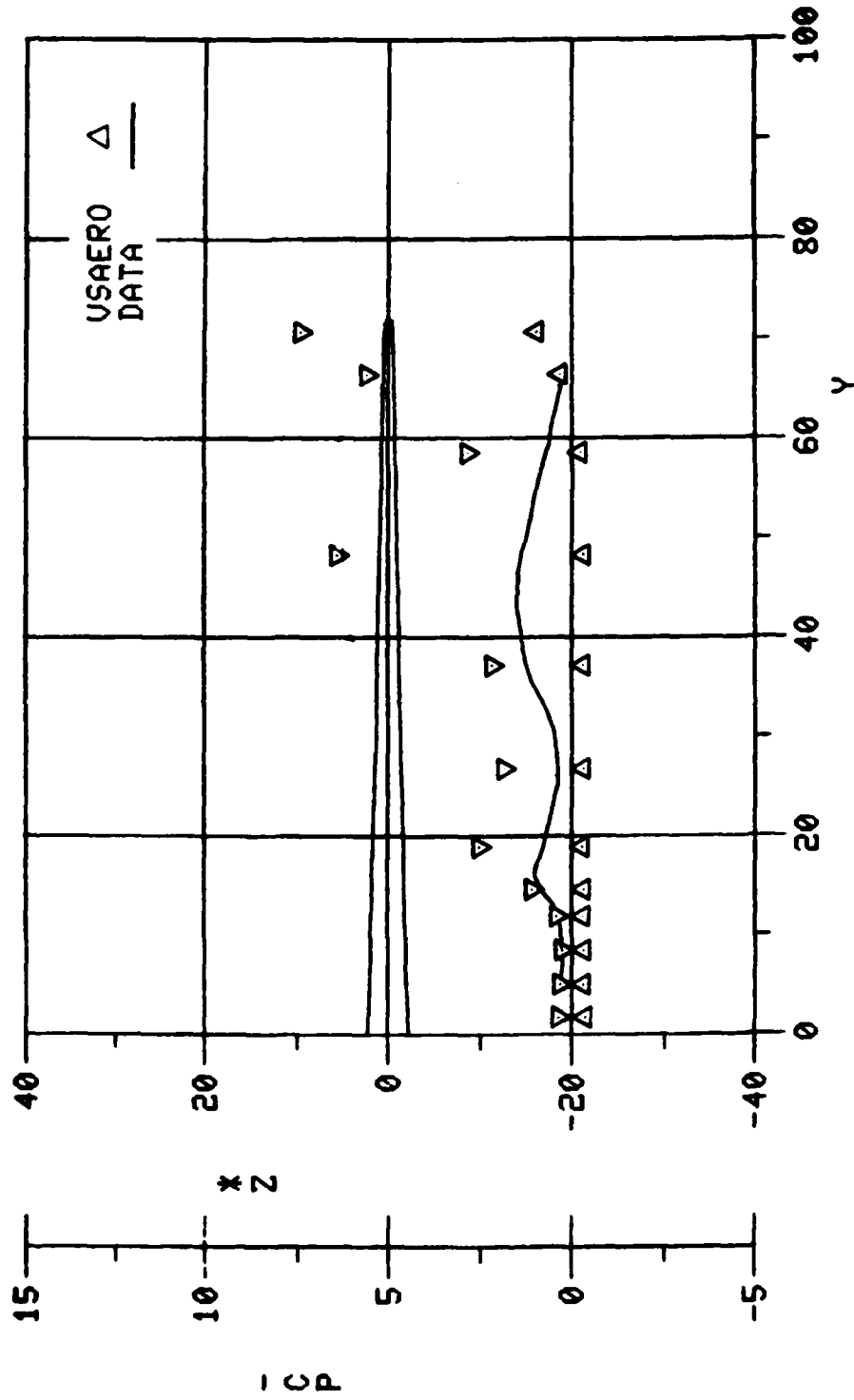


Figure 5.4.9(c).

STRAKED WING WITH VORSEP-GENERATED WAKE

\* YAWED STATION CUT X, Y, BETA 62.05 0.00 36.70

AERODYNAMICS DATA

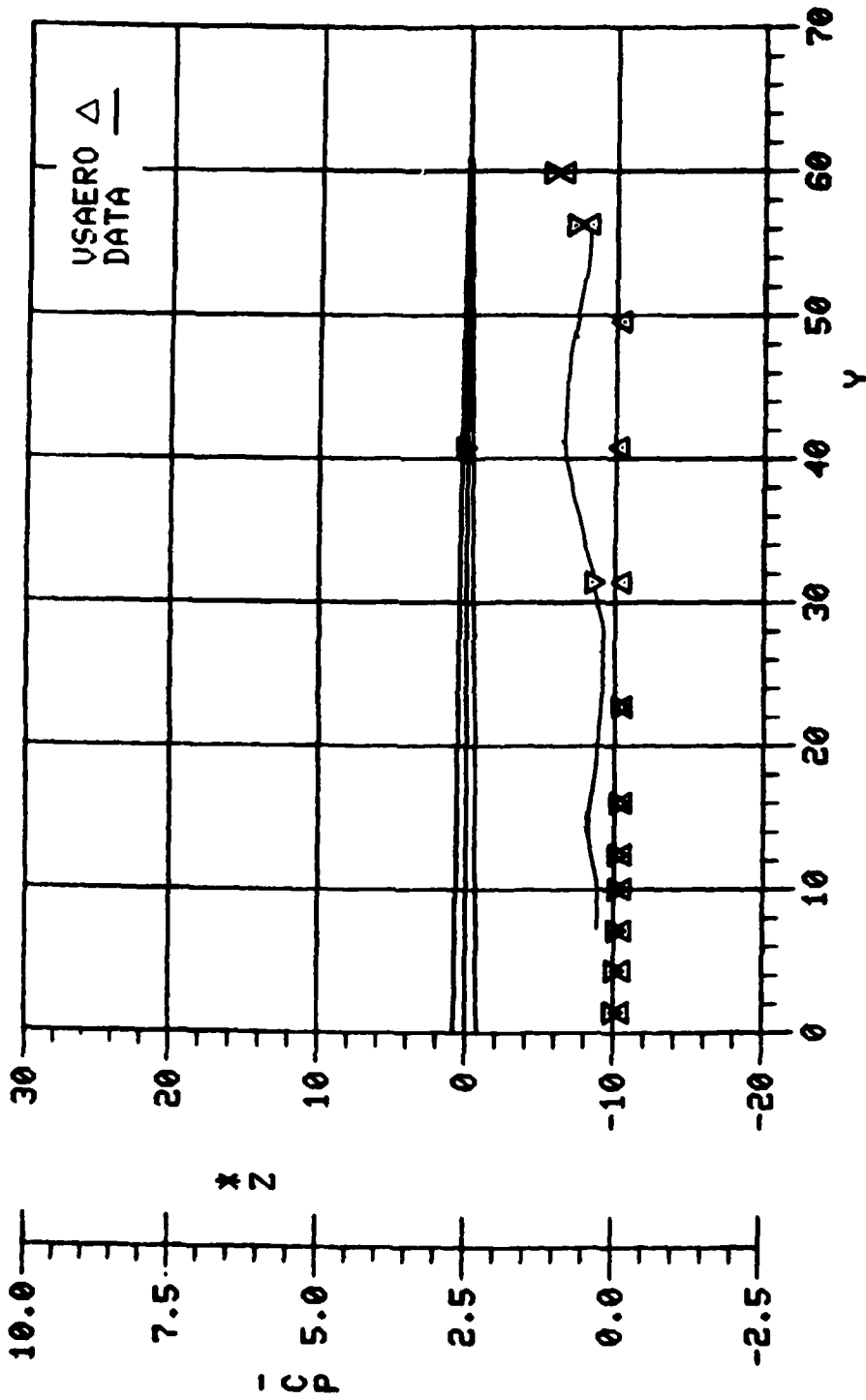


Figure 5.4.9 (d).

STRAKED WING WITH VORSEP-GENERATED WAKE  
 \* YAWED STATION CUT X,Y,BETA 90.25 0.00 18.70

pressure under the wing vortex is again too high, but elsewhere the loading is obviously approaching zero near the trailing edge and the leading edge. The trailing-edge loading under the wing vortex is high because the trailing vorticity streams straight back instead of flowing spanwise under the influence of the leading-edge vortex. This violation of the Kutta condition has been observed by other researchers. Once the trailing-edge wake is relaxed this peak should be reduced.

The results are quite encouraging considering this is the first time VSAERO and VORSEP have been coupled. Qualitatively they show the presence of two pressure peaks over most of the body caused by the strake and wing vortices. Quantitatively, the peaks are consistently high.

To investigate the cause of this the wake circulation as a function of wing root chord is plotted in Figure 5.4.10. This is compared to the circulation calculated by VORSEP. It is apparent that over the strake, where the low-aspect ratio assumption of VORSEP is observed, VSAERO agrees remarkably closely with VORSEP. This is true even if the wake in VSAERO is from the strake only and attached flow is assumed over the wing. However, over the main wing the circulation is markedly higher than that calculated by VORSEP.

Slightly better agreement would be obtained if only the streamwise circulation in VSAERO were plotted, but the 15% difference would not substantially decrease the strength of the wing vortex which, near the strake/wing juncture, is twice that predicted by VORSEP. Reducing the vorticity (the slope of the circulation curve) would reduce the wing vortex strength, and, hence, the pressures under the core, leading to better correlation between VSAERO and experiment.

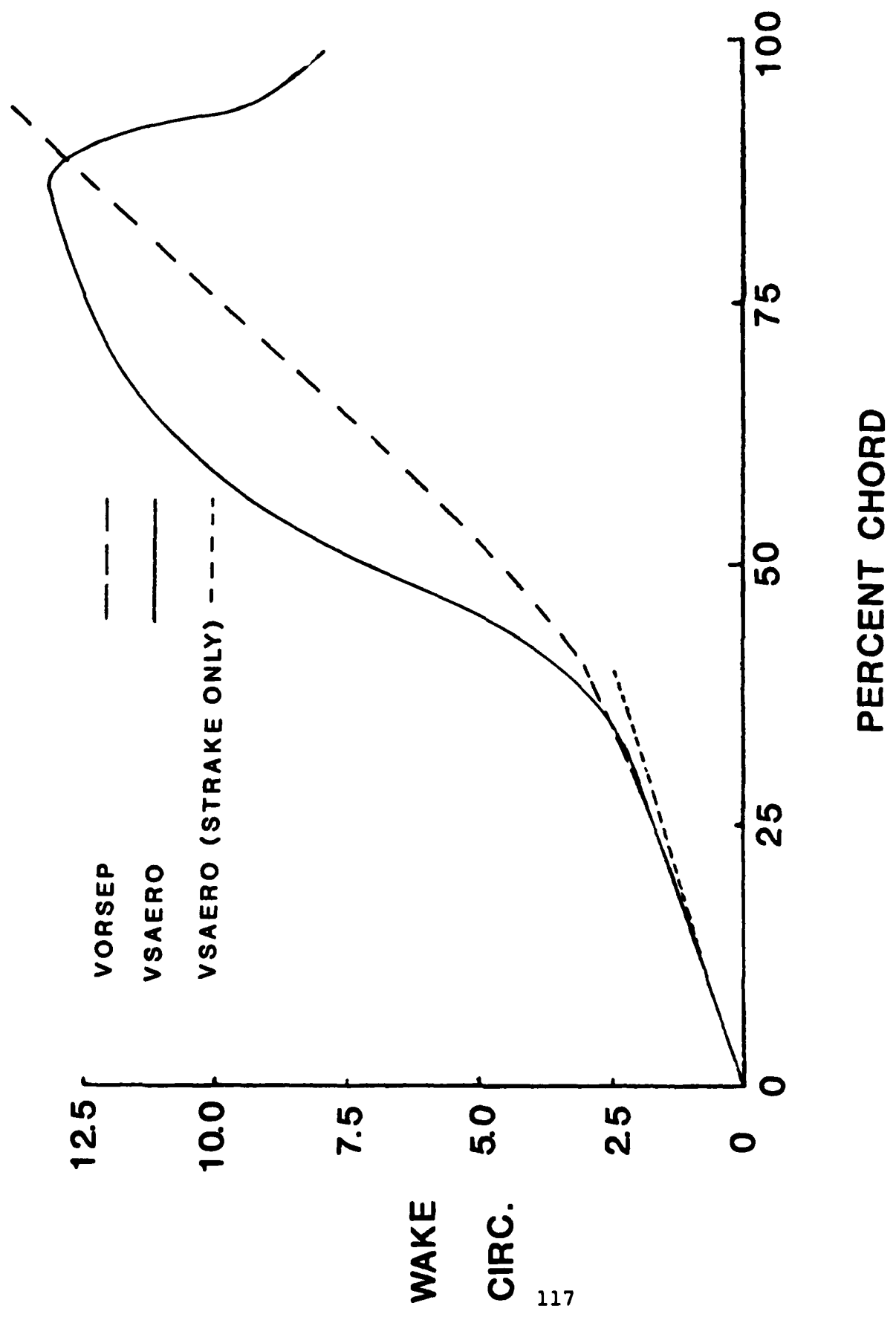


Figure 5.4.10. Comparison of VORSEP and VSAERO Vortex Circulation.

## 6.0 CONCLUSIONS AND RECOMMENDATIONS

The flow characteristics of fighter wings at large angles of attack are undoubtedly very complex. The present investigation has examined modeling techniques for such flows based on a surface singularity panel method coupled with iterative routines for wake location, viscous effects and vortex flows. Applications of the techniques to a number of configurations having separated flows have shown encouraging results and are very economical in computing effort. Separations that are essentially of a two-dimensional nature, i.e., small amounts of cross flow inside the separated zone, appear to be treated very well, with good prediction of separated zone pressures. When the separation becomes highly three-dimensional as in the case of strong vortex/surface interactions, the procedure has had mixed success. Further development of the model for the vortical-flow dominated separations is recommended. Experimental data, complete with flow-field information as well as surface oil flow and pressures, is desirable to help with this development. Also, the wide range of data on the Kolbe and Boltz wing should be used for further correlational studies.

The results of Section 5.4 indicate that the unsteady cross-flow program, VORSEP, can reproduce physically realistic three-dimensional wake structures for use in VSAERO. The pressure predictions of VSAERO show that the VORSEP wakes would be suitable starting points for wake relaxation although a converged wake shape from VSAERO was not obtained. It is therefore recommended that improvements to the wake relaxation scheme, such as those of Rao and Nathman (67) be incorporated in VSAERO. Calculations over the straked wing illustrate the need for a multiple-core wake model to avoid the question of how best to represent a continuous separation with multiple vortices. The extra data required for the VORSEP calculations is minimal, a sign that savings in labor and computer resources can be achieved.

## 7.0 REFERENCES

1. Rao, B.M., Maskew, B. and Dvorak, F.A., "Prediction of Aerodynamic Characteristics of Fighter Wings at High Lift", ONR Report CR-215-258-1, July 1979.
2. Dvorak, F.A., Maskew, B. and Woodward, F.A., "Investigation of Three-Dimensional Flow Separation on Fuselage Configurations", U.S. Army USAAMRDL Report TR-77-4, March 1977.
3. Dvorak, F.A., Woodward, F.A. and Maskew, B., "A Three-Dimensional Viscous/Potential Flow Interaction Analysis Method for Multi-Element Wings", NASA CR-152012, July 1977.
4. Maskew, B. and Dvorak, F.A., "The Prediction of  $C_{l_{max}}$  using a Separated Flow Model", J. Am. Hel. Soc., April 1978.
5. Dvorak, F.A., Maskew, B. and Rao, B.M., "An Investigation of Separation Models for the Prediction of  $C_{l_{max}}$ ", Final Technical Report, Prepared for U.S. Army Research Office, Research Triangle Park, N.C., 1976-1979.
6. "VSAERO, A Computer Program for Predicting the Non-linear Aerodynamic Characteristics of Arbitrary Configurations--Theory Document", To be published as a NASA CR.
7. Winkleman, A.E., "Flow Field Surveys of Separated Flow on a Rectangular Planform Wing", Paper 81-0255, Presented at AIAA 19th Aerospace Sciences Meeting, St. Louis, MO, January 1981.
8. White, R.P., Gangwani, S.T. and Balcerak, J.C., "A Theoretical and Experimental Investigation of Vortex Flow Control for High Lift Generation", Office of Naval Research Report ONR-CR-212-223-3, December 1976.
9. Brennenstuhl, U. and Hummel, D., "Vortex Formation over Double-delta Wings", ICAS Paper 82-6.6.3, 1982.
10. Blascovich, J.D., "Characteristics of Separated Flow Airfoil Analysis Methods", Grumman Aerospace Corporation Report, January 1983.
11. Dvorak, F.A. and Maskew, B., "The Modelling of Airfoil Separation in Subsonic and Transonic Flow", Paper No. 1 in Viscous and Interacting Flow Field Effects, Proc. 5th U.S. Air Force and Federal Republic of Germany Data Exchange Agreement Meeting, AFWAL-TR-80-3088, June 1980, pp. 1-22.

12. Rao, B.M., Dvorak, F.A. and Maskew, B., "An Analysis Method for Multi-Component Airfoils in Separated Flow", NASA CR-159300, August 1980.
13. Maskew, B. and Dvorak, F.A., "Prediction of Dynamic Stall Characteristics using Advanced Non-linear Panel Methods", Paper Presented at AFOSR/FJSRL Workshop on Unsteady Separated Flows, USAF Academy, Colorado Springs, CO, August 1983.
14. Jacob, K., "Advancement of a Method for Calculating Separated Flows around Airfoils with Special Consideration of Profile Drag", DLR-FB-76-36, Translated as ESA-TT-373, April 1977.
15. Henderson, M.L., "A Solution to the Two-dimensional Separated Wake Modeling Problem and its Use to Predict C of Arbitrary Airfoils Sections", AIAA Paper 78-156, January 1978.
16. Gilmer, B.R. and Bristow, D.R., "Analysis of Stalled Airfoils by Simultaneous Perturbations to Viscous and Inviscid Equations", AIAA J., Vol. 20, No. 9, September 1982, pp. 1160-1166.
17. Barnwell, R.W., "A Potential Flow/Boundary Layer Method for Calculating Subsonic and Transonic Airfoil Flow with Trailing-Edge Separation", NASA TM-81850, June 1981.
18. Carlson, L.A., "TRANSEP: A Program for High-Lift Separated Flow about Airfoils", NASA CR-3376, December 1980.
19. Le Balleur, J.C. and Neron, M., "Calcul D'Ecoulements Visqueux Decolles sur Profils D'Ailes par une Approche de Couplage", AGARD CP-291, February 1981.
20. Young, W.J., Jr. and Hoad, D.R., "Comparison of Flow Surveys above Stalled Wings", AIAA Paper 79-0149, January 1979.
21. Jacob, K., Private communication.
22. Ermolenko, S.D., "On the Non-linear Theory of Wings of Small Aspect Ratio", R.A.E. Lib. Trans. 1218, 1967.
23. Garner, H.C. and Lehrian, D.E., "Non-linear Theory of Steady Forces on Wings with Leading-edge Flow Separation", N.P.L. Aero. Rep. 1059, 1963.
24. "Vortex-Lattice Utilization", NASA SP-405, May 1976.

25. Kandil, O.A., "State of Art of Nonlinear Discrete-Vortex Methods for Steady and Unsteady High Angle of Attack Aerodynamics", AGARD CP-247, 1978.
26. Katz, J., "Lateral Aerodynamics of Delta Wings with Leading-Edge Separation", AIAA J., March 1984, pp. 323-378.
27. Weber, J.A. et al., "A Three-Dimensional Solution of Flows over Wings with Leading-Edge Vortex Separation", AIAA Paper 75-866, Hartford, CT, June 1975.
28. Maskew, B., "Calculation of Two-Dimensional Vortex-Surface Interference using Panel Methods", NASA CR-159334, December 1980.
29. Rao, B.M. and Maskew, B., "Flows over Wings with Leading-Edge Vortex Separation", NASA CR-165858, April 1982.
30. Marshall, F.J. and Deffenbaugh, F.A., "Separated Flow over a Body of Revolution", J. Aircraft, Vol. 12, No. 2, February 1975.
31. Lamb, Sir H., Hydrodynamics, 6th Ed., Dover Publications, New York, N.Y., 1945.
32. Maskew, B., "Prediction of Subsonic Aerodynamic Characteristics--A Case for Low-Order Panel Methods", Paper 81-0252, Presented at AIAA 19th Aerospace Sciences Meeting, St. Louis, MO, January 1981.
33. Morino, L., Chen, L.-T. and Suci, E.O., "Steady and Oscillatory Subsonic Aerodynamics around Complex Configurations", AIAA J., Vol. 13, No. 3, March 1975.
34. Johnson, F.T. and Rubbert, P.E., "Advanced Panel-Type Influence Coefficient Methods Applied to Subsonic Flow", Proc. AIAA 13th Aerospace Sciences Meeting, January 1975.
35. Bristow, D.R. and Grose, G.G., "Modification of the Douglas Neumann Program to Improve the Efficiency of Predicting Component Interference and High Lift Characteristics", NASA CR-3020, 1978.
36. Curle, H., "A Two-Parameter Method for Calculating the Two-Dimensional Incompressible Laminar Boundary Layer", J. R. Aero. Soc., Vol. 71, 1967.
37. Nash, J.F. and Hicks, J.G., "An Integral Method Including the Effect of Upstream History on the Turbulent Shear Stress", Proc. Computation of Turbulent Boundary Layers--1968, AFOSR-IFP-Stanford Conference, Vol. 1, 1968.

38. Cumpsty, N.A. and Head, M.R., "The Calculation of Three-Dimensional Turbulent Boundary Layers; Part II: Attachment Line Flow on an Infinite Swept Wing", Aero. Quart., Vol. XVIII, May 1967.
39. Bradshaw, P., "Calculation of Three-Dimensional Turbulent Boundary Layers", J. Fluid Mech., Vol. 46, 1971.
40. Cumpsty, N.A. and Head, M.R., "The Calculation of the Three-Dimensional Turbulent Boundary Layer; Part III: Comparison of Attachment--Line Calculations with Experiment", Aero. Quart., Vol. XX, May 1969.
41. McLean, J.D., "Three-Dimensional Turbulent Boundary Layer Calculations for Swept Wing", Paper 77-3, Presented at AIAA 15th Aerospace Sciences Meeting, Los Angeles, CA, January 1977.
42. Cumpsty, N.A. and Head, M.R., "The Calculation of Three-Dimensional Turbulent Boundary Layers; Part I: Flow over the Rear of an Infinite Swept Wing", Aero. Quart., Vol. XVIII, February 1967.
43. Maskew, B., "Program VORSEP, Interim Pilot Code, Method Description and User Guide", NASA Contract NAS1-15495, Analytical methods, Inc., December 1979.
44. Westwater, F.L., "Rolling Up of the Surface of Discontinuity behind an Aerofoil of Finite Span", Aero. Res. Council, R & M No. 1962, 1935.
45. Fink, P.T. and Soh, W.K., "A New Approach to Roll-up Calculations of Vortex Sheets", Proc. Royal Soc. of London, Series A, Vol. 362, 1978, pp. 195-209.,
46. Munk, M.M., "The Aerodynamic Forces on Airship Hulls", NACA Report 184, 1924.
47. Tsien, H.S., J. Aero. Sci., Vol. 5, 1938, p. 480.
48. Jones, R.T., "Properties of Low-Aspect Ratio Pointed Wings at Speeds below and above the Speed of Sound", NACA Report 835, 1946.
49. Moore, D.W., "A Numerical Study of the Roll-up of a Finite Vortex Sheet", J Fluid Mech., Vol. 63, Part 2, 1974, pp. 224-235.

50. Hoeijmakers, H.W.M. and Vaatstra, W., "A Higher-Order Panel Method Applied to Vortex Sheet Roll-up", NLR Report MP 81059U; see also AIAA Paper 82.0096 presented at 20th AIAA Aerospace Sciences Meeting, Orlando, Florida, January 1982.
51. Chorin, A.J. and Bernard, P.S., "Discretization of a Vortex Sheet with an Example of Roll-up", FM-72-5, College of Engr., Univ. of California, Berkeley, CA, November 1972.
52. Clements, R.R., "An Inviscid Model of Two-Dimensional Vortex Shedding", J. Fluid Mech., Vol. 57, Part 2, 1973, pp. 321-336.
53. Sytsma, H.S., Hewitt, B.L. and Rubbert, P.E., "A Comparison of Panel Methods for Subsonic Flow Computation", AGARD AG-241, 1979.
54. Kolbe, C.D. and Boltz, f.W., "The Forces and Pressure Distribution at Subsonic Speeds on a Plane Wing having 45° of Sweepback, An Aspect Ratio of 3 and a Taper Ratio of 0.5", NACA RM A51G31, October 1951.
55. De Vries, O., "Wind Tunnel Investigation of the Development of the Vortex Wake behind a Sweptback Wing", National Aerospace Laboratory, NLR Report TR-72017U, March 1973.
56. Fage, A., "Experiments on a Sphere at Critical Reynolds Numbers", Great Britain Aero. Res. Comm. Tech. Report, R & M 1766, 1937.
57. Yip, L.P. and Shubert, G.L., "Pressure Distributions on a 1 x 3 Semispan Wing at Sweep Angles from 0° to 40° in Subsonic Flow", NASA TM-72755, December 1976.
58. Smith, J.H.B., "Inviscid Fluid Models Based on Rolled-up Vortex Sheets for Three-Dimensional Separation at High Reynolds Number", AGARD LS 94, (Three-Dimensional and Unsteady Separation at High Reynolds Numbers), May 1978.
59. Peake, D.J. and Tobak, M., "Three-Dimensional Interactions and Vortical Flows with Emphasis on High Speeds", NASA TM 81169, March 1980.
60. Johnson, W., "A Lifting-Surface Solution for Vortex-Induced Airloads", AIAA J., Vol. 9, No. 4, April 1971.
61. Patel, M.H. and Hancock, G.J., "Some Experimental Results of the Effect of a Streamwise Vortex on a Two-Dimensional Wing", Aero. J., April 1974, pp. 151-155.

62. McMillan, O.J., Schwind, R.G. et al., "Rolling Moments in a Trailing Vortex Flow Field", NASA CR-151961, February 1977.
63. Maskew, B., "Predicting the Aerodynamic Characteristics of Vortical Flows on Three-Dimensional Configurations using a Surface Singularity Panel Method", Paper 13 in AGARD CP-342, April 1983.
64. McAlister, K.W. and Tung, C., "Airfoil Interaction with an Impinging Vortex", NASA TP 2273, AVSCOM Tech. Report 83-A-17, February 1984.
65. Hummel, D., "Study of the Flow around Sharp-Edged Slender Delta Wings with Large Angles of Attack", NASA Tech. Translation, NASA TT F-15, 107.
66. Smith, J.H.B., "Improved Calculations of Leading-Edge Separation from Slender, Thin, Delta Wings", Proc. Roy. Soc., London, Ser. A., 306, pp. 67-90, 1968.
67. Rao, B.M. and Nathman, J.K., "Analytical and Experimental Investigations of Delta Wings in Incompressible Flow", Office of Naval Research Report ONR-CR215-321-2, December 1976.

**END**

**FILMED**

**10-84**

**DTIC**